ELECTROMAGNETIC SIMULATION AND MEASUREMENT OF DIFFUSE SCATTERING FROM BUILDING WALLS

TESI DI LAUREA IN
Propagazione e pianificazione nei sistemi d'area LM

RELATORE:
Chiar.mo Prof. Ing.
Vittorio Degli Esposti

CORRELATORI:
Dott. Ing.
Raffaele D'Errico

Dott. Ing.
Enrico M. Vitucci

PRESENTATA DA:
Lorenzo Minghini

«I dedicate this work to my family.
A special feeling of gratitude to my loving parents,
Anna Maria Zamagna and Massimiliano Minghini.
Thank you for giving me a chance to prove and improve
myself through all my walks of life. I love you.
I also dedicate this dissertation to my many friends
who have supported me throughout the process,
I will always appreciate all they have done.
I wish to thank especially my best friend Matteo Serra,
thank you for your unconditional support and encouragement.
Finally, I would like to give special thanks
to my wonderful and beloved girlfriend Emily Farneti
who has always been by my side during these years.»

- Lorenzo Minghini -

Contents

Acknowledgements

I wish to thank my supervisors who were more than generous with their expertise and precious time. I would like to express my deep gratitude to Professor Vittorio Degli Esposti for his patient guidance, enthusiastic encouragement and useful critiques of this work. I wish to express my sincere gratitude to Dr. Raffaele D'Errico who offered invaluable assistance during my period at CEA–Leti Grenoble, without his guidance this work would not have materialized. My greatful thanks to Dr. Enrico Maria Vitucci whose support and help has been vital for the success of the project.

I would also like to extend my thanks to the members of the DSIS/STCS/LAP laboratory of the CEA–Leti Grenoble who provided the necessary means and know-how thanks to which all results in this thesis have been achieved. I am grateful for their constant support and help.

Finally I would like to thank the beginning teachers, mentor-teachers and administrators in our school division that assisted me with this project.

1

Introduction

This work is the result of the cooperation between University of Bologna and CEA-Leti, more precisely the DRT/LETI/DSIS/STCS/LAP laboratory and its staff in cooperation with the University of Bologna have provided the necessary means and know-how thanks to which all results in this thesis have been achieved.

The aim of this work is to give a better description of electromagnetic scattering in a real propagation scenario and to provide new topics for future works, in fact the scattering phenomenon has been studied for years because of its relevance in the waves propagation and in many other fields of application as well (remote sensing, optics, physics, *etc.*), but its understanding is still far from being complete. In our context the contribution of diffuse scattering to the total field in a certain propagation scenario can have a significant impact on the radio link, above all in the case of non-line-of-sight (NLOS) propagation (cf. [1]-[2]), that's why an accurate and efficient model to include in simulation programs for radio coverage estimation is needed.

As well known in case of smooth and homogeneous surfaces the propagation mechanism of the electromagnetic radiation can be analyzed with the geometrical or physical optics approximation, therefore all interactions are regarded as reflections, refractions and diffractions. In a real propagation scenario the case of a perfectly smooth surface may be rarely present, above all in urban areas where buildings have highly irregular structures and volume inhomogeneities and then the approximation to have only specular and transmitted paths is not always true. As we will see in the next paragraphs the electromagnetic propagation in complex environments can be described in different ways, this to take into account surface and volume effects that occurs in complex structures that don't generate only a reflected and transmitted component but rather a distribution of the radiation into the angular domain. It is necessary to understand that these mechanisms depend of course on the frequency of the impinging radiation as well as its polarization, its incidence angle and on the target itself (geometry, material characteristics). Therefore a part of this work is focused on describing and summarizing existing methods and models for diffuse scattering characterization, in the meanwhile some radio techniques for materials electromagnetic characteristics estimation are reported and discussed (these results can be obtained from a straightforward elaboration of the same measurements done for the diffuse scattering).

So a brief remind on the interaction between EM waves and matter is first done, various models and measurement methods for each topic are discussed and then our method of investigation, both theoretical and experimental, is reported and described.

1.1 Interaction between matter and electromagnetic radiation

When an electromagnetic wave impinges on a flat smooth surface, in the hypothesis of plane incident wave and homogeneous lossless mediums, a reflected and a refracted plane wave are generated (see fig. 1.1).
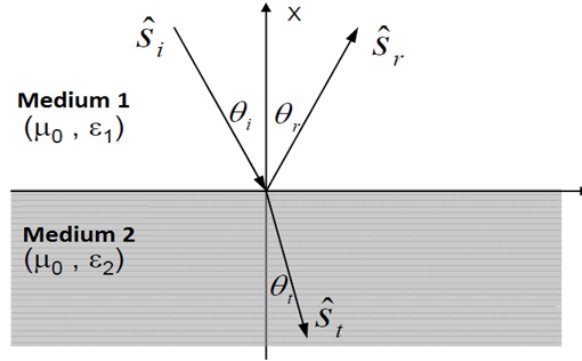
Figure 1.1: Reflection and transmission of electromagnetic radiation at an interface.

Thanks to the continuity conditions of the field at an interface for both TE and TM polarizations it is possible to write reflection and refraction laws:

- Reflection law

$$\vartheta_i = \vartheta_r \tag{1.1}$$

- Snell's law

$$n_1 \sin \vartheta_i = n_2 \sin \vartheta_t \tag{1.2}$$

Where $n = \sqrt{\frac{\varepsilon_c}{\varepsilon_0}}$ is the complex refraction index and $\varepsilon_c = \varepsilon_0 \varepsilon_r - j\frac{\sigma}{2\pi f}$ is the complex permittivity.

To take into account amplitude variations of the incident wave at the interface, we can derive reflection (Γ) and transmission (τ) Fresnel's coefficients for both TM and TE polarizations:

$$\Gamma_{\mathrm{TE}} = \frac{E_{refl\,\mathrm{TE}}}{E_{inc\,\mathrm{TE}}} = \frac{\cos\vartheta_i - \sqrt{\left(\frac{n_2}{n_1}\right)^2 - \sin^2\vartheta_i}}{\cos\vartheta_i + \sqrt{\left(\frac{n_2}{n_1}\right)^2 - \sin^2\vartheta_i}} \tag{1.3}$$

$$\tau_{\mathrm{TE}} = \frac{E_{trans\,\mathrm{TE}}}{E_{inc\,\mathrm{TE}}} = \frac{2\cos\vartheta_i}{\cos\vartheta_i + \sqrt{\left(\frac{n_2}{n_1}\right)^2 - \sin^2\vartheta_i}} \tag{1.4}$$

$$\Gamma_{\mathrm{TM}} = \frac{E_{refl\,\mathrm{TM}}}{E_{inc\,\mathrm{TM}}} = \frac{\left(\frac{n_2}{n_1}\right)^2\cos\vartheta_i - \sqrt{\left(\frac{n_2}{n_1}\right)^2 - \sin^2\vartheta_i}}{\left(\frac{n_2}{n_1}\right)^2\cos\vartheta_i + \sqrt{\left(\frac{n_2}{n_1}\right)^2 - \sin^2\vartheta_i}} \tag{1.5}$$

$$\tau_{\mathrm{TM}} = \frac{E_{trans\,\mathrm{TM}}}{E_{inc\,\mathrm{TM}}} = \frac{2\left(\frac{n_2}{n_1}\right)\cos\vartheta_i}{\left(\frac{n_2}{n_1}\right)^2\cos\vartheta_i + \sqrt{\left(\frac{n_2}{n_1}\right)^2 - \sin^2\vartheta_i}} \tag{1.6}$$

Equations (1.3)–(1.6) hold also for the magnetic field. Furthermore power relations can be obtained through the ratio of transmitted and reflected waves power with the incident power:

$$R_{\text{TE}} = \frac{P_{refl\,\text{TE}}}{P_{inc\,\text{TE}}} = \left| \frac{n_1 \cos \vartheta_i - n_2 \cos \vartheta_t}{n_1 \cos \vartheta_i + n_2 \cos \vartheta_t} \right|^2 = |\Gamma_{\text{TE}}|^2 \qquad (1.7)$$

$$T_{\text{TE}} = \frac{P_{trans\,\text{TE}}}{P_{inc\,\text{TE}}} = 1 - R_{\text{TE}} \qquad (1.8)$$

$$R_{\text{TM}} = \frac{P_{refl\,\text{TM}}}{P_{inc\,\text{TM}}} = \left| \frac{n_1 \cos \vartheta_t - n_2 \cos \vartheta_i}{n_1 \cos \vartheta_t + n_2 \cos \vartheta_i} \right|^2 = |\Gamma_{\text{TM}}|^2 \qquad (1.9)$$

$$T_{\text{TM}} = \frac{P_{trans\,\text{TM}}}{P_{inc\,\text{TM}}} = 1 - R_{\text{TM}} \qquad (1.10)$$

Where (1.8) and (1.10) result from conservation of energy.

1.2 Diffraction

Diffraction is a particular propagation phenomenon generated by obstacles present in the wave path. It differs from reflection and transmission mechanism because it determines a different field distribution compared these classical phenomena, in fact, when a certain radiation impinges on an edge (or wedge), we don't have a null field in non-directly illuminated areas and either we have a different field distribution in illuminated areas compared to what we may expect to have in the case of free space propagation. Furthermore diffraction is more relevant when geometrical dimensions (obstacles, apertures, edges, etc.) are small compared to the radiation wavelength.

(a)   (b)
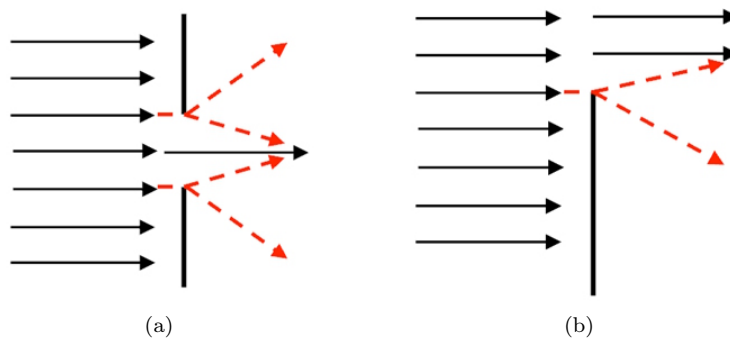
Figure 1.2: Diffraction from an aperture (a) and "Knife edge" diffraction (b).

Several methods and models can be adopted to characterize the diffraction effect depending on the field of application, the most important are: *Huygens–Fresnel principle*, *Kirchhoff–Fresnel diffraction equation* and *Fresnel ellipsoids*.

Perhaps the most intuitive way to understand the diffraction behavior is to apply the Huygens–Fresnel principle but, as it will be treated in the following for a more complex problem (cf. 1.3), it isn't here explained. Anyway we will give a brief summary based on *Geometrical Optics* (GO) and *Geometrical Theory of Diffraction* (GTD) in order to explain the basics of this phenomenon.

In this approach the electromagnetic radiation can be viewed as traveling along defined paths known as rays; the ray path, in any continuous medium, may be determined using the *Fermat's principle* which states that the energy flows along the paths of shortest electrical length between any two points in the medium. The shortest electrical path is the path which results in the shortest propagation time between the two points, furthermore these

rays are orthogonal to constant phase surfaces (the wavefront), then if the media is also homogenous ray paths are straight lines. These before mentioned concepts are at the base of GO, which natural extension to include diffraction phenomena has been first introduced by J. B. Keller founding the GTD on the following assumptions:

1. A diffracted ray is generated whenever a ray impinges on an edge (or on a vertex)

2. For every diffracted ray the Fermat's principle still holds

These two statements leads to *diffraction law*: the angles between incident or diffracted rays and the edge satisfy Snell's law (1.2) applied to diffraction, where the transmission angle ϑ_t becomes in fact the angle of diffraction ϑ_d.

If the rays are in the same material then $\vartheta_d = \vartheta_i$, therefore diffracted rays outside the wedge belong to the *Keller's cone* (fig. 1.3).
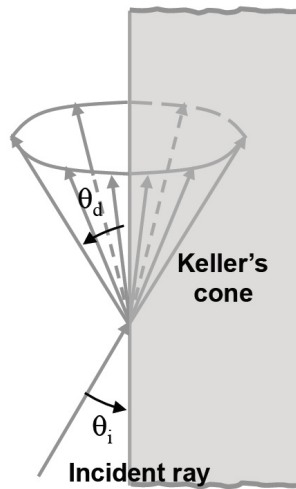
Figure 1.3: Representation of the Keller's cone.

Considering only straight edges, if the impinging wave is plane, the diffracted wave is cylindrical for perpendicular incidence ($\vartheta_d = \vartheta_i = \frac{\pi}{2}$) and conical for oblique incidence.

1.3 Diffuse scattering

Strictly speaking diffuse scattering is the reflection (and transmission) of radiation from a rough surface such that an incident ray is reflected (and transmitted) at many angles rather than at just one angle as in the case of specular reflection (and transmission). As a consequence of this the energy is scattered in a wide range of directions, apparently without following the geometrical optics rules.

Furthermore diffuse scattering has several behaviors and its characterization is not as simple as it could seem. In the next sections we will analyze different methodologies and theories adopted to study such phenomenon, but at the beginning it's better to give a qualitative understanding of this topic.

First we define a surface as *rough* if it scatters the energy of an incident plane wave into various directions rather than only in the specular one (cf. [3]). According to this definition, the same surface may be rough for some wavelength and smooth for others, and the same could happen for different angles of incidence. An issue that is strictly related to the surface definition is how we can threat the different kinds of surfaces present in the environment; as one can imagine a lot of different structures, materials and buildings exist in urban scenarios and a full geometric and electromagnetic description would be needed to completely solve the problem. This let we understand that the deterministic approach requires enormous costs in terms of computational capability and environment description.

Another thing that has to be considered is that scattering is the superposition of several effects that occurs even in the volume of the object, not only on its surface, and this is

primarily due to material heterogeneities of various nature present in the structure we are analyzing (cables, air cavities, pipes, layers, etc.). Finally one can understand the huge amount of information required for a deterministic definition of the problem and the poor flexibility that this method offers in general terms of radio coverage estimation. On the other hand the deterministic approach is necessary to analyze and better understand the behavior of diffuse scattering and this may lead to the formulation or verification of simpler but effective models.
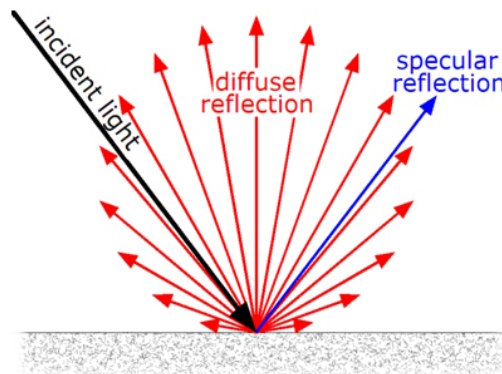
Figure 1.4: A simple representation of diffuse scattering in the reflection half–space.

Thus the most general situation is represented by an inhomogeneous medium composed of materials with different electromagnetic properties and the energy that impinges on the object is reflected, absorbed (if losses are present), transmitted and scattered. This last effect is the one on what we're focusing in this work, because of its contribution in signal propagation. Actually we can distinguish between surface and volume scattering, the former concerns all interactions on the boundaries of the object, while the latter refers to effects that take place into the medium. The contribution of volume scattering is usually weaker than surface scattering, this owing to the fact that the transmitted wave is only a portion of the incident one and also volume interactions cause a redistribution of energy of this wave in multiple directions, which results in a loss of energy density. Furthermore we have to consider that for lossy materials the scattering due to scatterers inside the medium experience an additional attenuation due to conduction. Conductive losses depend in fact on frequency and on the material itself:

$$\tan \delta = \left| \frac{\Im m \{\varepsilon_c\}}{\Re e \{\varepsilon_c\}} \right| = \frac{\sigma}{\omega \varepsilon} \tag{1.11}$$

Where σ [S/m] is the conductivity of the material. Therefore volume scattering strictly depends on the material structure, from its geometry to the electromagnetic characteristics of its various parts.

As said at the beginning of this section a surface can be regarded as rough when irregularities in the surface lead the reflected wave from the surface to differ significantly from the specular reflection.

Let's formalize this concept: when a wave interacts with a rough surface each component has a different phase variation due to heights distribution, this can lead them to partially cancel or sum. As well–known this interaction is fully destructive when the phase difference is π and that occurs when the path difference, in terms of distance, is a half wavelength. However destructive interference is always present in the range $\left[\frac{\pi}{2} < \Delta\phi < \frac{3}{2}\pi\right] + k2\pi$ while constructive interference happens when $\left[-\frac{\pi}{2} < \Delta\phi < \frac{\pi}{2}\right] + k2\pi$, where $\Delta\phi = \phi_2 - \phi_1$ is the phase difference between two components and $k \in \mathbb{N}$. The phase difference $\Delta\phi$ can be derived as shown in figure 1.5 and it holds:

$$\Delta\phi = 2 \cdot \Delta h \cdot \frac{2\pi}{\lambda} \cdot \sin \psi = 2 \cdot \Delta h \cdot \frac{2\pi}{\lambda} \cdot \cos \vartheta_i \tag{1.12}$$

Using the *Rayleigh criterion* a surface can be considered rough if the phase difference
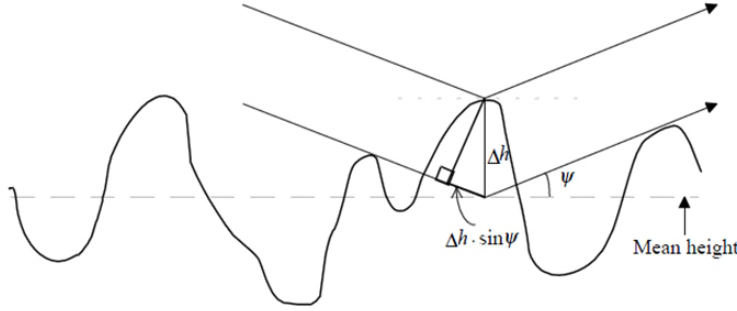
Figure 1.5: Different paths (phase difference) due to surface roughness with respect to a smooth surface.

between two reflected waves is more than $\frac{\pi}{2}$:

$$\Delta h \geq \frac{\lambda}{8 \cos \vartheta_i} \tag{1.13}$$

Where Δh is the height variation (or the standard deviation of heights if statistically represented) of the considered surface, λ is the wavelength and ϑ_i is the incidence angle with respect to the surface normal.

The usage of more stringent conditions are reported in [3]–[4], one of them is called *Fraunhofer criterion* and considers a surface as rough if the phase difference exceeds $\frac{\pi}{8}$:

$$\Delta h \geq \frac{\lambda}{32 \cos \vartheta_i} \tag{1.14}$$

Therefore if Δh is small compared to the wavelength, then the phase difference is insignificant but, if it is not, the specular reflection will be reduced due to interference of the reflected waves. Note that thanks to the previous criterions, surfaces that are rough at one angle of incidence can be smooth at another, in fact, looking at the right side of 1.12, the surface will tend to be effectively smooth under two conditions:

$$\frac{\Delta h}{\lambda} \to 0 \qquad \text{or} \qquad \vartheta_i \to \frac{\pi}{2} \tag{1.15}$$

However one has to understand that the Rayleigh criterion, even if widely used in engineering practice, takes into account only surface roughness, it is based on a simple ray theory and describes the irregularities of the rough surface by Δh only.

In a real environment all degrees of roughness ranging from perfectly smooth to completely rough are actually present. In figure 1.6 we can see the contribution to the reflected power due respectively to coherent and the diffuse (or incoherent) components in function of the degree of surface roughness.
The higher the degree of roughness (and volume inhomogeneities) the more the power becomes incoherent and spreads in all directions; in fact in case of a very rough surface the coherent component (only present in the direction of specular reflection) can be neglected.

In order to give a complete point of view let better discuss about coherent and incoherent contributions. As already said before, the scattering phenomenon could be seen as the reduction on average of the specular reflected component on behalf of the diffuse field, where the term "average" is to be interpreted as an ensemble average over many specimens (surfaces, soils, walls, etc.) obeying the same statistics. The *coherent component* is then defined as the part of radiation that is found around the specular direction of reflection, where a field averaging over many realizations gives a non-zero contribution because of phase preservation. On the other hand roughness generates also fluctuating-phase components in directions that differ from the specular one, the mean generated field of this *incoherent* (or *diffuse*) *component* is zero in average even if it has a non-null power for any realization (see fig. 1.7a–1.7b).

$$E(\bar{r}) = \langle E_{coh}(\bar{r}) \rangle + E_{incoh}(\bar{r}) \tag{1.16}$$
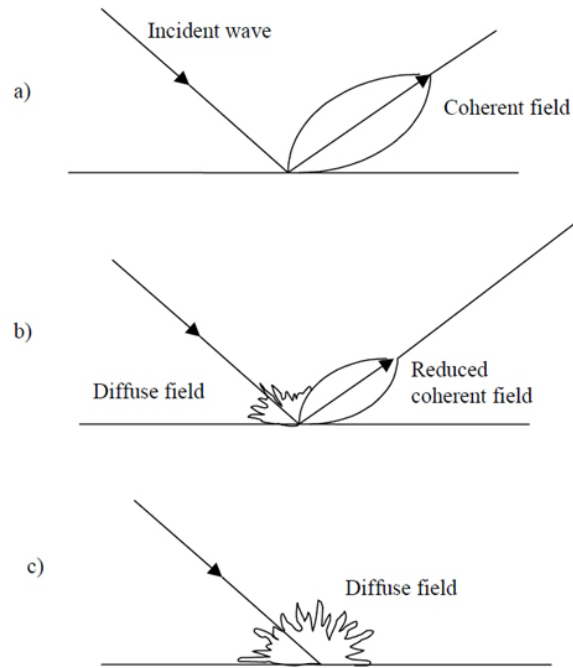
Figure 1.6: Coherent and diffuse field for smooth (a) slightly rough (b) and very rough (c) surface.

Thus the total field $E(\bar{r})$ is a random function of position obtained as the sum of two different components: the average coherent field and the fluctuating incoherent field, which mean is $\langle E_{incoh}(\bar{r}) \rangle = 0$ as said before.
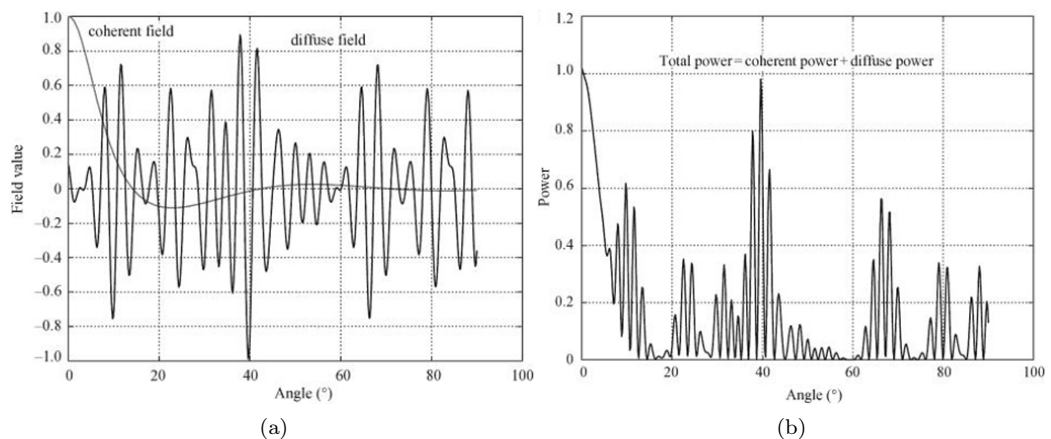
Figure 1.7: Difference between coherent and incoherent fields. The diffuse field has a zero mean (a) when averaged on many realizations of surfaces but, for any realization, it could add a significant contribution to the total scattered power (b).

This behavior can be understood by the *Huygens-Fresnel principle*: every point to which an electromagnetic perturbation reaches becomes itself a source of a spherical wave, the sum of these secondary waves determines the form of the wavefront at any subsequent time.

This principle can also be applied when a plane wave impinges on an interface. In fact an electromagnetic field is generated by the secondary sources along the surface, each of which has its own phase depending on its position. Considering a smooth surface, the superposition of these spherical waves locally generated on the surface give rise to a non-zero contribution only in the specular direction of reflection, this according to the fact that along that direction they interfere constructively due to the zero phase difference.

As a consequence the more we get far from the specular direction the more destructive interference happens.
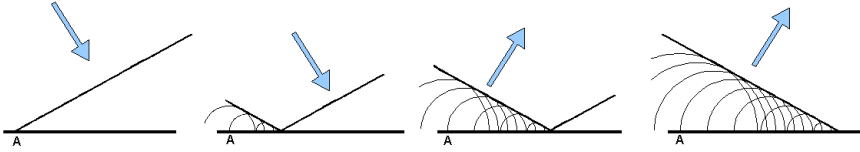
Figure 1.8: Reflection of a plane wave from a smooth surface represented by Huygens principle.

Precisely speaking this behavior is valid only in the case of a surface of infinite extension, when one considers finite-dimensions surfaces border effects must be taken into account. In fact, as well reported in [3], a non-infinite smooth surface will not reflect only in the specular direction, but event in its proximity; the smaller the slab the more this effect is emphasized.

Considering now a rough surface it is easy to understand that the superposition of all spherical waves doesn't follow the specular reflection mechanism. What we have is then a pseudo-random distribution of the electromagnetic radiation in the space, with specular and diffused components strengths related to the surface roughness (in addition to frequency, polarization and material properties).

Thus, being the superposition of a large number of micro-contributions of unknown characteristics, diffuse scattering is essentially characterized by its non-coherency, *i.e.*, the phase and polarization of the scattered field cannot be considered deterministic, but rather random. Thanks to this we can express the power scattered by the surface in one direction as the sum of a coherent and an incoherent contribution (cf. [2]):

$$P_{scattered} = P_{coh} + P_{incoh} \qquad (1.17)$$

1.4 Statistical description of rough surfaces

As previously said, because of the variety of geometric configurations, it is impossible to precisely describe all the media and structures present in the environment. So it is necessary to introduce a statistical description of the problem taking into account a large spectrum of possible scenarios, starting from the characterization of the surface roughness.

The statistical behavior of a *random rough surface* (RRS) is completely given by two main factors:

1. The *statistical distribution of surface heights*

2. The *spatial correlation function*

The former function gives us the understanding on how the heights are distributed around a certain mean level, while the latter gives information on how hills and valleys are linked together in the spatial domain.

Thus, generally speaking, we may have the heights distribution following a certain statistics around a certain mean level while the spatial correlation function follows another kind of relationship. In fact, for naturally occurring surfaces, it is reasonable to assume the probability distribution of the heights as Gaussian with a certain spatial correlation (Gaussian, exponential, n-th order, etc.) among peaks that has to be chosen according to the application (cf. [4]).

Obviously other methods could be adopted to characterize the stochastic behavior of rough surfaces (some of them include also fractal expansions), anyway the majority of works present in the literature tend to confirm that the statistical approach described above is optimal way to represent a wide range of common scenarios.

1.4.1 1D Gaussian random rough surface

The surface profile is described by a height function $f(x)$, which is a random function of coordinate x. The profile heights assume values $z = f(x)$, with a Gaussian probability density function $p(z)$ as:

$$p(z) = \frac{1}{\sqrt{2\pi\sigma^2}} \, e^{-\left(\frac{(z-\mu)^2}{2\sigma^2}\right)} \tag{1.18}$$

Where σ is the standard deviation (that in this context concerns the surface heights deviation) and μ is the mean value of the surface heights (usually normalized to zero). The Fourier transform of the rough surface height function is generally:

$$F(k_x) = \frac{1}{2\pi} \int_{-\infty}^{+\infty} f(x) \, e^{-ik_x x} dx \tag{1.19}$$

Where $k_x = \frac{2\pi}{L}$ is the variable in the domain of spatial frequency and L is period of repetition of the considered profile (surface dimension). If the surface is infinite the Fourier transform does not exist, this is the reason why we have to define the truncated function:

$$f_L(x) = \begin{cases} f(x) & \text{if } |x| \leq \frac{L}{2} \\ \\ 0 & \text{if } |x| \geq \frac{L}{2} \end{cases} \tag{1.20}$$

The Fourier transform then becomes:

$$F_L(k_x) = \frac{1}{2\pi} \int_{-\infty}^{+\infty} f_L(x) \, e^{-ik_x x} dx \tag{1.21}$$

Equations (1.19) and (1.21) agree for large L. If we consider two Gaussian random variables $z_1 = f(x_1)$ and $z_2 = f(x_2)$ with zero mean value ($\mu_1 = \mu_2 = 0$) and the same standard deviation ($\sigma_1 = \sigma_2 = \sigma$), the correlation of the two random variables is:

$$R_f(x_1, x_2) = \langle z_1 z_2 \rangle = \sigma^2 C(x_1, x_2) \tag{1.22}$$

Where C is the *normalized correlation function* of the two random variables and σ is nothing but the standard deviation of the heights (sometimes reported also as h or Δh). If $C = 0$ then z_1 and z_2 are independent random variables. Some commonly used correlation functions are:

- the *Gaussian normalized correlation function*:

$$C(x_1, x_2) = \exp\left[-\frac{(x_1 - x_2)^2}{l^2}\right] \tag{1.23}$$

- the *exponential correlation function*:

$$C(x_1, x_2) = \exp\left[-\frac{|x_1 - x_2|}{l}\right] \tag{1.24}$$

Where l is the *correlation length*, defined as the distance within which the normalized correlation is higher than $\exp(-1)$. In both (1.23) and (1.24) as $|x_1 - x_2| \gg l$ the autocorrelation function tends to be zero and this means that two points on the surface separated by a distance much larger than the correlation length are independent.

Besides the height function $z = f(x)$, the slope function $z' = \frac{df(x)}{dx} = \alpha(x)$ is also an important characterization parameter of the rough surface. In the same way as (1.22), it holds:

$$\langle \alpha(x_1)\alpha(x_2) \rangle = s^2 C_\alpha(x_1, x_2) \tag{1.25}$$

Where s is the *rms slope* and C_α is the correlation function for the slope function so that $C_\alpha(0) = 1$. If the height function is normally distributed then also its first derivative,

the slope function, will be normal with $\langle \alpha(x) \rangle = 0$ and variance related to the second derivative of the $z(x)$ correlation function at the origin (cf. [3]–[4]):

$$s^2 = \langle \alpha^2(x) \rangle = -\sigma^2 C''(0) \tag{1.26}$$

The rms slope is then simply the square root of (1.26). For the Gaussian correlation function (1.23) the respective slope correlation function is:

$$\begin{aligned} C_\alpha(x_1, x_2) &= -C''(x_1, x_2) \\ &= \frac{2}{l^2} \left(1 - \frac{2(x_1 - x_2)^2}{l^2} \right) \exp\left[-\frac{(x_1 - x_2)^2}{l^2} \right] \end{aligned} \tag{1.27}$$

So that, from (1.26):

$$s^2 = -\sigma^2 C''(0) = \frac{2\sigma^2}{l^2} \tag{1.28}$$

For the exponential correlation function (1.24) the rms slope doesn't exist, in fact, because of sharp edges that may exist in the rough surface profile, some integrals (here not reported) are no longer calculable (cf. [4]).

1.4.2 2D Gaussian random rough surface

The two dimensional case of a random rough surface is the natural extension of the one dimensional case. In fact now we have to consider z, the stochastic height of the roughness, as a function of both x and y coordinates, so that $z = f(x, y)$. Even in this case a truncation (that can be seen as a periodization as well) of $f(x, y)$, similarly to what done in (1.20), is necessary. Like in (1.22) the correlation function of a 2D surface is defined by:

$$\begin{aligned} R_f(x_1, y_1; x_2, y_2) &= \langle z_1 z_2 \rangle \\ &= \langle f(x_1, y_1) f(x_2, y_2) \rangle \\ &= \sigma^2 C(x_1, y_1; x_2, y_2) \end{aligned} \tag{1.29}$$

The variables involved in the two dimensional extension are the same as in 1.4.1, they have just a slightly different form (cf. [5]):

- Gaussian correlation function

$$C(x, y) = \sigma^2 \exp\left[-\left(\frac{x^2}{l_x^2} + \frac{y^2}{l_y^2} \right) \right] \tag{1.30}$$

- Exponential correlation function

$$C(x, y) = \sigma^2 \exp\left[-\sqrt{\left(\frac{x^2}{l_x^2} + \frac{y^2}{l_y^2} \right)} \right] \tag{1.31}$$

Where l_x and l_y are the correlation lengths for the x and y direction respectively; the corresponding *power spectral densities* are subsequently reported:

- Power spectral density for the Gaussian correlation function

$$W(k_x, k_y) = \frac{\sigma^2 l_x l_y}{4\pi} \exp\left[-\left(\frac{k_x^2 l_x^2}{4} + \frac{k_y^2 l_y^2}{4} \right) \right] \tag{1.32}$$

- Power spectral density for the exponential correlation function

$$W(k_x, k_y) = \frac{\sigma^2 l_x l_y}{2\pi} \left[1 + \left(k_x^2 + k_y^2 \right) l_x l_y \right]^{-\frac{3}{2}} \tag{1.33}$$

As we can see from figure 1.9a and figure 1.9b the surface generated with the exponential spatial correlation function presents fine-scale elements with respect to the Gaussian one (generation parameters are the same in both cases).

The *slope function* isn't here reported because the same considerations done in the previous paragraph still holds and the expansion to the 2D case is straightforward as seen for the other parameters.

In order to give a complete description of random rough surfaces topic, the numerical method for generating RRS will be described and analyzed in the following chapters (see 4.2.1).
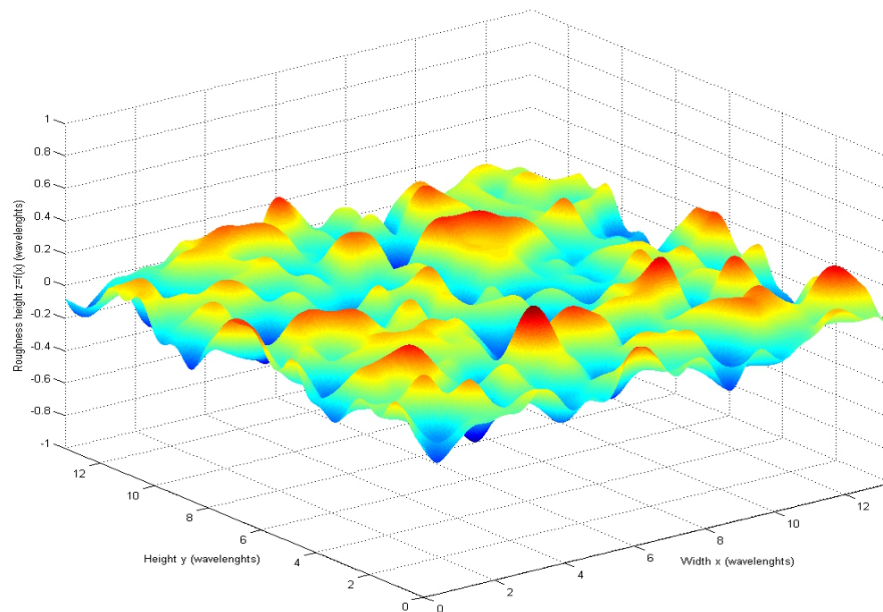
(a)
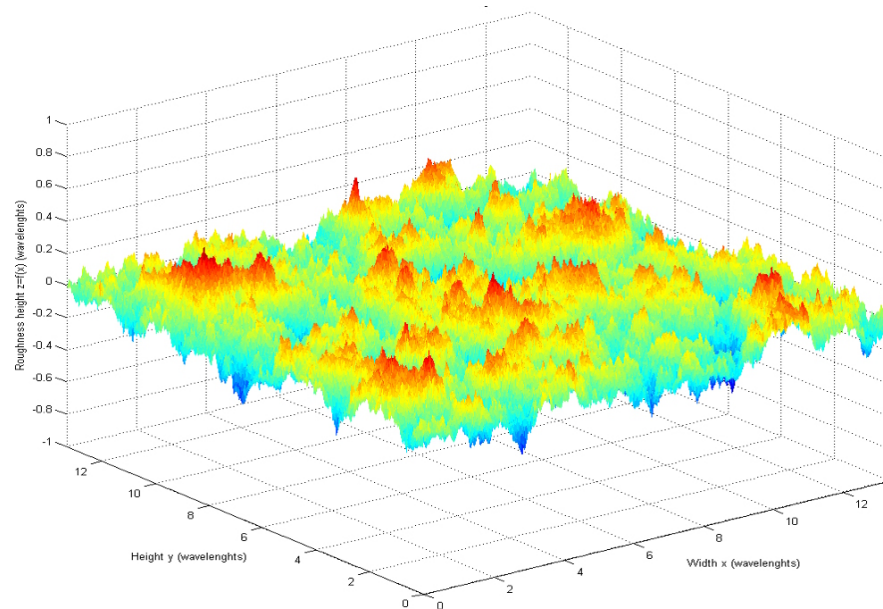
(b)

Figure 1.9: Generated surfaces with Gaussian distribution of heights and Gaussian (a) or exponential (b) correlation function.

2

Scattering models: state of the art

There are several models to solve and characterize the scattering phenomenon. First we have to remember that each problem concerning electromagnetism can be completely solved applying *Maxwell's equations* (2.1)–(2.4), constitutive relations of media and boundaries conditions to our domain:

$$\nabla \times \bar{E} = -\frac{\partial \bar{B}}{\partial t} \tag{2.1}$$

$$\nabla \cdot \bar{E} = \frac{\rho}{\varepsilon_0} \tag{2.2}$$

$$\nabla \times \bar{H} = \frac{\partial \bar{D}}{\partial t} + \bar{J}_c + \bar{J}_i \tag{2.3}$$

$$\nabla \cdot \bar{H} = 0 \tag{2.4}$$

Where $\bar{D} = \varepsilon \cdot \bar{E}$, $\bar{B} = \mu \cdot \bar{H}$ and $\bar{J}_c = \sigma \cdot \bar{E}$. However this problem is not analytically calculable due to the multitude of parameters being involved, thus several computational numerical techniques have been developed and implemented in computer software. Thanks to this we obtain closed form solutions of Maxwell's equations under various constitutive relations of media and boundary conditions. Some examples of these numerical techniques are *method of moments* (MoM), *finite-difference time-domain* (FDTD) and *integral methods*.

Therefore with these models a complete electromagnetic characterization of the scenario is done but, precisely because of their deterministic formulation, these techniques require an accurate modeling of the environment under test (both geometric and electromagnetic properties). Exactly for what we said in the previous section, inherently to the fact that a deterministic definition of the problem offers a poor flexibility and no databases that describe urban areas in detail are available, these methods are suitable only to perform simulations of small and known structures. Obviously the dimension of the environment that can be simulated in an acceptable amount of time depends on computational capabilities. Just to give an idea, for this type of methods, the order of magnitude could be in the range of few cube meters using a high-end simulation computer.

So it is clear that regarding the overall cost in terms of memory, CPU and database construction, the complete electromagnetic simulation of a large scene like and urban area is almost impossible (or at least is not effective).

To overcome these problems asymptotic techniques, like *ray-tracing* (RT), have been developed over the time. In fact these methods compute all the possible paths followed by the electromagnetic wave between a transmitter and a receiver in a given environment according to *Geometrical Optics* (GO) for reflection and transmission through an interface and the *Geometrical/Uniform Theory of Diffraction* (GTD/UTD) for interactions with edges and wedges. Because of this RT offers only an approximated, but still good, solution of the problem. As it's easy to understand we solve the environment under test using some approximations on Maxwell's equations: that permits to simplify the problem and reduce

computational stress together without a big loss of generality. However diffuse scattering is not usually taken into account, hence several studies have been done in the last years to deal with this lack.

2.1 Analytical modeling of scattering

Theoretical-analytical models yield a significant understanding of the interaction between the electromagnetic waves and the environment, although an exact solution of equations governing this interaction may not always be available because of the complexity of the scenario.

The most known and common analytical models discussed in literature comprehend the *Kirchhoff Approximation* (KA), the *Small Perturbation Method* (SPM) and the *Integral Equation Method* (IEM). The Kirchhoff Approximation and the Small Perturbation Methods represent early approaches to scattering which are still much used, whereas the Integral Equation Method represents a newer approach which has a larger domain of validity.

Our aim is to give only a general description of these methods, for a complete understanding the reader is referred to the cited bibliography.

2.1.1 Small perturbation method

The scattering of electromagnetic waves from a slightly rough surface can be studied using a perturbation method (cf. [3]–[4]). It is assumed that the surface variations are much smaller than the incident wavelength and the same is for slopes of the rough surface, thus the scattered field can be expressed as a superposition of plane waves. Furthermore the assumption of considering the variation of the heights small compared to the wavelength can be seen as a perturbation of the smooth surface scattering problem due to the presence of roughness.

The field amplitudes are then determined by the boundary conditions on the surface S with normal $\hat{n}$ and heights distribution considered as a function of two coordinates, *i.e.*, $z = f(x, y)$: the *Dirichlet problem* (2.5) describes the TE polarization whilst the *Neumann problem* (2.6) concerns the TM polarization, both for a perfectly conducting surface:

$$(\psi)_S \quad = \quad 0 \tag{2.5}$$

$$\left(\frac{\partial \psi}{\partial \hat{n}}\right)_S \quad = \quad 0 \tag{2.6}$$

Where in general ψ stands for a component of any of the field vectors. The physical behavior derives directly from the solving the waves equation:

$$\nabla^2 \psi = \frac{1}{\nu} \frac{\partial^2 \psi}{\partial t^2} \tag{2.7}$$

That for harmonic solutions of ψ, *i.e.*, $\psi(\bar{r}, t) = \psi(\bar{r}) \cdot e^{i\omega t}$, (2.7) becomes the Helmholtz equation:

$$\nabla^2 \psi = -k^2 \psi \tag{2.8}$$

Generally we can consider the wave as the superposition of the incident and the scattered field:

$$\psi = \psi_{inc} + \psi_{scat} \tag{2.9}$$

Where $\psi_{inc} = e^{i(k_{ix} x - k_{iz} z)}$ (plane wave that propagates in the xz plane) with $k_{ix} = k \sin(\vartheta_i)$, $k_{iz} = k \cos(\vartheta_i)$. In the perturbation method one uses the height of the random rough surface as a small parameter, this is based on the assumption that:

$$k \cdot \Delta h \ll 1 \tag{2.10}$$

Where Δh is the RMS height. Then we can write the scattered wave as a perturbation series:

$$\psi_s = \psi_s^{(0)} + \psi_s^{(1)} + \psi_s^{(2)} + \ldots \tag{2.11}$$

Finally imposing the desired boundary condition (2.5) or (2.6) and a proper formulation for the scattered field ψ_s, makes possible to solve the problem with an accuracy strictly related to the truncation order chosen to represent the perturbation series (2.11).

The validity of the perturbation theory is restricted by (2.10), in fact the accuracy will decrease as the angle of incidence increases, this because the resulting degree of roughness is higher for grazing angles. Moreover, in its first formulation, this model doesn't take shadowing (parts of the surface is not illuminated due to roughness) into account, however some theories have been developed to consider this effect.

2.1.2 Kirchhoff theory

The *Kirchhoff approach* (KA) is based on solving the scattering problem by using the approximation that each point on the scatterer is part of an infinite plane, parallel to the local surface tangent: this means that the fields at any point on the surface are approximated by the fields that would be present on the tangent plane at that point, therefore the reflection is considered to be locally specular. Because of the tangent approximation the Kirchhoff approach requires that every point on the surface has a large radius of curvature compared to the wavelength of the incident field, as a consequence this theory breaks down if the roughness includes sharp edges or sharp points.
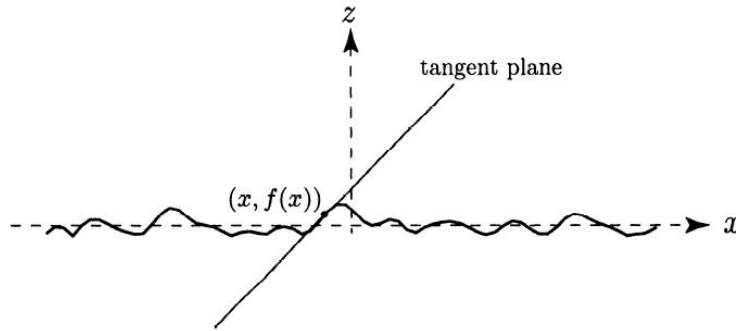
Figure 2.1: Tangent plane at a general point of the rough surface.

Thus the validity of the solution is essentially limited by the assumption that the field obeys to the local reflection principle, so that at each point of the surface S holds:

$$(E)_s = (1 + R) E_{inc} \tag{2.12}$$

Where $E = \bar{E}/\hat{e}$ is the scalar value of the field and R is the reflection coefficient for a smooth plane (see 1.1). Equation (2.12) is fulfilled exactly in the case of an infinite plane, so in a real case it will be a very good approximation for "locally flat" surfaces composed of irregularities with small curvatures. As reported in [3] it is required that at distances from the point of tangency which are large compared to the wavelength of the incident radiation, the tangent plane shall not be appreciably distant from the rough surface. A useful criterion is that the radius of curvature r_c must respect the condition:

$$4\pi r_c \, cos\vartheta_i \ll \lambda \tag{2.13}$$

Where ϑ_i is the local angle of incidence. Being this the principal limit on the model, the surface must not contain a large amount of sharp edges, sharp points or other irregularities with small radii of curvature. Since every point of the surface has two principal radii of curvature one has to consider always the smaller when applying (2.13). Besides the radius of curvature condition, the Kirchhoff approximation also ignores shadowing and multiple scattering; accordingly to this we have that the validity of the model also depends on the incidence angle.

Other restrictions on the Kirchhoff approximation have been stated in [6] for random
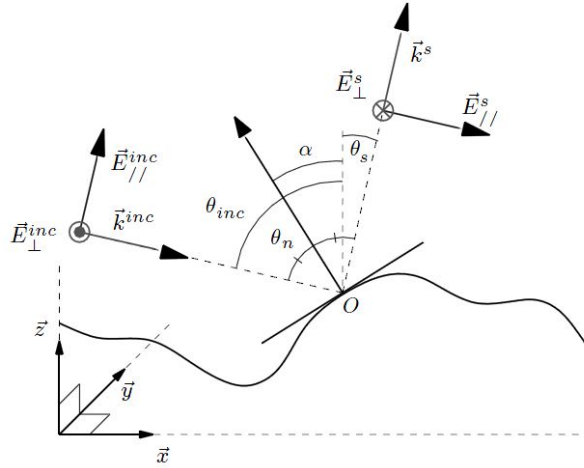
Figure 2.2: Local scattering geometry assumed by the Kirchhoff approximation.

rough surfaces with both Gaussian distribution of heights and correlation function:

$$kl \quad > \quad 6 \tag{2.14}$$

$$\sigma \quad < \quad \frac{l^2}{2.76 \cdot \lambda} \tag{2.15}$$

Where $k = \frac{2\pi}{\lambda}$ is the wave number, l is the correlation length and λ is the radiation wavelength.

The importance is to understand that this model, as well as the small perturbation method, can adopt different expressions for the incident and scattered field. In fact in literature are reported several works that using these approximations try to characterize exactly the scattering phenomenon in different ways. Some applications can be found in [3], [4] and [6].

2.2 Empirical-analytical models

Analytical models are for sure powerful and useful tools to characterize and comprehend the scattering phenomenon. However, in real scenarios, their assumptions cannot be always satisfied, in fact effects like shadowing, high degree of roughness, volume effects, etc. are typically present in the environment. Therefore these models can't give always a correct description of what actually happens and the prediction may differ significantly from what observed in the reality.

In order to overcome these lacks empirical models have been developed over the time. These models are usually derived by physical considerations or directly from one of the analytical models cited before; their aim is usually to simplify the characterization giving a general description of scattering in a mean way, so to include all possible effects in a straightforward formulation. This last thing is one of the main advantages of this approach: the exact, rigorous solution is substituted by a general case solution that comprehends a large variety of possible scenarios. Now it's easy to understand that the computational stress falls down significantly and moreover no requirements on the environment database are necessary. Therefore a trade-off has been done, we lost something in the rigorous and exact representation of the scattering phenomenon but we gained in generality and effectiveness of the process.

The adoption of empirical-analytical models leads then to a reduction of the model complexity and to a great simplification with respect to rigorous approaches, in fact the majority of these methods are suitable for being implemented in ray-tracing software thus to add a description of the scattering phenomena in a large and complex propagating environment.

In addiction simpler methods giving only a stochastic representation of the scattering phenomenon have been developed over the time. These methods usually represent the scattering through a certain statistical distribution, which in the simplest case could be a decay law, and they don't give any information about the low-level interaction that happens when an electromagnetic wave impinges on a wall. However they are very useful tools to use in combination with more accurate models in order to integrate the results or decrease the computational stress but, as one can easily comprehend, they're not very suitable for a detailed analysis of the scattering phenomenon. For this reason fully-statistical models won't be considered in our work.

2.2.1 Lambertian scattering pattern

One of the first empirical models that has been adopted in the scattering characterization is the Lambertian scattering pattern (see fig. 2.3). It assumes the scattered field intensity to be proportional to the cosine of the angle between the surface normal vector and the scattered ray (so its maximum is in the direction perpendicular to the wall) and being independent from the angle of arrival of the incident wave:

$$E_s^2 = E_{s0}^2 \cdot \cos \vartheta_s \tag{2.16}$$

Where E_s is the scattered field, E_{s0} is its maximum amplitude and ϑ_s is the angle between the surface normal and the scattering direction.

This model is usually representative of surfaces with high degree of roughness and volume irregularities, where the superposition of all effects is in first approximation characterized through a non-uniform irradiation, according to (2.16), in the upper half space of a spherical wave which departs from the surface element.
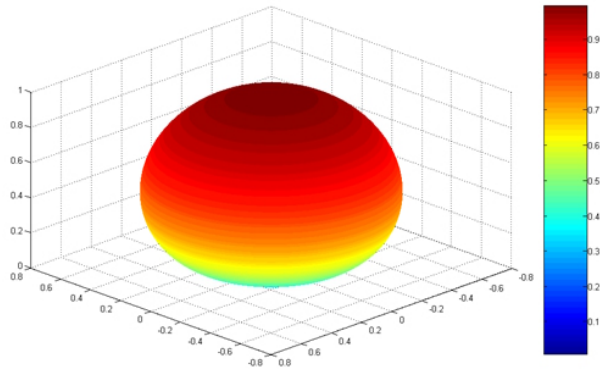
Figure 2.3: Lambertian scattering pattern.

The Lambertian pattern has been proved to be rarely representative of the scattering spatial distribution in real propagation scenarios, however it can be considered as one of the first steps in the scattering characterization, giving a general description when the environment is completely unknown.

2.2.2 Micro-facet based scattering model

The following model (cf. [7]–[8]) is based on the Kirchhoff Approximation (KA, see 2.1.2), so the rough surface is decomposed into micro-facets, *i.e.*, into small planes that are locally tangent to the roughness (see figure 2.4b). According to this the micro-facet based model inherits all the assumptions and limits of the KA even if it is at the same time valid for both slightly rough and very rough surfaces.

The decomposed rough profile is illuminated with an incident plane wave. Thus, each micro-facet receives the same part of the incident plane wave and reflects it in its own specular direction. The overall scattered field is obtained thanks to a coherent sum of all the contributions of the reflected fields encapsulated in a small solid angle $d\vartheta$ around a specific direction ϑ_s, in order to take into account interferences due to the possible various heights of the corresponding micro-facets.
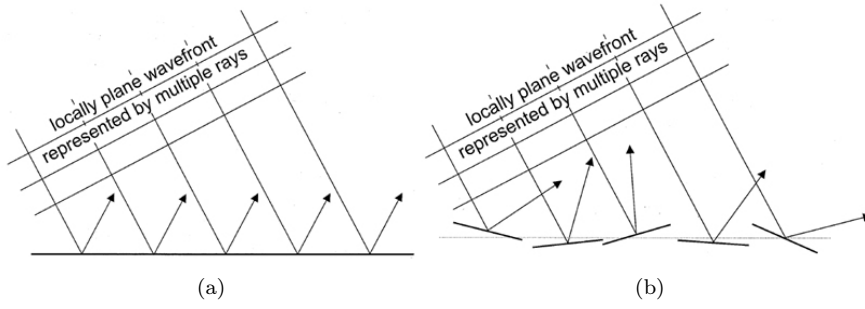
Figure 2.4: Reflection at tangential planes for each discrete ray.

Defining $p(\vartheta_s)$ as the *probability density function* (PDF) to have a well-directed micro-facet around a specific direction, one is able to evaluate the scattered field in the ϑ_s direction and it's also possible to compute the scattered field for many kinds of rough surfaces. In fact several continuous or discrete roughness profiles (also representing building façades) can be adopted in this model, allowing to choose the one that better describes the surface. Even if this last point offers a good flexibility it could be very tricky to find the PDF that correctly represents the analyzed environment.

2.2.3 Scattering from building façades

The key assumption of this model (cf. [9]) is that non-specular scattering from the façades of large buildings is usually dominated by windows and decorative masonry which placement is nearly periodic if we consider high density populated areas. Thus computing the scattering for many realizations of building façades, with parameterized dimensions as represented in figure 2.5, allows us to average its properties in order to achieve a single smoothed scattering coefficient.

The scattering due to building facades is then considered in a mean statistical way and not as a punctual effect. This agrees with the fact that different kinds of buildings have different behaviors when an electromagnetic wave impinges on their façade.
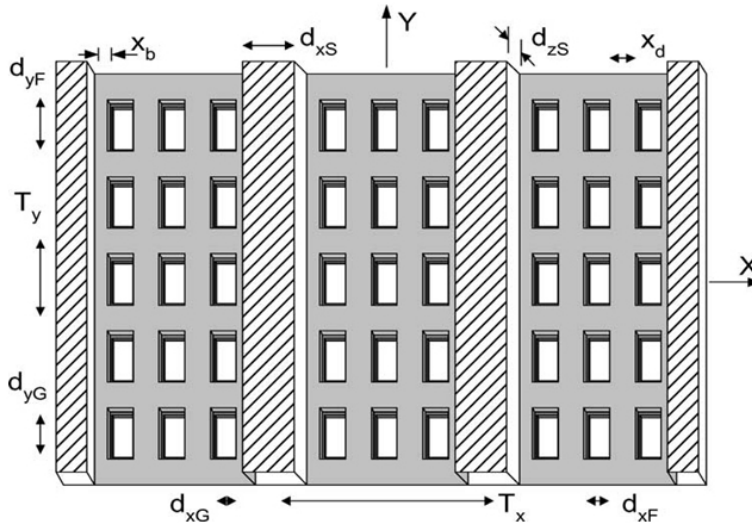
Figure 2.5: Model of a building façade used in simulations.

A plane wave with a certain angle of incidence is assumed to illuminate the façade, then the reflected field $\bar{E}_{refl}(\bar{r}')$ is considered to be equal to the incident field multiplied by the local reflection coefficient (1.3) or (1.5) depending on the polarization.

Assuming the façade as periodic leads to the decomposition of the scattered field, expressed by the vectorial form of the Kirchhoff-Huygens' expression with harmonic time

dependence (2.17), in a series of harmonic waves (cf. [9]).

$$\iint_A \left[i\omega\mu_0 \bar{\bar{G}}(\bar{r}, \bar{r}') \cdot \left(\hat{n} \times \bar{H}_{refl}(\bar{r}') \right) + \nabla \times \bar{\bar{G}}(\bar{r}, \bar{r}') \cdot \left(\hat{n} \times \bar{E}_{refl}(\bar{r}') \right) \right] dA' \qquad (2.17)$$

In the previous expression $\bar{\bar{G}}(\bar{r}, \bar{r}')$ is the free space Green's function in the far field region, $\hat{n}$ is the normal vector with reference to the surface element dA' of the façade and the "$refl$" subscript stands for local reflected field.

Thanks to that field decomposition the scattering pattern can be found simulating building façades with a numerical simulation routine through the Monte Carlo method, *i.e.*, doing several simulations in each of which façade parameterized dimensions are randomly varied (within defined intervals). Moreover the mean value and the standard deviation of the scattered field (2.17) over all realizations can be examined. This point is important because the scattered field can be represented as the superposition of two different contributions: the *coherent* mean field $\left\langle \bar{E}_s \right\rangle$ and the fluctuating (*incoherent*) part $\bar{E}_{s,f}$, for which holds $\left\langle \bar{E}_{s,f} \right\rangle = 0$.

$$\bar{E}_s = \left\langle \bar{E}_s \right\rangle + \bar{E}_{s,f} \qquad (2.18)$$

Computational results reported in [9] show the dependence of the scattered field from frequency, polarization and angle of incidence.

First of all it has been observed that the scattered power is concentrated in the neighborhood of the specular direction and moreover its contribution in the specular direction of reflection can be neglected (note that the scattered component is here considered as the incoherent contribution on the total received field).

Considering the incidence angle ϑ_i we can observe in figure 2.6 that for $\vartheta_i = 0$ the scattering is symmetric in both horizontal and vertical planes, as ϑ_i increases the scattering in the horizontal plane becomes more asymmetrical with respect to the specular direction.
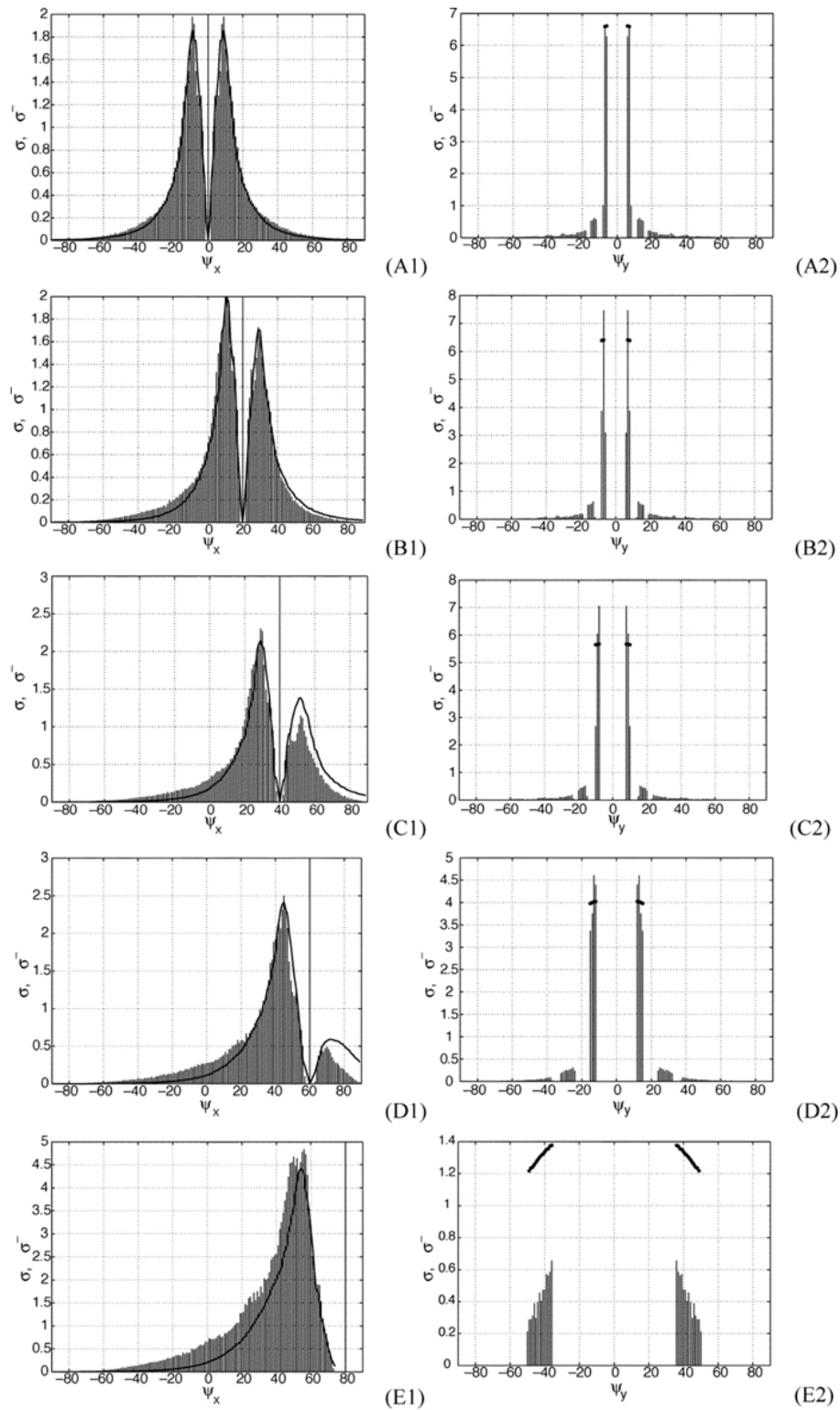
Figure 2.6: Scattering coefficient in horizontal (xz) and vertical (xy) planes at 900 [MHz] for TE polarization : A) $\vartheta_i = 0$ B) $\vartheta_i = 20°$ C) $\vartheta_i = 40°$ D) $\vartheta_i = 80°$.

As we can see in figure 2.7, when the impinging wave has TE polarization ($\Phi_i = 0$) the specular coherent power P_{co} increases as the angle of incidence approaches 90° (grazing incidence) while the incoherent power P_{nco} decreases. On the other hand, for TM polarization ($\Phi_i = 90°$), the specular power decreases until ϑ_i reaches the Brewster's angle, after which it increases; the non-specular power has the same trend as the previous case.

θ_i	f	$\phi_i = 0°$		$\phi_i = 90°$	
		P_{co}	P_{nco}	P_{co}	P_{nco}
0°	900MHz	6.50%	17.77%	6.50%	17.77%
	1GHz	6.64%	17.63%	6.64%	17.63%
	2GHz	6.00%	23.22%	6.00%	23.63%
	3GHz	6.62%	23.84%	6.62%	23.84%
	4GHz	6.48%	23.39%	6.48%	23.39%
20°	900MHz	7.10%	17.23%	5.17%	14.51%
	1GHz	7.20%	17.32%	5.50%	14.59%
	2GHz	6.54%	22.30%	5.81%	18.06%
	3GHz	7.04%	23.69%	5.12%	21.09%
	4GHz	7.01%	22.84%	5.96%	19.29%
40°	900MHz	9.95%	14.61%	3.17%	6.44%
	1GHz	9.47%	15.29%	3.17%	6.79%
	2GHz	9.44%	18.13%	3.99%	7.96%
	3GHz	8.77%	21.19%	3.47%	9.75%
	4GHz	9.63%	20.13%	3.46%	10.00%
60°	900MHz	15.59%	9.59%	2.40%	1.10%
	1GHz	15.96%	10.01%	0.28%	1.16%
	2GHz	15.05%	12.54%	0.57%	1.47%
	3GHz	15.41%	13.71%	0.79%	1.64%
	4GHz	14.51%	14.79%	0.73%	1.82%
80°	900MHz	40.30%	5.65%	7.51%	0.51%
	1GHz	40.01%	5.43%	7.36%	0.55%
	2GHz	39.04%	4.71%	6.08%	0.98%
	3GHz	39.83%	4.62%	6.24%	1.23%
	4GHz	33.44%	4.50%	5.89%	1.36%

Figure 2.7: Percentage of the incident power that is scattered into specular and non-specular directions.

Furthermore the frequency dependence has been analyzed; the frequency is supposed to vary from 900 [MHz] to 4 [GHz] (in this range of frequencies building dimensions are large compared to the wavelength). What has been observed is that as the frequency increases the angular width of the scattering coefficient gets narrower and with higher amplitude (see fig. 2.8). In terms of power these effects cancel each other, making their combined effect frequency-independent. In fact, as we can see in figure 2.7, the power in the specular direction is almost independent on frequency, while the incoherent power has only small variations. Finally, as a result of simulations, the scattering pattern is found to be limited to two cones (analogous to Keller's cones), which is different from the pattern expected for randomly rough surfaces.

This model, because of its general derivation, is surely useful to represent scattering in urban environments where a detailed description of the buildings isn't available. Compared to the previous analytical models it is evident that the complete physical understanding of the scattering phenomenon is overtaken by its large-scale modeling in a real-case scenario. We now start to understand that different approaches and applications may lead to results that really differ one to another depending on the context and on the considered typical scenario.
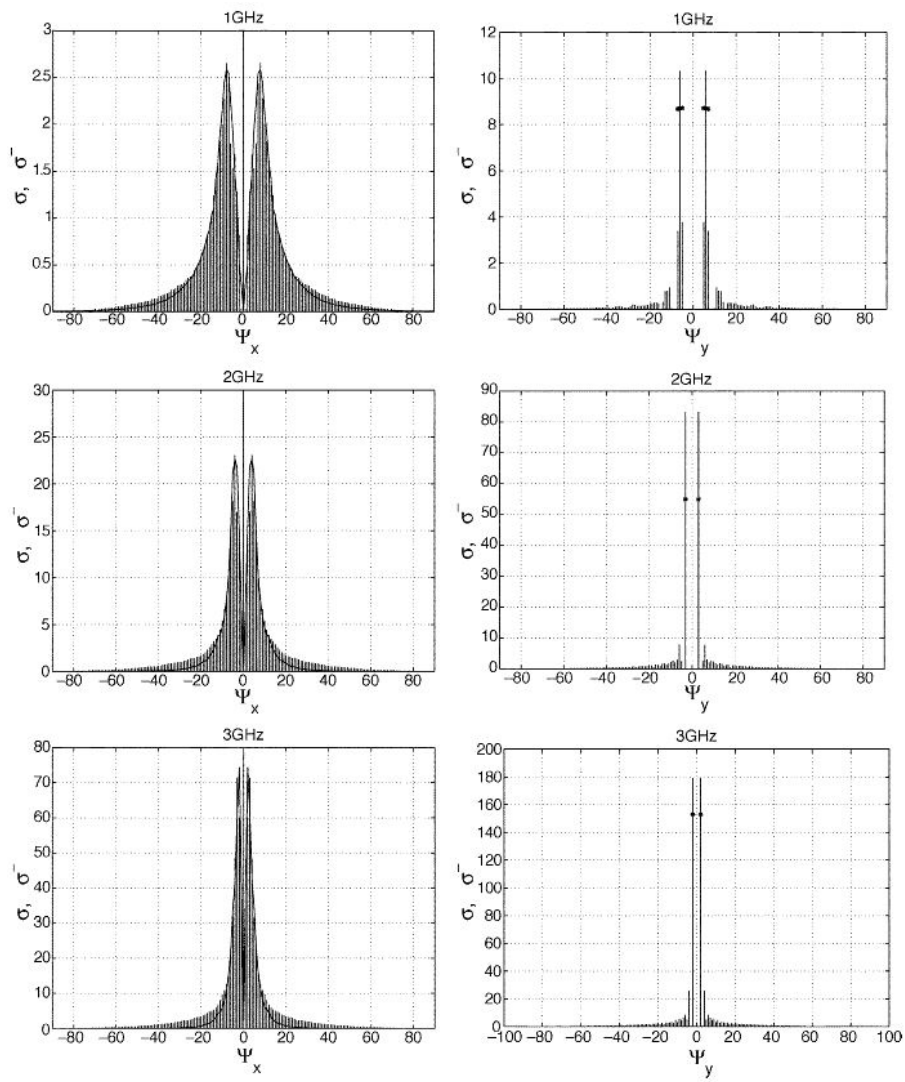
Figure 2.8: Frequency dependence of scattering coefficient in horizontal and vertical plane respectively.

2.2.4 Effective roughness model

As presented in [10] and [11] the *effective roughness* (ER) model is based on physical considerations concerning the electromagnetic wave-wall interaction mechanism. This model doesn't take into account only the real surface roughness, but also general wall irregularities in a mean way; in other words the scattering caused by real physical properties (surface height fluctuations, volume inhomogeneities, etc.) are modeled through a surface with characteristics that reflect the same scattering behavior as the real sample.

With this model it is possible to characterize both back and forward scattering respectively regarding the reflected and transmitted radiation; the field scattered by a surface element dS is modeled as a non-uniform, spherical wave springing from the element surface and propagating in the outer half-space according to a certain *scattering pattern* (see below).
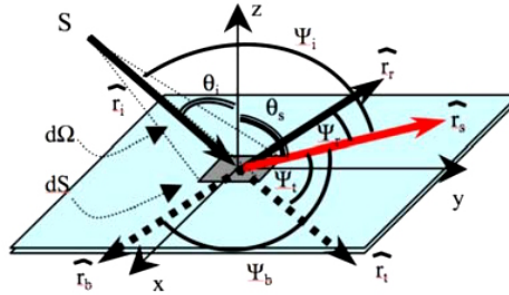
Figure 2.9: Reference system at the generic wall element for the ER model.

The key assumption of this model is that the transmitted power through the wall P_t is the same fraction of the incoming power P_i as in the case of smooth, homogeneous slab, *i.e.*, the ratio P_t/P_i is assumed independent of surface or volume irregularities.

Another consideration regards the scattered power in backward (P_{sr}) and forward (P_{st}) half-spaces, in fact with the ER model they can be simply expressed as a function of the incident field:

$$
\begin{aligned}
P_{sr} &= S_r^2 \cdot P_r \\
&= \int_\Omega S_r^2 \cdot |\Gamma|^2 \, \frac{|\bar{E}_i|^2}{2\eta} \, d\Omega \cdot r_i^2
\end{aligned}
\tag{2.19}
$$

$$
\begin{aligned}
P_{st} &= S_t^2 \cdot P_t \\
&= \int_\Omega S_t^2 \cdot |\tau|^2 \, \frac{|\bar{E}_i|^2}{2\eta} \, d\Omega \cdot r_i^2
\end{aligned}
\tag{2.20}
$$

Where S_r and S_t are the backward and forward scattering coefficient defined as the incoherent ratio of the scattered field with respect to the reflected one (cf. [10]). With this definition, S^2 is the percentage of the power which is scattered at the expenses of the reflected power.

Furthermore it is assumed that the scattered field follows a defined spatial power distribution, characterized with a certain scattering pattern. This function is assumed to be representative of the behavior of the considered sample with respect to the incident and, as the problem threats both half-spaces, it is composed of two sub-patterns: one for the backward and the other for the forward half-space. The two sub-patterns can be represented by one of the analytical functions given in [10]: *Lambertian model*, *directive lobe model* or *backscattering lobe model*.

Concerning the *Lambertian scattering pattern* the field amplitude follows (2.16), while for the *directive lobe function* the analytical formulation is given by:

$$
|\bar{E}_s|^2 = E_{s0}^2 \left(\frac{1 + \cos\psi_r}{2} \right)^{\alpha_r}
\tag{2.21}
$$

Where ψ_r is the angle between the direction of specular reflection and the scattering direction (ϑ_s, φ_s), whilst the exponent α_r is related to the width of the scattering lobe and E_{s0} is the maximum amplitude of the scattered field (that can be computed as expressed in [10]–[11]). As one can see in figure 2.10 the scattering lobe is then oriented toward the direction of the reflection (this in agreement with results obtained in [3] for random rough surfaces using the KA) with a directivity defined by the parameter α_r (to be found through a model fitting of experimental results) that depends on the specific specimen.
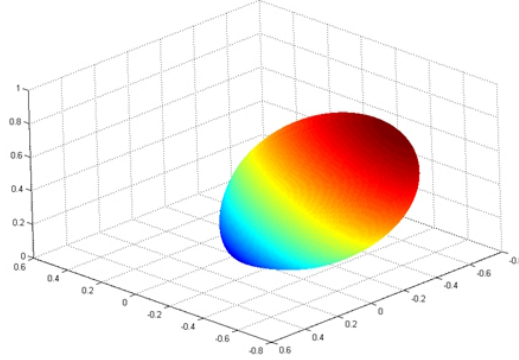
Figure 2.10: Directive model single-lobe of the ER model.

As said before, for a complete characterization, it is needed to find model parameters for each half space; for example it is necessary to determine the lobe directivity α_r for the backward-scattered component as well as α_t for the transmitted one.

The third and last scattering pattern is the so-called *backscattering lobe model*, where a certain part of the radiation is back-reflected around the transmission direction (see fig. 2.11). The expression of this pattern is:

$$|\bar{E}_s|^2 = E_{s0}^2 \left[\Lambda \left(\frac{1 + \cos \psi_r}{2} \right)^{\alpha_r} + (1 - \Lambda) \left(\frac{1 + \cos \psi_i}{2} \right)^{\alpha_i} \right] \qquad (2.22)$$

Where α_r, α_i refer to the specular reflection lobe and to the back-lobe width respectively and $\Lambda \in [0,1]$ is the repartition factor between the amplitudes of the two lobes.
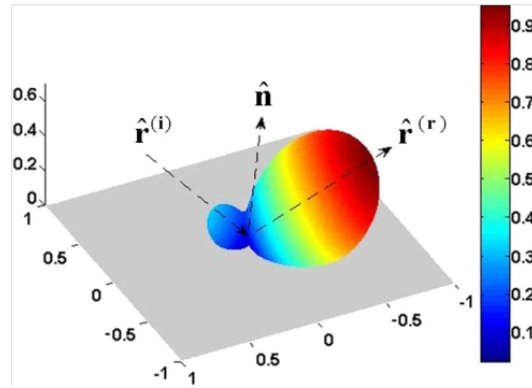
Figure 2.11: Backscattering double-lobe of the ER model.

In any of the previous cases the power balance at the generic wall element can be expressed as follows (cf. [11]):

$$\begin{aligned} P_i &= R_r^2 \cdot P_r + R_t^2 \cdot P_t + S_r^2 \cdot P_r + S_t^2 \cdot P_t \\ &= P_r \cdot \left(R_r^2 + S_r^2 \right) + P_t \cdot \left(R_t^2 + S_t^2 \right) \end{aligned} \qquad (2.23)$$

Where P_i is the incident power, P_r and P_t are the reflected and transmitted powers in the case of smooth and homogeneous slab, R_r and R_t are the Rayleigh factors, that take into account the loss of power in the specular reflection due to the presence of scattering, finally S_r and S_t have the same meaning as previously said. These last parameters have to be

determined by measurements, in fact they are the values that, when used in simulations, best fit experimental results.

Therefore is now easy to understand that the intensity of the scattered field depends on scattering coefficients S_r and S_t while its distribution in the spatial domain is defined by the scattering pattern function.

Moreover it becomes evident how the ER model is straightforward: starting from measurements one can express the scattered field by the use of analytical functions depending on few parameters. What is needed to be investigated is the assumption made on the transmitted power, namely the independence of the transmitted power from wall irregularities.

$$3$$

Electromagnetic characterization of materials

The interaction between the electromagnetic radiation and the environment depends on several factors such as frequency, wave polarization, the kind of material which the object is made, surface roughness, *etc.* (see 1). Therefore electromagnetic properties of materials have a high relevance when we want to give an accurate description of these phenomena.

In general the aim of all characterization methods is to estimate the complex permittivity ε_c of materials:

$$\varepsilon_c = \varepsilon' - j\varepsilon'' = \varepsilon_0 \varepsilon_r - j\frac{\sigma}{\omega} \tag{3.1}$$

Where ε_r is the relative permittivity, σ is the conductivity and $\omega = 2\pi f$ is the angular frequency.

Each kind of material has its own complex permittivity that depends on frequency, incident wave polarization (TE or TM), moisture content, *etc.* Several methods have been developed through the years to determine the complex permittivity, they can mainly divided in three categories:

1. Resonant cavities (monochromatic)

2. Transmission lines (narrow band)

3. Free space techniques (wide band)

   - Fresnel method
   - Reflection (or transmission) ellipsometry

Since we want to analyze wide band parameters and in the meanwhile we are also evaluating the diffuse scattering behavior of the sample (the measurement setup is almost the same), we will take into account only the third set of techniques mentioned above.

3.1 Fresnel method

The finite thickness wall is modeled as a *Fabry-Pérot cavity* (see fig. 3.1), this because several reflections-transmissions happen at wall interfaces introducing a fluctuating shape on the curves of each reflection coefficient modulus versus the angle of incidence. The reflection function of this kind of system is expressed by (3.2). In the following it is discussed only the reflection technique, but a similar reasoning can be obviously done for transmission coefficients.

$$\Gamma(f, \vartheta_i, \varepsilon_{cr}) = \frac{1 - \exp(-j2\beta)}{1 - \Gamma'^2 \exp(j2\beta)} \, \Gamma' \tag{3.2}$$

Where $\beta = e \cdot k_0 \sqrt{(\varepsilon_{cr} - \sin^2 \vartheta_i)}$ is the complex propagation factor through the sample slab, e is the thickness of the sample, $k_0 = 2\pi/\lambda_0$ is the free-space wavenumber, λ_0 is the free-space wavelength, $\varepsilon_{cr} = \varepsilon_c/\varepsilon_0$ is its relative complex permittivity and Γ' is the
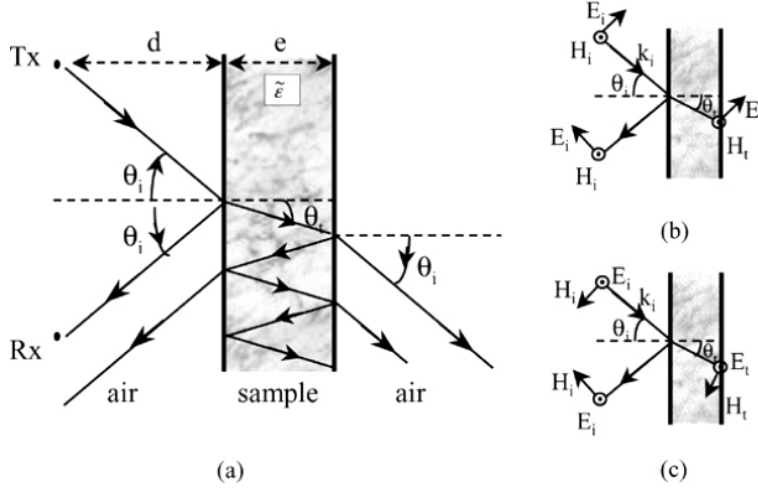
Figure 3.1: Fabry-Pérot cavity can model a finite-thickness wall, multiple reflections within a sample are represented.

reflection coefficient at the air-medium interface, defined as in (1.3) and (1.5) depending on the polarization.

As extracting the complex permittivity from this model could be not so easy for complex structures, it can be found that at the *Brewster's angle*[1] ϑ_B the Fabry-Pérot cavity can be modeled with the classic Fresnel coefficient for infinite thickness walls, thus the angular position of this minimum characterizes accurately the reflection on the first interface (cf. [12]).
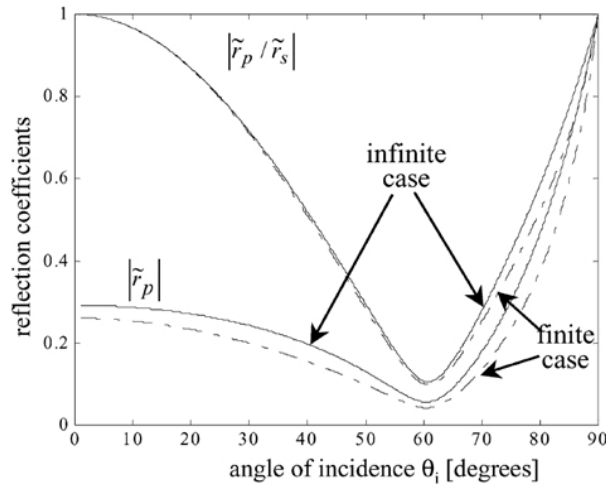
Figure 3.2: Theoretical curves of the moduli of the TM reflection coefficient $|\tilde{r}_p|$ and the ratio of both reflection coefficients $|\tilde{r}_p/\tilde{r}_s|$ in function of incidence angle in the case of finite or infinite thickness.

Thus is possible to estimate the complex permittivity starting from the measurements of Fresnel reflection coefficients for arbitrary angles of incidence for both TE and TM polarization. In fact, considering one of the two medium, as it actually is, as air we can write (1.3) and (1.5) in the following manner (cf. [12]):

$$\begin{aligned} \Gamma_{\text{TE}} &= \Gamma_{\perp} \\ &= \frac{\cos\vartheta_i - \sqrt{\varepsilon_{cr} - \sin^2\vartheta_i}}{\cos\vartheta_i + \sqrt{\varepsilon_{cr} - \sin^2\vartheta_i}} \end{aligned} \tag{3.3}$$

---

[1]The Brewster's angle is the the angle of incidence for which the reflection coefficient for TM polarization has the minimum modulus.

$$\Gamma_{\text{TM}} = \Gamma_{||}$$
$$= \frac{\sqrt{\varepsilon_{cr} - \sin^2 \vartheta_i} - \varepsilon_{cr} \cos \vartheta_i}{\sqrt{\varepsilon_{cr} - \sin^2 \vartheta_i} + \varepsilon_{cr} \cos \vartheta_i} \tag{3.4}$$

Then measuring the reflected field for both TE and TM polarization, as a function of the angle of incidence ϑ_i, one can find the coordinates of the minimum of the experimental curve $|\Gamma_{\text{TM}}/\Gamma_{\text{TE}}|^2$ (see fig. 3.2). Thanks to this it is possible to extract a first estimation of the complex permittivity from $|\Gamma_{\text{TM}}/\Gamma_{\text{TE}}|^2$ and, computing several values of real and imaginary parts of the complex permittivity, one can fit, using a nonlinear least square method, the theoretical expressions of either joint parallel (TM) and perpendicular (TE) reflection coefficients, or their ratio, to the measured data. Then the theoretical curve that best fits the measured data yields the optimum estimate of the complex permittivity. Summarizing this method adopts the following steps:

1. Determine the Brewster's angle ϑ_B

2. Extract a first estimation of the complex permittivity $\varepsilon_{cr}(\vartheta_B)$ from $|\Gamma_{\text{TM}}/\Gamma_{\text{TE}}|^2$ (or $|\Gamma_{\text{TM}}|^2$ and $|\Gamma_{\text{TE}}|^2$ jointly)

3. Several values of ε_{cr} are computed, to each of them is associated a curve of $|\Gamma_{\text{TM}}/\Gamma_{\text{TE}}|^2$ as a function of ϑ_i

4. Among these curves the one that fits at best (according to a least squares criterion) the measurement data is selected and its corresponding parameter is adopted as the best estimated value

In [12] is reported the full step-by-step procedure for the determination of the complex permittivity with additional considerations about sources of uncertainty and experimental issues.

Examples of measurement setups for Fresnel reflection and transmission coefficients are shown in figure 3.3 and figure 3.4 respectively.
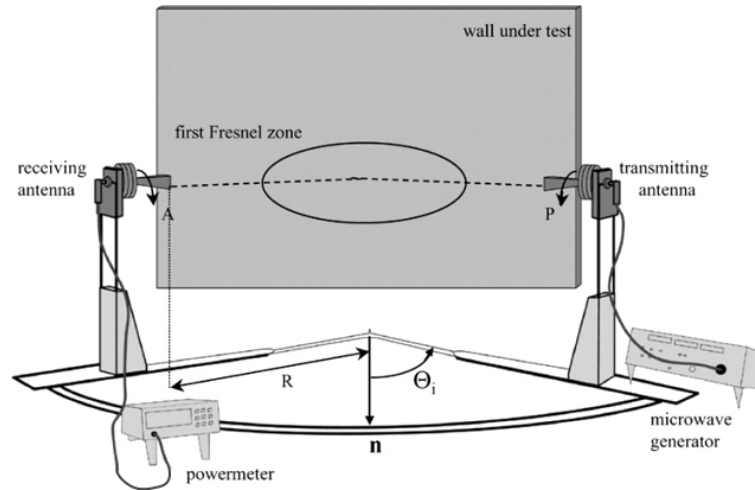
Figure 3.3: Possible measurement setup for reflection coefficient estimation with free space techniques.
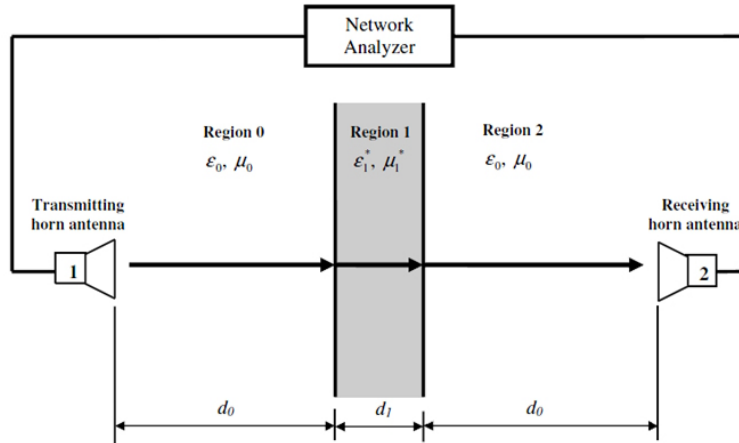
Figure 3.4: Possible measurement setup for transmission coefficient estimation with free space techniques.

3.2 Reflection (or transmission) ellipsometry

Reflection ellipsometry is a technique based on measurements of the change of polarization state (linear to elliptical) of an incident polarized electric field after its reflection on the air-sample interface for a fixed angle of incidence ϑ_i.

The setup is the same reported in figure 3.3. An antenna transmits a linearly polarized wave with a fixed polarization angle (P) with respect to the analyzed sample, the receiving antenna detects instead the power as a function of its own polarization angle (A). Then the maximum power P_{max} and the P_{min}/P_{max} ratio at the receiver, allow to estimate, thanks to the *fundamental relations of ellipsometry* (cf. [12]) the complex permittivity of the material under test.

3.3 Measurements of complex permittivity

The complex permittivity of two samples has been measured with an existing system developed at *CEA-Leti Grenoble* that uses a *vector network analyzer* (VNA) and a coaxial probe (see fig. 3.5a). Measurements have been done in the frequency range from 1 [GHz] to 10 [GHz]. First of all, each time the VNA is used, it is mandatory to calibrate it in open

(a) Measurement system
(b) Probe
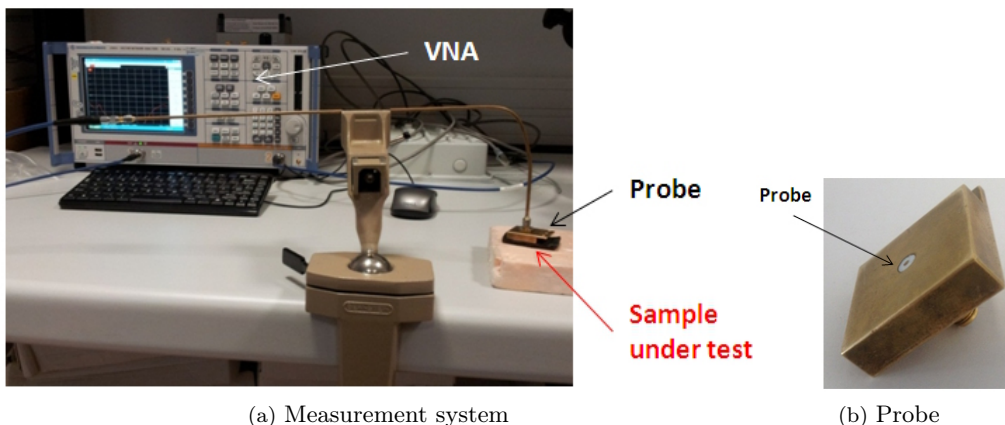
Figure 3.5: Setup used for complex permittivity measurements (a) and a detail of the coaxial probe (b).

circuit, short circuit and adapted load configurations. After the instrument calibration phase, three reference measurements are done on well-known materials in order to give a reference point to the measure we are going to do on our unknown sample. In our case these measurements have been done with distilled water, Teflon and air in the desired frequency

band. Finally measurements on real samples can be done. In our case we measured a brick wall covered with plaster on each side and a smooth sandstone slab. Results are reported in figures 3.6a–3.7b (page 32–33). Typical values of relative permittivity for the under test materials are:

- $3, 5 < \varepsilon_r < 5$ for the brick wall

- $2, 5 < \varepsilon_r < 6$ for plaster

- $3 < \varepsilon_r < 6$ for sandstone

Therefore our results are extremely compatible from what can be found in literature, however the measurements may have been affected by an error due to a non-perfect contact matching between the probe and the sample surface, thus the relative permittivity results might be underestimated.
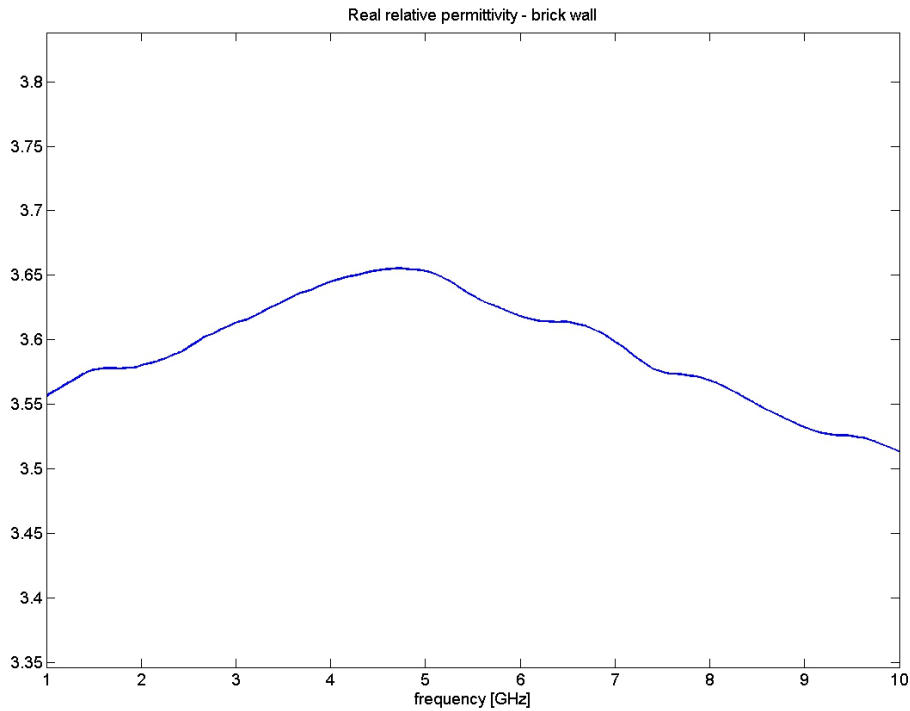
(a) Brick wall $-\varepsilon_r$
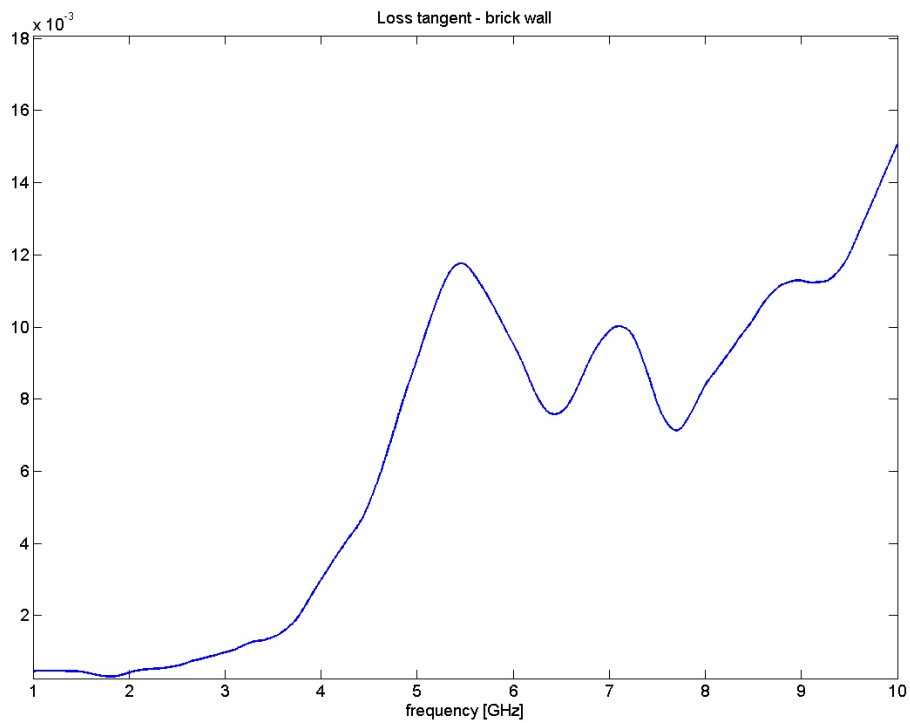
(b) Brick wall $- \tan\delta$

Figure 3.6: Measured permittivity (a) and loss tangent (b) of the brick wall. Note that $\tan\delta$ values have to be multiplied for 10^{-3}.
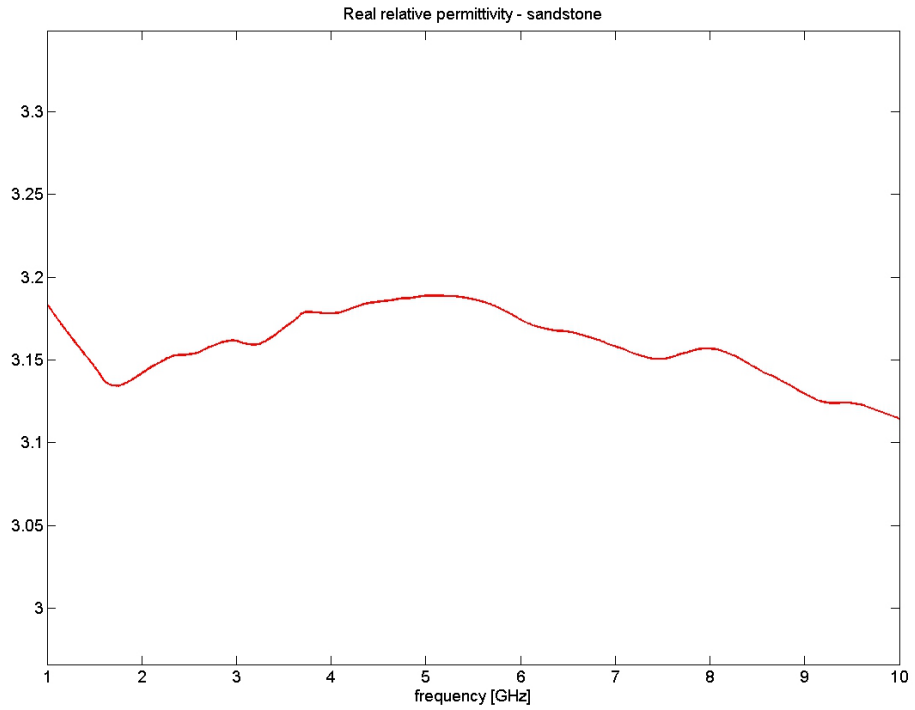
(a) Sandstone – ε_r
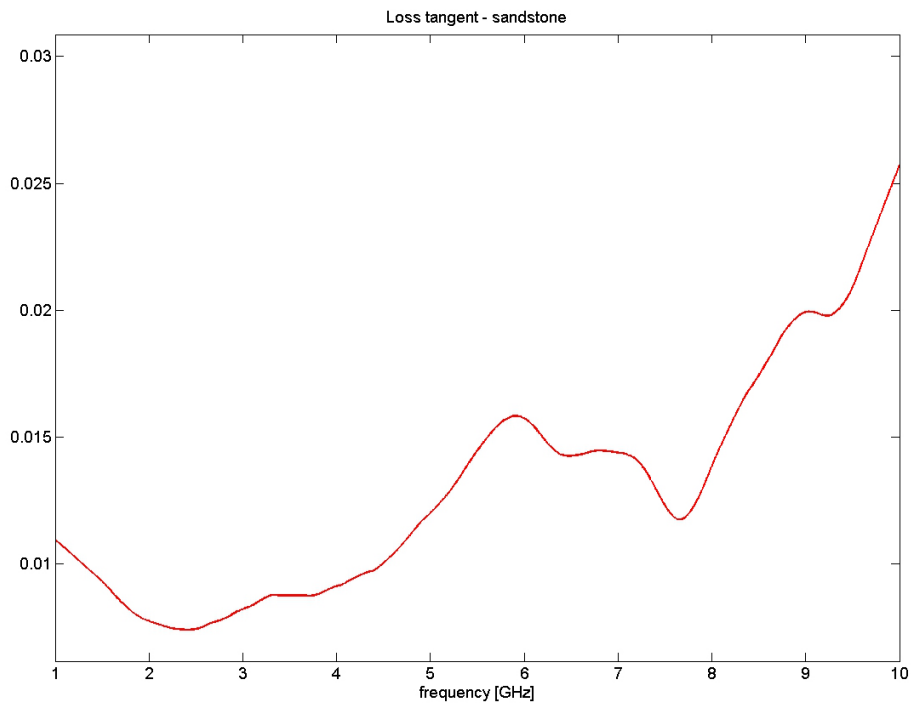
(b) Sandstone – $\tan \delta$

Figure 3.7: Measured permittivity (a) and loss tangent (b) of the sandstone slab.

Electromagnetic simulation of scattering from building materials

A part of this study concerns simulations with CST Microwave Studio$^{\text{TM}}$ (MWS) in order to reproduce the scattering behavior in real situations. First we have to take into account that the single simulation is nothing more than a realization of the statistical process, so our environment has to provide an effective setup that permits to repeat several iteration of the same statistical process without adding complexity. Furthermore, due to the complexity and the large variety of man-made building artifacts, several kinds of objects and even their dimensions need to be considered and parameterized.

Obviously building up a database of all construction materials and techniques to be included in a simulation software is something quite far from being possible. According to this a huge simplification has been done in our case, considering only the most relevant kinds of construction materials and methods. For each kind of artifact or surface most of the things are configurable, from its dimensions to the material and number of elements.
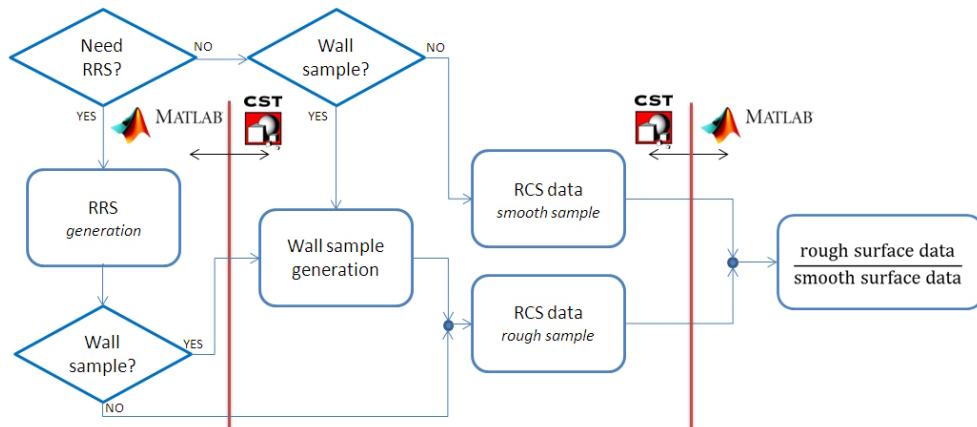
Figure 4.1: Flowchart of the developed simulation process for 3D scattering characterization.

4.1 Numerical electromagnetic simulation overview

The commercial software used in our work is a general-purpose electromagnetic simulator based on the *Finite Integration Technique* (FIT) (see [13]). This numerical method provides a spatial discretization scheme applicable to various electromagnetic problems ranging from static field calculations to high frequency applications in time or frequency domain, preserving the basics of the continuous equations such as conservation of charge and energy.

Unlike standard *Finite Difference Time Domain* (FDTD) methods FIT discretizes the integral form of Maxwell's equations rather than the differential seen in (2.1)–(2.4). To

solve these equations numerically, one must define a finite calculation domain, enclosing the considered application problem. Creating a suitable mesh system splits this domain up into many small elements or grid cells and then the spatial discretization of Maxwell's equations is finally performed on this grid system (at each cell facet separately) where the degrees of freedom are introduced as integral values.

Obviously the spatial discretization introduces inevitable numerical inaccuracy, in fact, when defining the necessary relations between voltages and fluxes, material relations integral values have to be approximated over the grid edges and cell areas respectively. Consequently, the resulting coefficients depend on the averaged material parameters as well as on the spatial resolution of the grid. Thanks to the FIT several kinds of meshes can be applied to the problem depending on discretization needs: orthogonal hexahedral grids are the more usual, but other mesh types such as topologically irregular grids (subgrids) and tetrahedral grids can be adopted.

(a) Hexahedral mesh   (b) Tetrahedral mesh
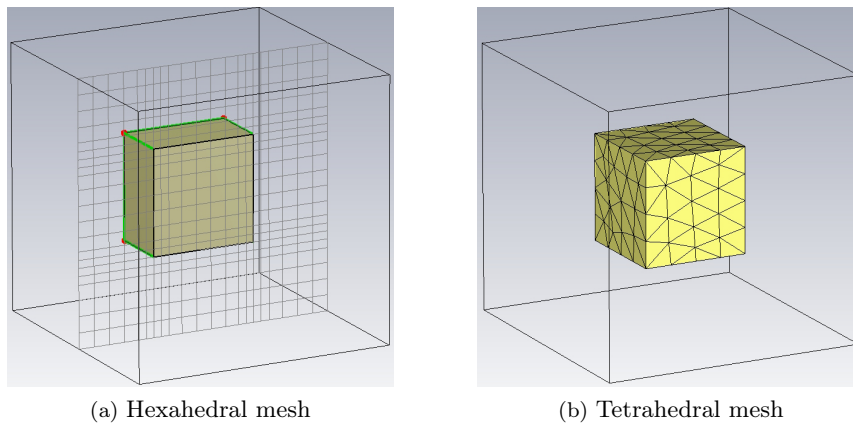
Figure 4.2: Example of hexahedral and tetrahedral grids for the same specimen.

In the case of Cartesian grids, the FIT formulation can be rewritten in time domain to yield FDTD, however, classical FDTD methods are limited to staircase approximations of complex boundaries.

Furthermore different kinds of solver can be used: in 4.4 and 4.5 the *time domain solver* has been adopted, while in 4.6 we utilized the *frequency domain solver*. These choices are problem-depending and differ quite strongly one to the other.

The *time domain solver* calculates the development of fields through time at discrete locations and at discrete time samples defined by geometrical details (the grid seen before) and simulation frequency bandwidth. It calculates the transmission of energy between the ports and/or open space of the investigated domain and it stops once signals energy gets lower of a certain level.

On the other hand the *frequency domain solver* considers the problem for a single frequency at a time (then Maxwell's equations may be transformed in the phasors domain) and for a number of adaptively chosen frequency samples in the course of a frequency sweep over the desired band. For each frequency sample, the linear equation system is solved by an iterative or sparse direct solver. Then the software interpolates missing results among simulated frequencies in the whole bandwidth and the simulation stops when the error associated to a chosen parameter (or more) falls down a preset threshold.

4.2 Building material under test

4.2.1 Random rough surfaces

The first step in generating random rough surfaces is to implement what discussed in 1.4 into a numerical computing software (in our work we used MathWorks - MATLAB). In literature several papers [14]–[16] deal with the problem of numerical generation of random rough surfaces, as this topic doesn't only concerns scattering characterization, but a large variety of physical systems and models.

The technique adopted in this work is the one described in [14]: briefly a matrix constituted by elements which represent the random height in that point is first generated according to a Gaussian distribution; after that a certain spatial correlation, one of (1.30) or (1.31), is introduced by multiplying, in the spatial transform domain, the Fourier transform of the before generated matrix with the transform of the correlation function. Doing the inverse Fourier transform of this quantity a surface with the desired spatial correlation is obtained. The generation of two dimensional profiles is done in the same way as described above, except for the fact that one has to work with one dimensional array instead of matrices.

In figure 4.3a and figure 4.3b the z axis reports the normalized autocorrelation of the generated surfaces represented in figure 1.9a and figure 1.9b respectively (all lengths are expressed as fraction of wavelength).
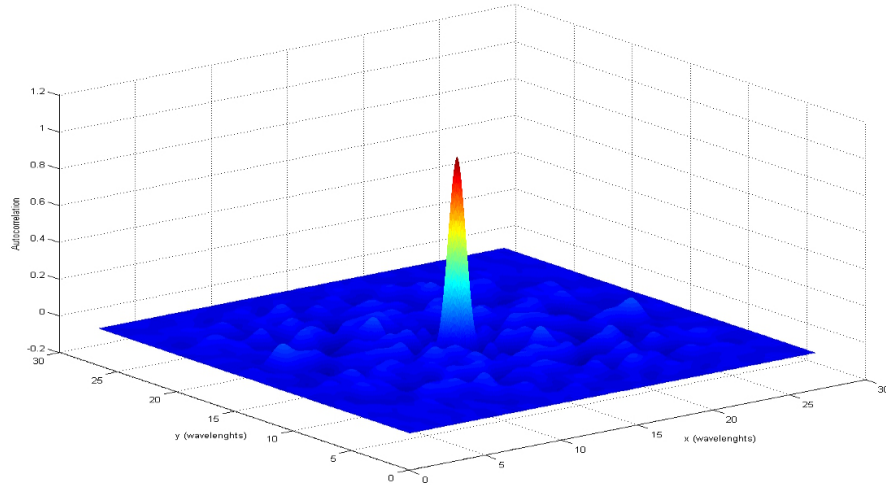
(a) Gaussian correlation
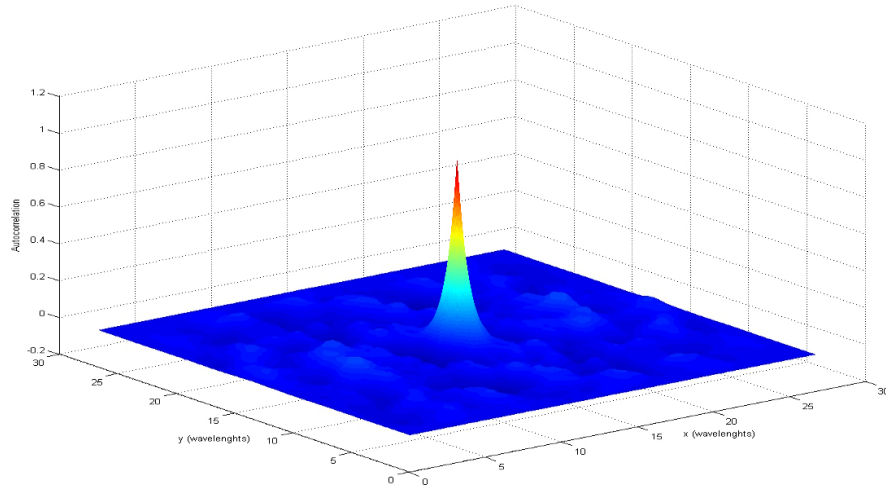
(b) Exponential correlation

Figure 4.3: Gaussian and exponential spatial autocorrelation functions with correlation length $= \frac{2}{3}\lambda$.

In figure 4.4a and figure 4.4b is reported the cut of the previous graphs along the x direction. In this manner we can verify if the effective correlation length, defined as the value of length for which the normalized autocorrelation falls below $\exp(-1)$, of the generated surface corresponds to the desired one (fixed *a priori*). As one can see, in both cases it is the same as the wanted.
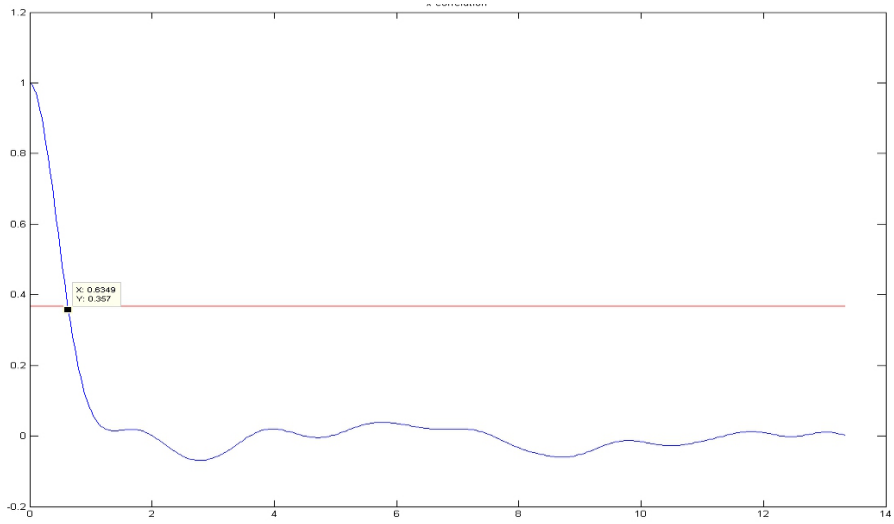
(a) Gaussian correlation
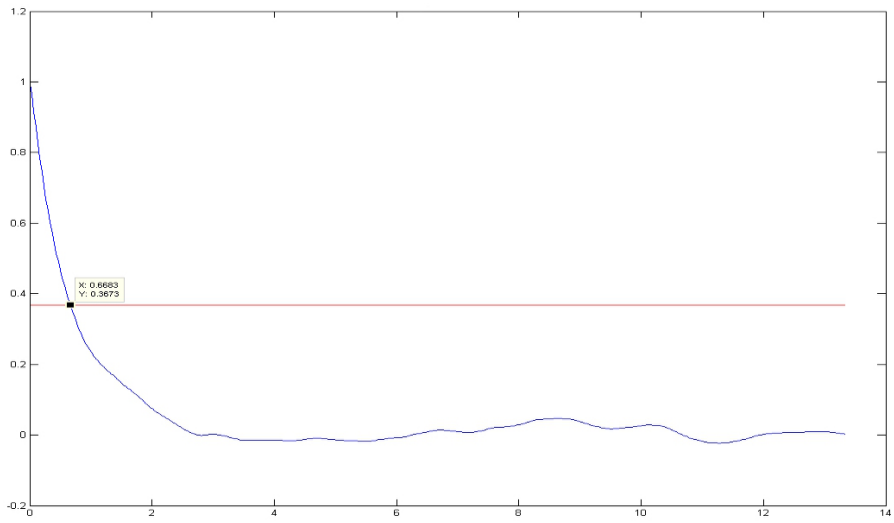
(b) Exponential correlation

Figure 4.4: Detail of the Gaussian and exponential spatial autocorrelation functions of figures 4.3a–4.3b along x direction with correlation length $= \frac{2}{3}\lambda$.

Summarizing, when one generates a RRS with the developed routine, degrees of freedom are:

1. Number of points by which the surface is composed (depending on dimensions and on the desired spatial resolution)

2. Standard deviation of roughness heights

3. Kind of spatial correlation function between peaks and valleys (Gaussian or exponential)

4. Correlation length

Once the surface has been generated in MATLAB it is imported in CST MWS and constructed with a macro that creates an array of connected polygons according to the imported matrix dimensions. An example of a generated surface with a Gaussian statistics of both heights and correlation length can be seen in figure 4.5b.

(a) Smooth surface   (b) RRS
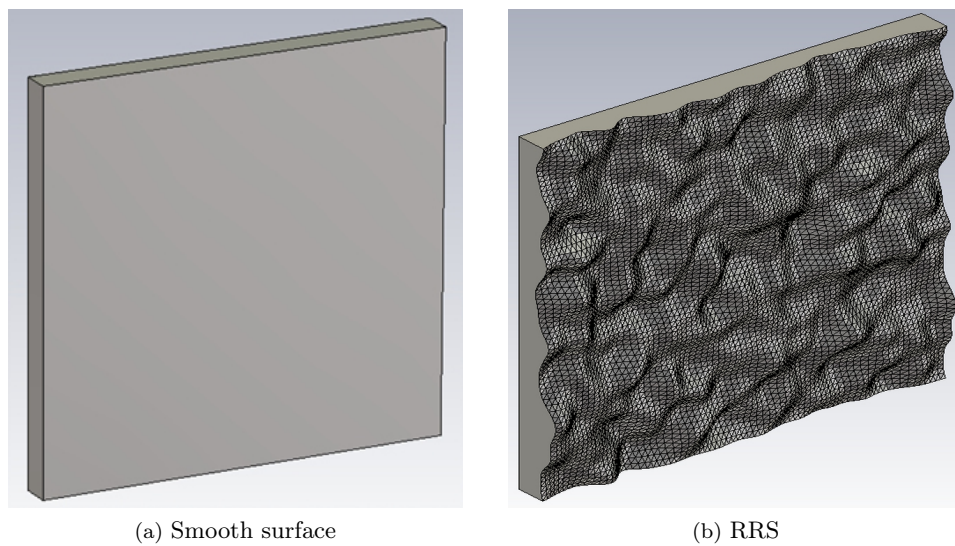
Figure 4.5: Gaussian RRS generated in CST MWS with our macro (b) in comparison with a smooth surface (a).

Moreover all samples that we will discuss in the following can be combined with this random rough surface in order to consider both volume and surface irregularities.

4.2.2 Brick walls

Another kind of sample that can be studied is a wall made of bricks stuck together with a mortar layer. This *macro* permits to set several parameter of the wall, in particular:

1. Dimensions and characteristics of wall and bricks (width, height and thickness)

2. Number of holes in each brick

3. Thickness of the material of which the brick is made

4. Thickness of the mortar layer

According to these constraints the wall is automatically generated.
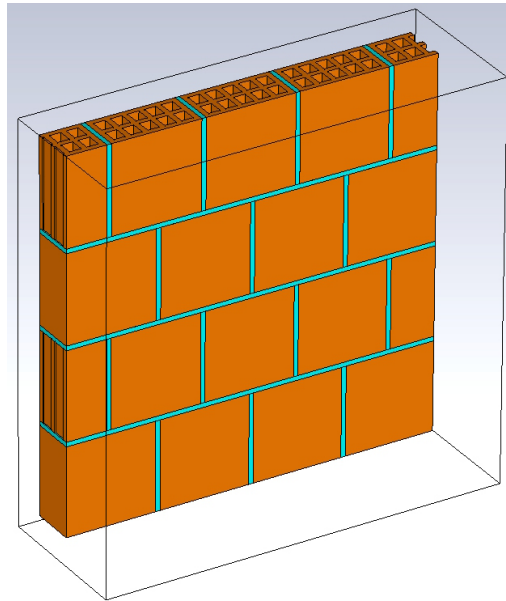
Figure 4.6: Hollow bricks wall generated in CST MWS with the developed macro.

4.2.3   Plasterboard

Plasterboard is one of the most used kinds of wall for interior construction. A plasterboard wall is essentially constituted by an interior skeleton, made with metallic rails, where two layers of plastered material are attached. A representation is given in figure 4.7a–4.7b.

(a)   (b)
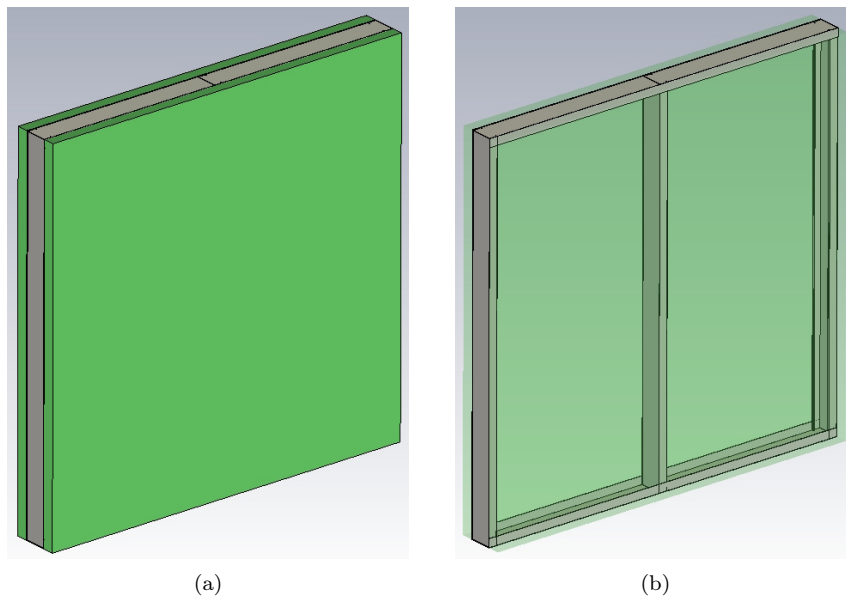
Figure 4.7: Plasterboard wall (a) and a detail of the metallic structure (b).

As before, even with this macro is possible to tune several wall characteristics:

1. Dimensions of the wall and plasterboard (width, height and thickness)

2. Thickness of the material of which the metallic structure is made

4.2.4   Reinforced concrete

Reinforced concrete is one of the most used composite materials in buildings construction thus, in order to take it into account, another parametrized macro has been developed in

CST MWS.

(a)   (b)
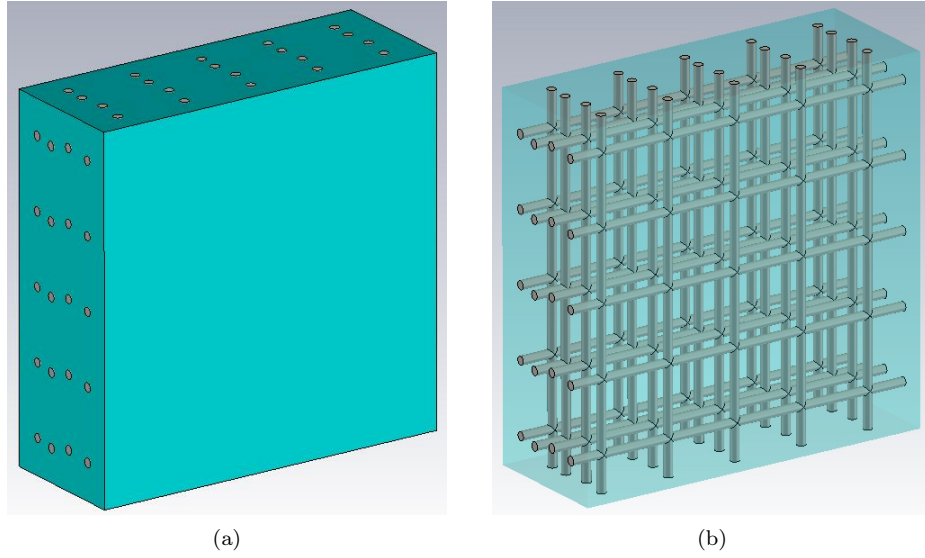
Figure 4.8: Reinforced concrete wall (a) and a detail of the internal mesh (b).

As well as before, several parameters can be setted:

1. Dimensions and characteristics of the wall (width, height and thickness)

2. Dimension of squares side that constitute the mesh

3. Thickness of the material of which the metallic mesh is made

4. Number of mesh layers

5. Possibility to have only vertical or horizontal elements in the mesh

6. The disposition of the mesh into the wall can be randomly varied

4.3 Theoretical behavior

4.3.1 Effect of roughness

When an electromagnetic wave impinges on a real construction, in the hypothesis of plane incident wave, we have to consider that the coherent phase addition of the contribution from inside the first Fresnel zone will be partially destroyed by the random surface and also the cancellation due to the successive Fresnel zones will no longer take place to the same degree. As said in the previous paragraphs (in particular in 1.3 and 2.1) this phenomenon depends by the size and nature of surface roughness and/or volume irregularities.

As well explained in [2] and [17] diffuse scattering has an incoherent nature, this because it's the sum of many micro-reflection and diffraction contributions from the irregularities and the periodic structures in the wall. As a result diffuse scattering can be considered as a random phase term $\bar{E}_{incoh}$, which gives rise to a zero-mean signal but with a non-zero scattering power.

$$\mathbb{E}\left[\bar{E}_{incoh}(\vartheta_s, \varphi_s)\right] \quad = \quad 0 \tag{4.1}$$

$$\begin{aligned} \mathbb{E}\left[\bar{E}^2_{incoh}(\vartheta_s, \varphi_s)\right] &= P_{incoh} \\ &\neq 0 \end{aligned} \tag{4.2}$$

Thanks to (1.16) and energy conservation, the incident power P_i can be obtained summing up together powers of coherent reflection and transmission components and incoherent

scattering contributions:

$$P_i = P_{r,\,coh} + P_{r,\,incoh} + P_{t,\,coh} + P_{t,\,incoh} \tag{4.3}$$

Where P_r refers to the reflected component, P_t is the transmitted one (including power dissipations in lossy mediums) and the terms "coh" and "incoh" refer to the coherent or incoherent contribution respectively (see 1.3).

4.3.2 Connection between simulation results and diffuse scattering

The results that we need from time domain simulations with CST MWS are the bi-static *Radar Cross Sections* (RCS) for one incoming wave direction at a fixed frequency and polarization. Thus, for the incidence direction (ϑ_i, φ_i), the scattered field is evaluated in the whole spatial domain:

$$
\begin{aligned}
RCS_{p,\,q}(\vartheta_s, \varphi_s)\big|_{\vartheta_i,\,\varphi_i} &= \lim_{r \to \infty} 4\pi r^2 \frac{|E_{rx}^q(\vartheta_s, \varphi_s)|^2}{|E_i^p|^2} \\[2mm]
&= \lim_{r \to \infty} 4\pi r^2 \frac{|E_{rx}^q(\vartheta_s, \varphi_s)|^2}{|E_i^p|^2} \cdot \frac{2\eta}{2\eta} \\[2mm]
&= \lim_{r \to \infty} 4\pi r^2 \frac{S_{rx}^q(\vartheta_s, \varphi_s)}{S_i^p}
\end{aligned}
\tag{4.4}
$$

The RCS is a far-field parameter that determines the scattering properties of a specific target. It represents a complex parameter depending on the incident wave properties such as polarization, propagation angle, operation frequency and the target itself (geometry, material characteristics). In the previous equation $S_{rx}^q(\vartheta_s, \varphi_s)$ is the received power density in the scattering direction defined by ϑ_s and φ_s with q polarization, while S_i^p is the power density impinging on the wall surface with p polarization. Simulations parameters are: $f = 10\,[\text{GHz}]$, variable angle of incidence ϑ_i and linear (TE or TM) polarization.

4.3.3 Smooth wall

First a reference simulation with a smooth and homogeneous wall is done, thus to have the behavior of an ideal situation. Moreover its electromagnetic characteristics, such as complex permittivity, have to take in account the overall mean behavior of the system that we want to analyze.

In this case the received power in both backward and forward half-spaces is due only to coherent components, so we can write:

$$RCS_{p,\,q}(\vartheta_s, \varphi_s)\big|_{\vartheta_i,\,\varphi_i}^{smooth} = 4\pi r^2 \frac{S_{rx,\,smooth}^q(\vartheta_s, \varphi_s)}{S_i^p} \tag{4.5}$$

$$S_{rx,\,smooth}^q(\vartheta_s, \varphi_s) = S_{r,\,coh}^q + S_{t,\,coh}^q \tag{4.6}$$

As one can imagine the reflected and transmitted components refer to the backward and forward half-spaces respectively, *i.e.*, in the backward half-space we have only reflected contributions while in the forward half-space we have only transmitted ones.

4.3.4 Rough wall

In the case of a rough surface the diffuse component could be relevant and has to be taken into account in the power balance. In this case we have:

$$RCS_{p,\,q}(\vartheta_s, \varphi_s)\big|_{\vartheta_i,\,\varphi_i}^{rough} = 4\pi r^2 \frac{S_{rx,\,rough}^q(\vartheta_s, \varphi_s)}{S_i^p} \tag{4.7}$$

$$S_{rx,\,rough}^q(\vartheta_s, \varphi_s) = S_{r,\,coh}^{'\,q} + S_{r,\,incoh}^q + S_{t,\,coh}^{'\,q} + S_{t,\,incoh}^q \tag{4.8}$$

The reflected and transmitted coherent components are here considered different to the case of the smooth surface, this because these contributions are in general roughness-dependent. In fact the coherent component for a rough surface can be viewed as a reduction on average of the specular reflected component in case of a smooth surface (cf. [17]), where the average is to be interpreted as an ensemble average over many surfaces obeying the same statistics.

4.3.5   Contributions relationship

According to what seen before we can relate the received power to the different scattered components, in this way we'll have a sort of power balance that takes into account all the contributions.

   The idea is to give a sort of transfer function in a statistical way (several roughness realizations for each kind of structure), thus to have a simple tool to implement in a radio coverage estimation software.

$$
\begin{aligned}
\frac{RCS_{p,\,q}(\vartheta_s,\varphi_s)|_{\vartheta_i,\,\varphi_i}^{rough}}{RCS_{p,\,q}(\vartheta_s,\varphi_s)|_{\vartheta_i,\,\varphi_i}^{smooth}} &= \left.\frac{\left|E_{rx,\,rough}^q\left(\vartheta_s,\varphi_s\right)\right|^2}{\left|E_{rx,\,smooth}^q\left(\vartheta_s,\varphi_s\right)\right|^2}\right|_{\vartheta_i,\,\varphi_i} \\[2ex]
&= \left.\frac{S_{rx,\,rough}^q\left(\vartheta_s,\varphi_s\right)}{S_{rx,\,smooth}^q\left(\vartheta_s,\varphi_s\right)}\right|_{\vartheta_i,\,\varphi_i} \\[2ex]
&= \zeta\left(\vartheta_s,\varphi_s\right) \quad\quad\quad (4.9)
\end{aligned}
$$

In (4.9) we made the assumption that S_{inc} on the target is the same in case of smooth and rough surface. For one incoming wave direction (ϑ_i,φ_i) in the *backward half-space* the following expression holds:

$$
\left.\frac{S_{rx,\,rough}^q\left(\vartheta_s,\varphi_s\right)}{S_{rx,\,smooth}^q\left(\vartheta_s,\varphi_s\right)}\right|_{\vartheta_i,\,\varphi_i} = \frac{S_{r,\,coh}^{'q}+S_{r,\,incoh}^q}{S_{r,\,coh}^q} = \zeta_r\left(\vartheta_s,\varphi_s\right) \quad\quad (4.10)
$$

While in the *forward half-space* it is:

$$
\left.\frac{S_{rx,\,rough}^q\left(\vartheta_s,\varphi_s\right)}{S_{rx,\,smooth}^q\left(\vartheta_s,\varphi_s\right)}\right|_{\vartheta_i,\,\varphi_i} = \frac{S_{t,\,coh}^{'q}+S_{t,\,incoh}^q}{S_{t,\,coh}^q} = \zeta_t\left(\vartheta_s,\varphi_s\right) \quad\quad (4.11)
$$

Analyzing several realizations in which we keep constant parameters that characterize the surface roughness (standard deviation of heights and correlation length) we are able to extract an observed variance of measured values reported above. This leads to the understanding of parameters deviation around their mean value.

$$
\sigma^2\left[\zeta\left(\vartheta_s,\varphi_s\right)\right] = \frac{1}{N-1}\cdot\sum_{i=1}^{N}\left[\zeta_i\left(\vartheta_s,\varphi_s\right)\right]-\bar{\zeta}\left(\vartheta_s,\varphi_s\right)]^2 \quad\quad (4.12)
$$

$$
\bar{\zeta}\left(\vartheta_s,\varphi_s\right) = \frac{1}{N}\cdot\sum_{i=1}^{N}\zeta_i\left(\vartheta_s,\varphi_s\right) \quad\quad (4.13)
$$

Where, for each (ϑ_s,φ_s), σ^2 is the observed variance, ζ_i is the *i-th* simulated value of $\left.\frac{S_{rx,\,rough}^q(\vartheta_s,\varphi_s)}{S_{rx,\,smooth}^q(\vartheta_s,\varphi_s)}\right|_{\vartheta_i,\,\varphi_i}$ and $\bar{\zeta}$ is the mean value of these ratios.

   One fact that has to be taken into account is that when we compute (4.13) in fact we are evaluating the variance of the ratio between rough and smooth cases, so it is composed by a random part, namely the roughness contribution, and a constant one, that is the smooth contribution (used as reference case). A fundamental property of variance is:

$$
\sigma^2 = [a\cdot X] = a^2\cdot\sigma^2\left[X\right] \quad\quad (4.14)
$$

Where a is a constant and X is the random variable. In (4.9) the random variable is the power profile detected for each simulation with rough surfaces, while the constant is the normalizing pattern $S^q_{(rx,\,smooth)}(\vartheta_s, \varphi_s)$ obtained in the unique case of smooth surface.

Extracting the square root of (4.13) it is possible to evaluate the *standard deviation*, namely the deviation around the mean value of several realization of the process:

$$\zeta(\vartheta_s, \varphi_s) = \bar{\zeta}(\vartheta_s, \varphi_s) \pm \sigma(\vartheta_s, \varphi_s) \qquad (4.15)$$

Where $\sigma(\vartheta_s, \varphi_s) = \sqrt{\sigma^2(\vartheta_s, \varphi_s)}$ is the standard deviation.

The idea is then to evaluate in which manner irregularities (both superficial and volumetric) scatter the impinging electromagnetic wave in the spatial domain. In fact with (4.10) and (4.11) is possible to understand, over several realizations, how the power is distributed in the backward and forward half-spaces with reference to the case of a smooth and homogeneous slab. The uncertainty over this estimation is given by the standard deviation, namely from the square root of (4.13). In this way a relation between the scattered power in case of smooth and rough surfaces is defined in the whole spatial domain.

However a problem may occur when we normalize with respect to the smooth surface RCS in (4.9). In fact it could be that for certain spatial directions (ϑ_s, φ_s) the RCS values obtained in the case of smooth surface are very low compared to the case of rough surfaces and, according to (4.14), this leads to high values of the standard deviation.

4.4 Simulations results

In this section we analyze *time domain simulations* in order to see the effect of roughness on the scattered field: a reference simulation is first done with a smooth and homogeneous slab and then five RRSs for each surface statistics are simulated and compared to it. Subsequently all results are averaged and their observed standard deviation is also evaluated.

In table 4.1 is reported the set of all parameters that have been used to generate RRSs, for each correlation length/standard deviation couple five surfaces have been generated. Note that λ refers to the highest simulation frequency, that in our case is $f_{max} = 10\,[\text{GHz}]$ ($\lambda = 0.03\,[\text{m}]$).

SURFACES					
Set 1	*correlation length* $- c_l$	λ			
	standard deviation $- 3\sigma$	$\lambda/4$	$\lambda/2$	$(3/4)\lambda$	λ
Set 2	*correlation length* $- c_l$	$\lambda/2$	λ	$(3/2)\lambda$	2λ
	standard deviation $- 3\sigma$	$\lambda/2$			

Table 4.1: Set of statistical parameters that have been used to generate the simulated RRSs.

These values have been chosen considering plausible levels of roughness for building materials or, in a wider way, for handmade structures according to the simulated sample dimensions. In fact, thanks to the Gaussian distribution of heights chosen to generate the RRS, this means that the 99.7% of heights variations from the mean value are under 3σ, where σ is the standard deviation of heights; so in the "most rough" case ($3\sigma = \lambda$) these variations are lower than $3\,[\text{cm}]$ (maximum peak-to-peak variation $\approx 6\,[\text{cm}]$).

Correlation lengths have been chosen in order to have a correct statistics for the simulated wall of 0.4m×0.4m×0.03m (its dimensions are a good compromise between simulation time and size compared to the wavelength).

The adopted reference system is shown in figure 4.9: it is centered on the wall element, $\vartheta \in [0, \pi]$ is the elevation angle while $\varphi \in [0, 2\pi]$ is the azimuth; reflection and transmission directions comes directly from (1.1) and (1.2).

Backward half-space	$-\dfrac{\pi}{2} \leq \varphi < \dfrac{\pi}{2}$
Forward half-space	$\dfrac{\pi}{2} \leq \varphi < \dfrac{3}{2}\pi$
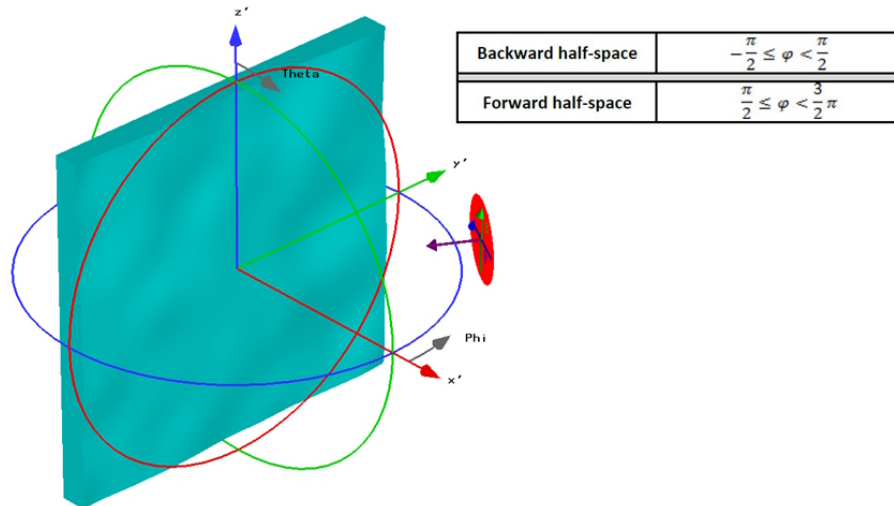
Figure 4.9: Simulations reference system, $\varphi \in [0, 2\pi]$ starts from x axis (red) while $\vartheta \in [0, \pi]$ starts from z axis (blue).

For each surface the RCS is then obtained in the range $[2.4 - 10]$ GHz for a fixed incidence direction and polarization. Material electromagnetic characteristics are the one measured for the sandstone as reported in 3.3. In figure 4.10 is represented the RCS of the
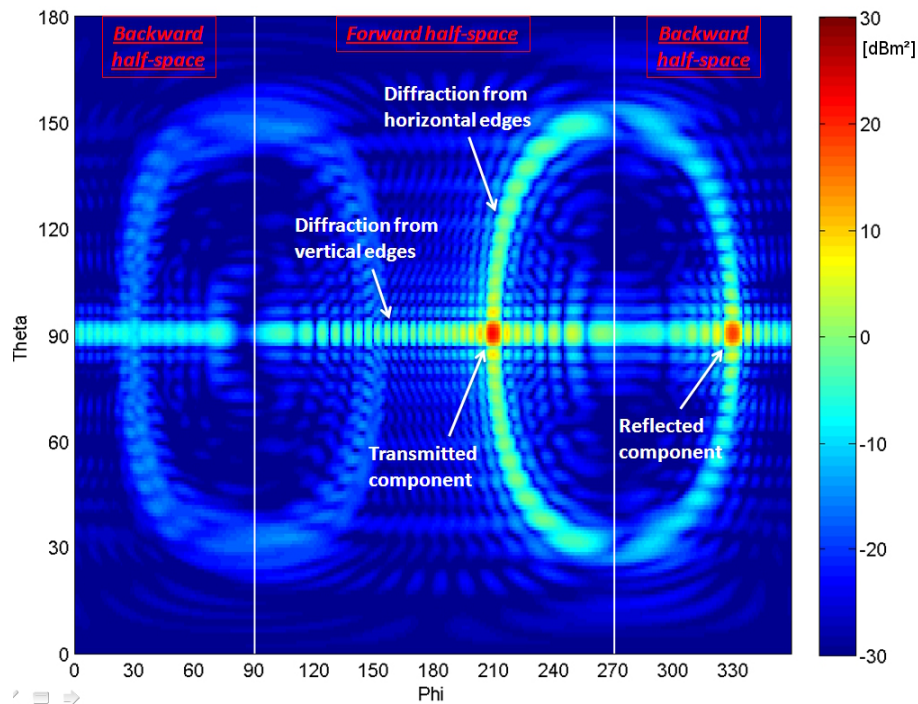
Figure 4.10: RCS [dBm^2] for the reference smooth wall, incidence angle $\varphi_i = \pi/6$ and $f = 10\,[\text{GHz}]$

smooth reference wall, it is clear that its maximum values are in reflection and transmission directions, moreover, due to the infinite incident plane wave extension and finite sample dimensions, diffraction happens in each edge of the wall. For horizontal edges this generates the Keller's cone pattern around transmission and reflection directions while for vertical edges the Keller's cone degenerates in the $\vartheta = \frac{\pi}{2}$ plane.

4.4.1   Results for RRS with $c_l = \lambda$ and $3\sigma = \lambda/2$

The same simulation has been done for a RRS with correlation length $c_l = \lambda$ and standard deviation of heights $3\sigma = \lambda/2$, its RCS is shown in figure 4.11.

It is notable that the reflected component in the specular direction of incidence (the coherent component) is attenuated of several [dB] with respect to the smooth-wall case, moreover the power is spread in the whole spatial domain both in the forward and backward half-spaces as an effect of surface roughness. The effect of edges diffraction tends also to disappear, because now this contribution is the coherent sum of all random local generated waves on the sample sides and they don't follow a regular interference pattern as seen before. Therefore surface roughness has three main effects:

1. Attenuation of the coherent reflected component

2. The scattered field spreads around the specular direction of reflection and transmission

3. Border diffraction changes its regular pattern (Keller's cones are dramatically modified)

Another important thing to notice when comparing figure 4.10 and figure 4.11 is that the scattering phenomenon takes place around reflection and transmission directions in an extended angular domain and not only in the "principal" plane $\vartheta = \pi/2$, this is one important result on scattering characterization because suggests that 3D analysis methods could be better than 2D models. One thing that has to be taken in account is that the
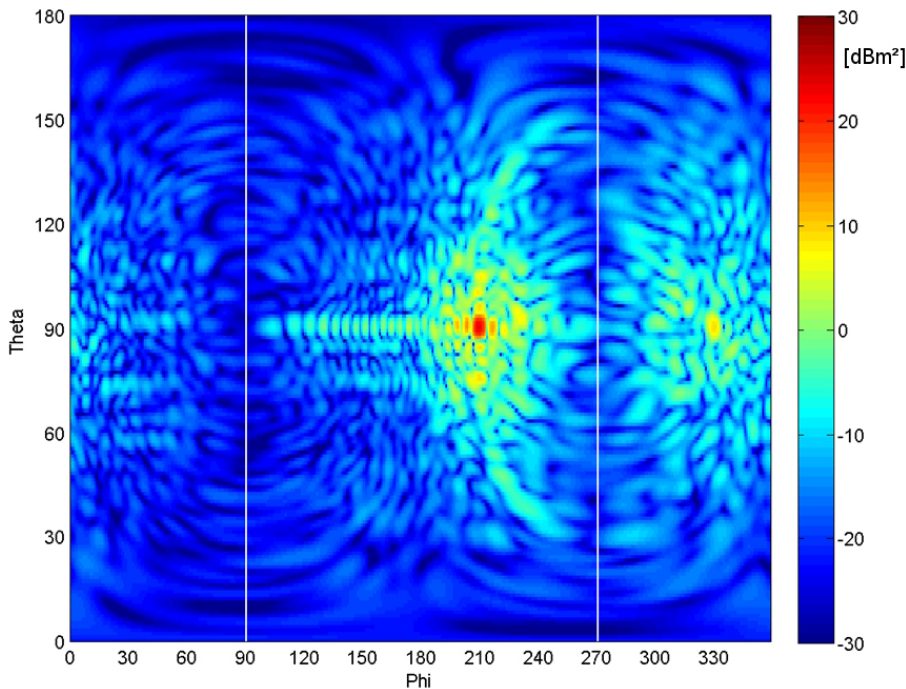
Figure 4.11: RCS [dBm^2] for a rough surface with $c_l = \lambda$ and $3\sigma = \lambda/2$.

strong component in the specular direction of transmission is due to the fact that in simulations the impinging plane wave has an infinite extension, while the sample has finite dimensions.

Doing the difference between RCS [dBm^2] in the case of rough and smooth surface one

can obtain the quantities seen in 4.3.

$$\zeta\left(\vartheta_s,\varphi_s\right) \quad = \quad RCS_{rough}(\vartheta_s,\varphi_s)|_{\mathrm{dBm}^2} - RCS_{smooth}(\vartheta_s,\varphi_s)|_{\mathrm{dBm}^2}$$

$$= \quad 10\log\left.\frac{\left|E^q_{rx,\,rough}\left(\vartheta_s,\varphi_s\right)\right|^2}{\left|E^q_{rx,\,smooth}\left(\vartheta_s,\varphi_s\right)\right|^2}\right|_{\vartheta_i,\,\varphi_i} \tag{4.16}$$

In the following we will show the mean in [dB] of these differences (4.17) and their standard deviation in [dBm^2] over five simulations (4.18).

$$\bar{\zeta}\left(\vartheta_s,\varphi_s\right) \quad = \quad \frac{1}{N}\cdot\sum_{i=1}^{N}\zeta_i\left(\vartheta_s,\varphi_s\right) \tag{4.17}$$

$$\sigma\left[\zeta\left(\vartheta_s,\varphi_s\right)\right] \quad = \quad \sqrt{\frac{1}{N-1}\cdot\sum_{i=1}^{N}\left[\zeta_i\left(\vartheta_s,\varphi_s\right)\right]-\bar{\zeta}\left(\vartheta_s,\varphi_s\right)]^2} \tag{4.18}$$

Simulations have been done with incidence angle $\varphi_i = \pi/6$, the mean and standard deviation over five surfaces following the same statistics have been analyzed. Applying (4.17) we obtained figure 4.12, from which some considerations can be done about the effect of the rough surface on the scattered field.
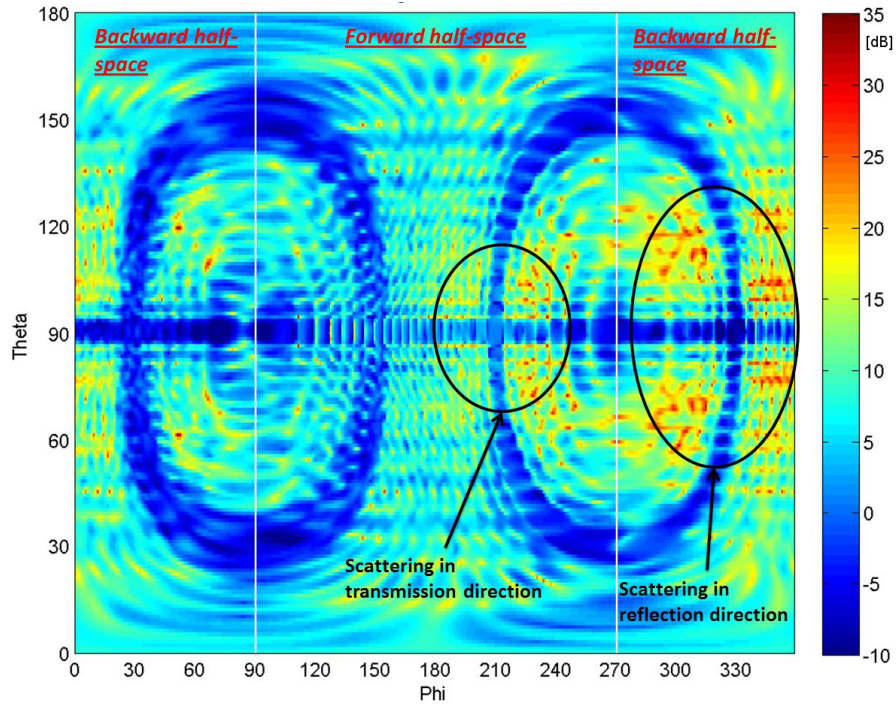
Figure 4.12: Surface roughness contribution in [dB] (mean value of (4.16) over five surfaces) for an incidence direction $(\vartheta_i,\varphi_i) = (\pi/2,\pi/6)$.

With reference to the smooth wall, the surface roughness attenuates the specular reflected component while contributions around it stand out. The same phenomenon of "spatial field spreading" happens also in the forward half-space, but the transmitted component isn't attenuated like in the reflection case and even scattering seems less significant than in the backward half-space. The effect of edges diffraction, in particular the presence of Keller's cones, almost disappears in the rough case, in fact these components are attenuated of approximately 5 [dB]. It is important to comprehend that this last effect can be primarily due to irregularities on borders more than in the surface, but since each edge, wedge or vertex in a real building could be rough (or more generally with an irregular geometry,

e.g., roof tiles) this is an important consideration that can be taken into account for future works.

In figure 4.13 the standard deviation (4.18) over five simulations is reported, it equals also the standard deviation of $RCS_{rough}(\vartheta_s, \varphi_s)|_{\text{dBm}^2}$.
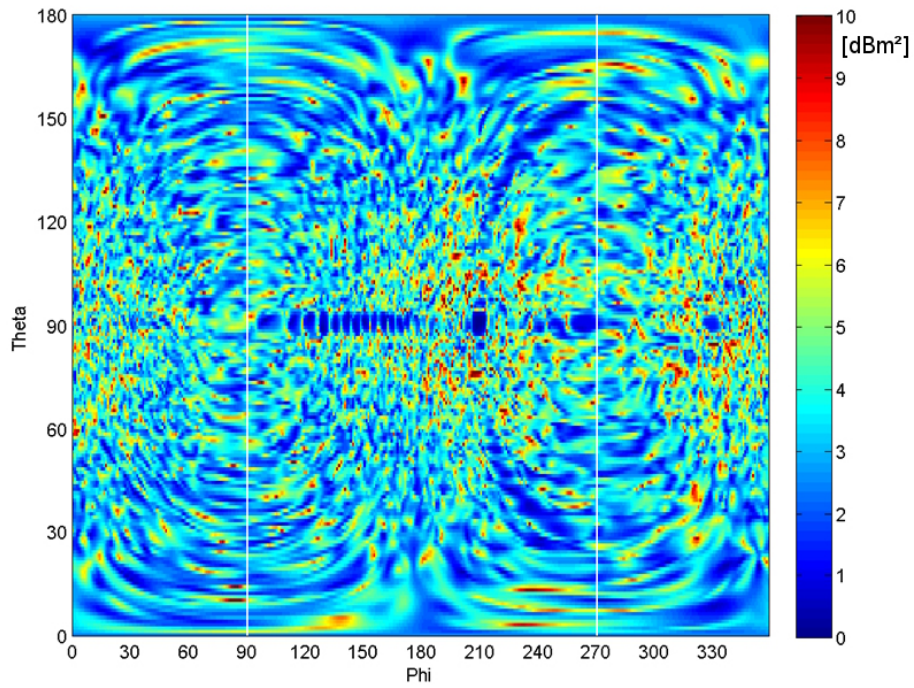
Figure 4.13: Standard deviation in [dBm^2] of (4.16) for $(\vartheta_i, \varphi_i) = (\pi/2, \pi/6)$.

4.4.2   Frequency analysis

An analysis over different frequencies has been done in order to have an idea on how scattering changes according to this parameter; even if simulations have been done in the [2.4 − 10] GHz band, results are reported in figure 4.14 for 2.4 [GHz] , 6 [GHz] and 10 [GHz] for reasons of space. The rough surfaces considered in this paragraph are the same as 4.4.1, so $c_l = \lambda$ and $3\sigma = \lambda/2$. It is clear that scattering becomes more important
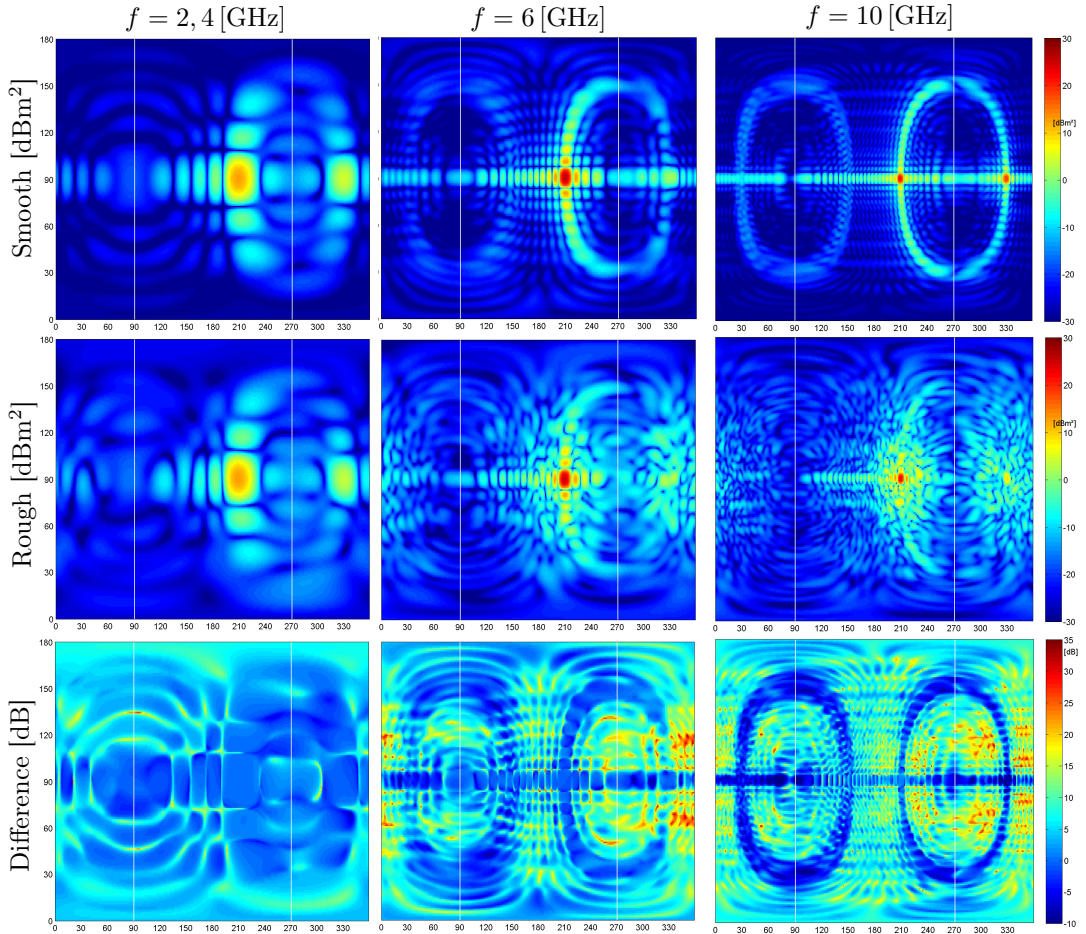
Figure 4.14: RCSs in function of frequency.

when the wavelength comes closer to irregularities dimensions, while differences between RCSs in case of smooth and rough surface at lower frequencies may be more influenced by irregular edges, because the most relevant differences are in peripheral areas compared to higher frequencies.

4.4.3 Standard deviation of heights effect

Another parameter that surely influences the scattered field is the standard deviation of heights σ, so the level of irregularities has been varied maintaining constant the correlation length c_l in order to evaluate only its contribution.

Results are reported in figure 4.15 where is represented (4.17) for each statistics (see table 4.1 Set 1) in function of frequency, incidence angle is always $\varphi_i = \pi/6$.
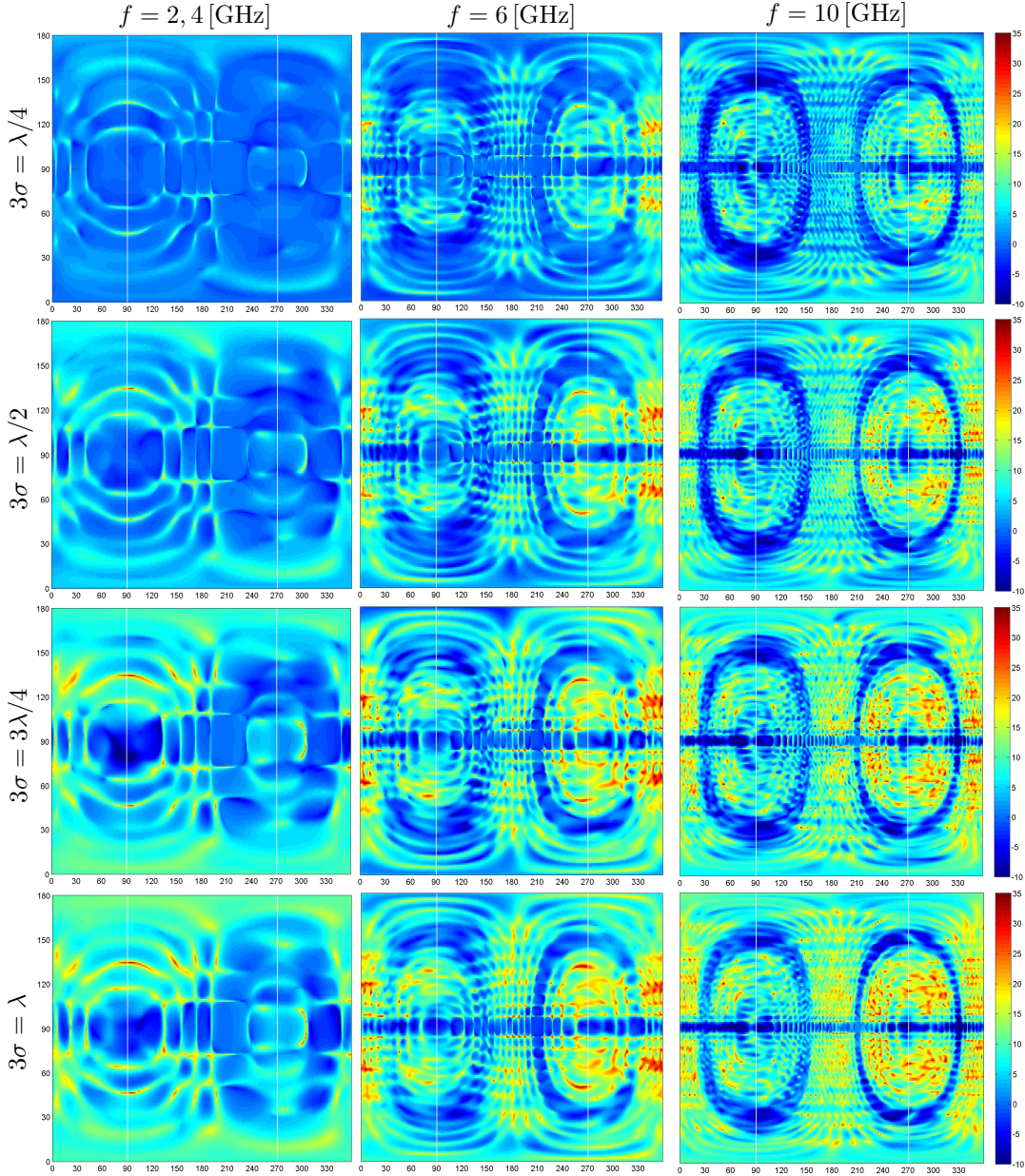
Figure 4.15: Representation of (4.17) in [dB] for correlation length of $c_l = \lambda$ and incidence angle $\varphi_i = \pi/6$.

As clear there is a direct proportionality between the increase of the standard deviation of heights and the higher level of scattering, moreover we observe the same frequency dependence seen before and the same considerations hold. Obviously when we analyze samples with a high standard deviation of heights we have that also diffracted components by the sides gets farer to the case of smooth surface with straight edges, so what reported in the previous figures is a combination of both rough border and surface effects.

4.4.4   Correlation length effect

According to what done in 4.4.3 for the standard deviation of heights another analysis has been conducted to find out the effect of the correlation length on the scattered field, this in order to give a complete description on how each tunable parameter can affect the overall pattern. Surfaces follow now the statistics represented in table 4.1 Set 2, where standard deviation of heights is maintained constant while the correlation length is varied; these results are reported in figure 4.16 and represent (4.17) for the same set of frequency seen before.
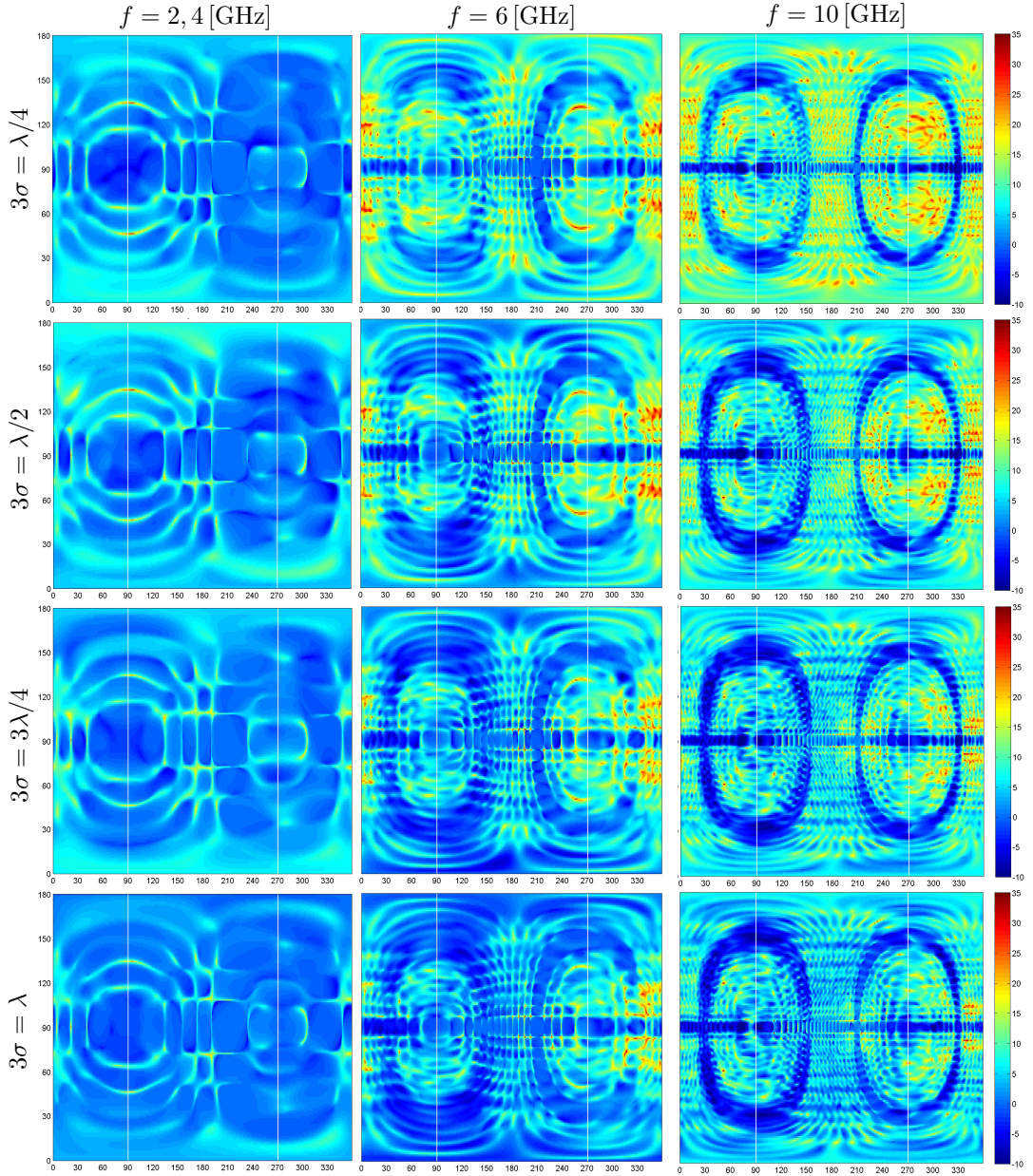
Figure 4.16: Representation of (4.17) in [dB] for $3\sigma = \pi/2$ and incidence angle $\varphi_i = \pi/6$.

As expected as the correlation length gets longer the surface appears less rough; in fact this means that with the same standard deviation of height, namely the height from the bottom of valleys to the top of peaks, irregularities are more separated and then slopes among them tend to be more gently, this results in a surface with less irregular elements as the correlation length rise.

4.5 Effect of volume heterogeneities

We have previously seen how surface roughness influences the scattered field, it could be interesting to analyze if even in presence of volume inhomogeneities the assertion that scattering in the back-ward half space is more relevant than in the forward half-space still holds. To do this two different samples have been simulated, a wall made of hollow bricks (fig. 4.17a) and a reinforced concrete slab (fig. 4.17b). As previously did, obtained results have been normalized with respect to a smooth and homogeneous wall made of the same material and having the same dimensions as the simulated one, in this way we obtain only the irregularities contribution.

(a) Bricks wall   (b) Reinforced concrete wall
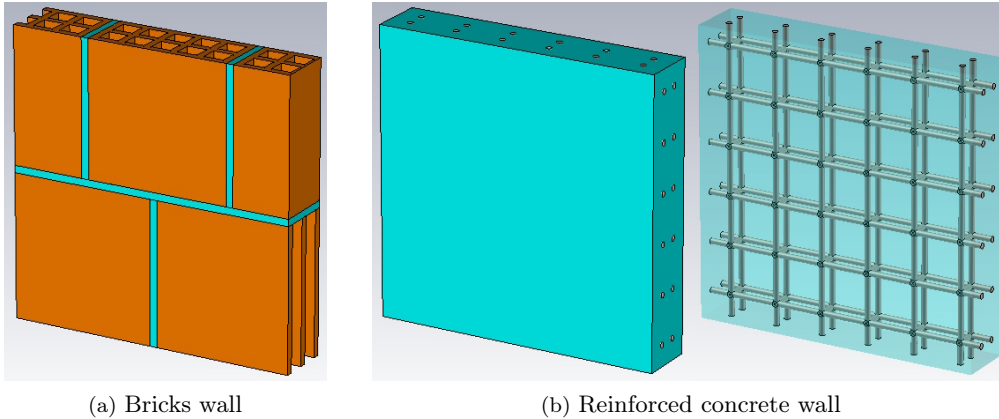
Figure 4.17: Simulated samples for the estimation of volume irregularities effects.

Wall samples have dimensions of $0.4\text{m} \times 0.4\text{m} \times 0.08\text{m}$, each brick is $0.2\text{m} \times 0.2\text{m} \times 0.08\text{m}$ with ten cavities of $0.028\text{m} \times 0.025\text{m}$ all along its height and the concrete wall has two internal equispaced metallic meshes with $92\,[\text{mm}]$ side.

4.5.1 Bricks wall

In this paragraph we will analyze the brick wall sample reported in figure 4.17a. It is constituted by hollow bricks of $20\text{cm} \times 20\text{cm} \times 8\text{cm}$ (which electromagnetic materials parameters are the same measured in 3.3) and among them there is a 1 [cm] thick mortar layer as in the reality.

RCSs in case of smooth and homogeneous wall, real brick wall and their ratio (4.16) are reported in function of frequency for an incidence angle $\varphi_i = \pi/6$ are reported in figure 4.18 (the reference system is the same as before, see fig. 4.9).

In these cases it can be noticed that there is not such a correlation between irregularities and the back-scattered field, in fact, when considering the brick wall, the RCS pattern changes considerably in every direction and not only in the vicinity of reflected and transmitted components as before in case of rough surface only. Therefore we can say, with reference to these first simulations, that anything can be stated about the spatial correlation that could exist between volume irregularities and the scattered field.

Moreover geometrical properties of the structure, such as air-cavities dimensions, surely affect field propagation through it and then we have a stronger dependence on physical parameters that may vary case-by-case.
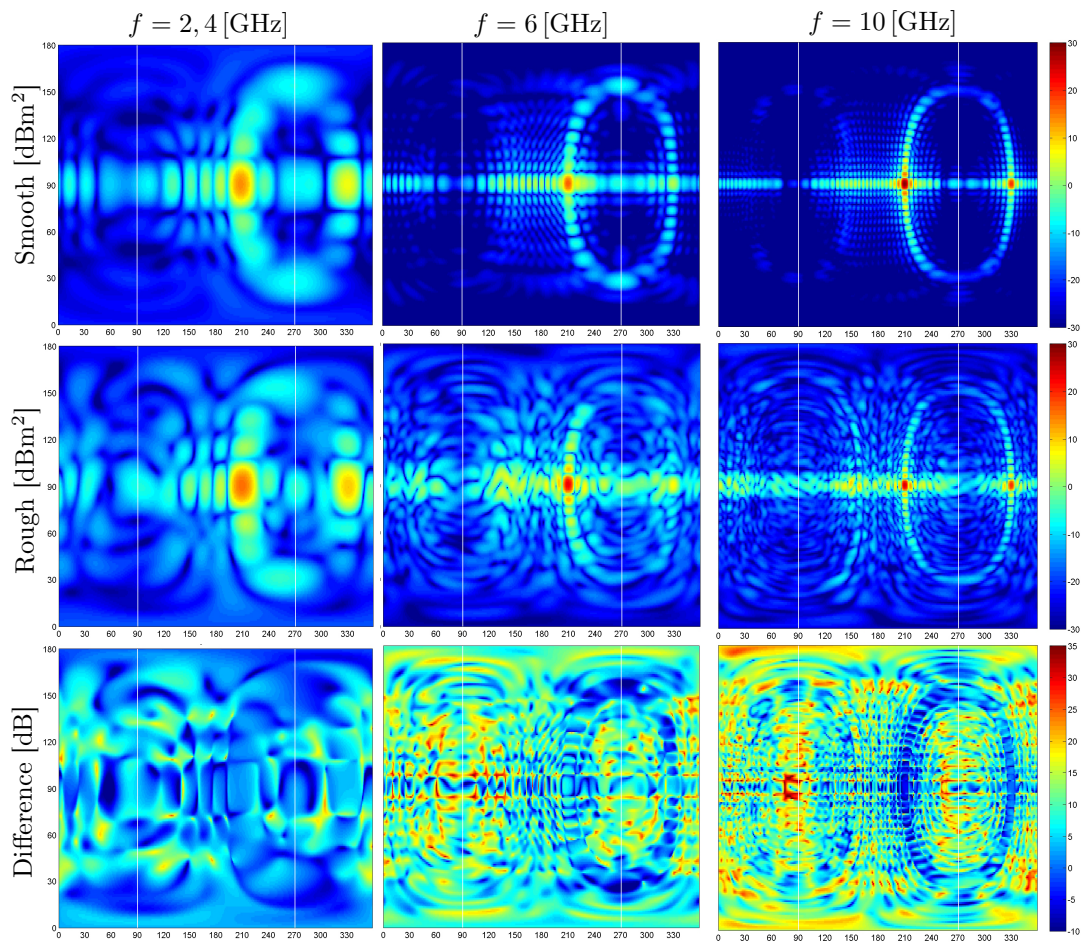
Figure 4.18: Volume irregularities RCSs analysis in case of brick wall.

4.5.2 Reinforced concrete wall

Concrete electromagnetic properties are $\varepsilon_r = 5.5$ and $\sigma = 0.013\,[\mathrm{S/m}]$ and have been picked up from CST MWS material library; the simulated reinforced concrete wall has been generated with two metallic meshes having an internal side of 92 [mm].

The same workflow as before has been applied to simulations, so RCSs in case of smooth, reinforced concrete wall and their difference (4.16) have been extracted.

As discussed before for the brick wall, in case of volume effects, internal geometry could influence the scattered field. In this case the internal metallic mesh has a strong impact on the RCS and cells dimension could also affect the structure frequency response (resonances, irradiations, *etc.*). Even in this case results haven't shown any evident correlation between volume inhomogeneities and the concentration of scattering around particular directions. It is important to remark that all these analysis are preliminary, so further works are necessary to state something more accurate on this topic; however we wanted to show the different behavior and complexity of scattering when considering volume irregularities.
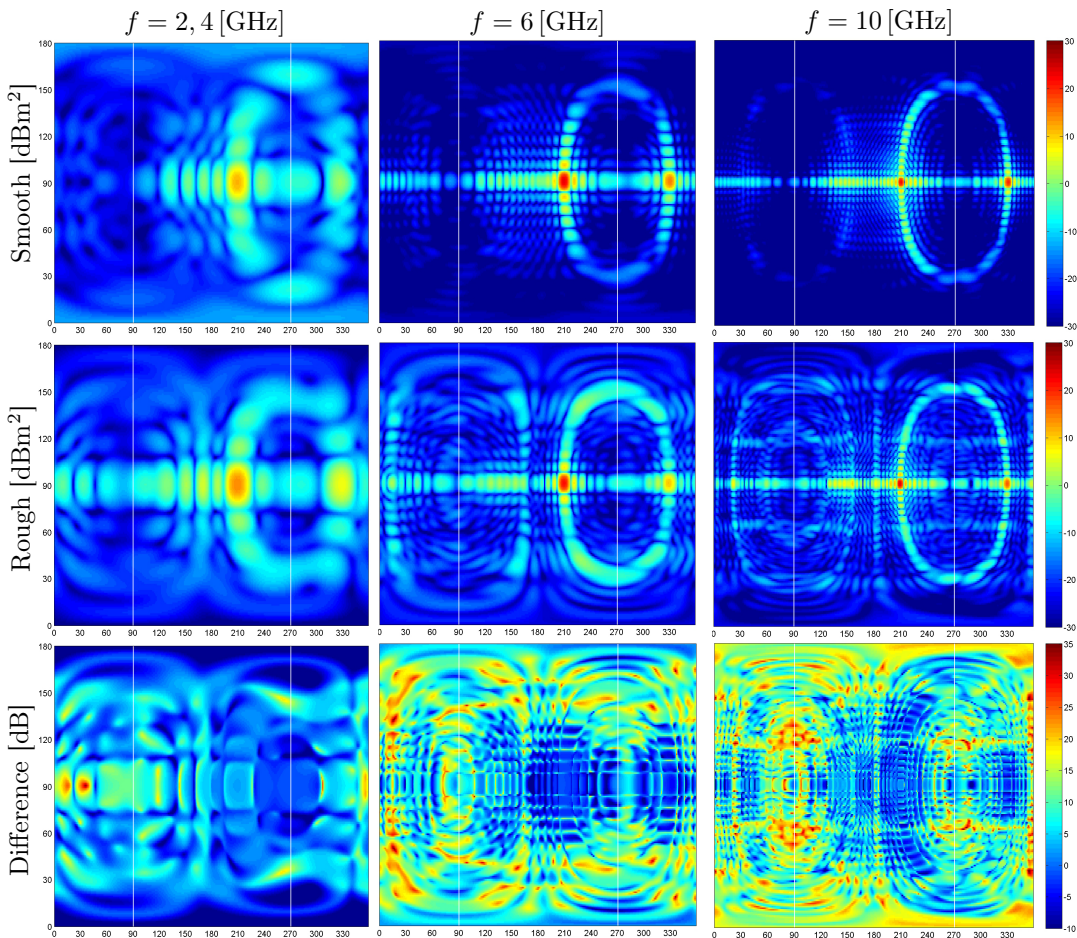
Figure 4.19: Volume irregularities RCSs analysis in case of reinforced concrete wall.

4.6 Contribution of roughness to the transmitted power

An interesting thing that can be analyzed by simulations and measurements is how surface roughness and/or volume irregularities influence the transmitted power or, in a wider perspective, the overall system power balance.

The parameters that we need to estimate are the S_{11} and the S_{21} that are the input port voltage reflection coefficient and the forward voltage gain of the equivalent two port network of the system represented in figures 4.20a–4.20b. In particular their modulus square power, $|S_{11}|^2$ and $|S_{21}|^2$, are nothing more than the power reflection coefficient

R defined in 1.1 and the power transmission coefficient T that differs from (1.8) and (eq:powTransmTM) because of the losses in the material (in fact (1.8) and (1.10) suppose $\sigma = 0$).

<table>
<tr><td>(a) Front view</td><td>(b) Rear view</td></tr>
</table>
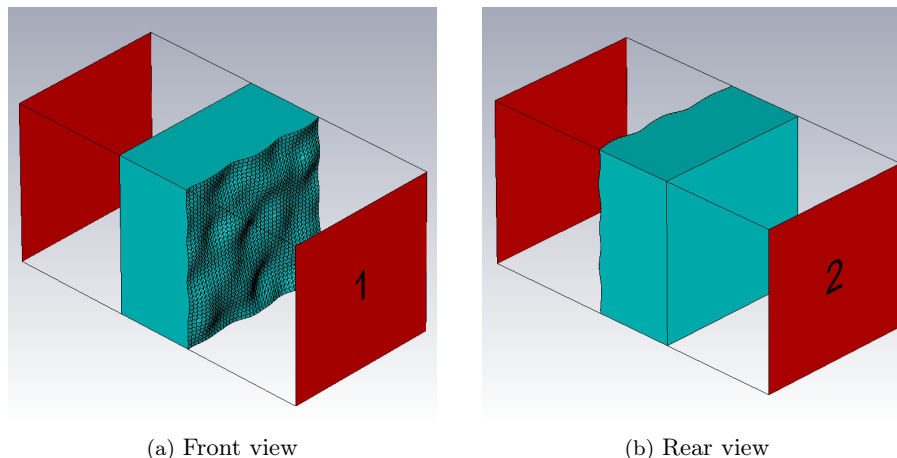
Figure 4.20: Setup for unit cell simulations; red squares are the system ports (Port 1 is where the incident plane wave is stimulated) and the wireframe delimits the periodically repeated unit cell.

Then one can obtain the part of incident power that is reflected and transmitted by the wall, moreover the fraction of dissipated power can be calculated. In fact, thanks to energy conservation, it is possible to extract the dissipated power P_{loss} that comprehend both *ohmic losses* in the material (if $\sigma \neq 0$) and, in case of rough surface, the *power that goes in in other polarizations*:

$$|S_{11}^p|^2 + |S_{21}^p|^2 + \frac{P_{loss}^p}{P_{inc}} = 1 \tag{4.19}$$

Where S-parameters are expressed as a linear quantity, *i.e.*, $S_{11} = 10^{(\frac{S_{11}\,[\text{dB}]}{20})}$ and p refers to the polarization of the incident plane wave (TE or TM).

Our final goal is to evaluate how roughness influences P_{loss}/P_{inc} for both polarizations, therefore, in order to evaluate the different power allocation in case of smooth and rough surfaces, simulations with *unit cell conditions* (*Floquet conditions*) in CST MWS can be done. Adopting this kind of boundary conditions we are able to change the incidence angle while contributions of wall sides are not considered, as it is supposed to have an infinitely extended surface. Small geometries could be also simulated without loss of generality, thanks to the fact that the slab under test is considered to be an infinite extension of the unit cell but, depending on the real geometry, this procedure has to be done with care and also in manner to maintain good surface statistical properties. Extending the defined unit cell to an infinite periodic structure forces also the field to be periodic with the same period; the concept is that Floquet conditions at unit cell ports relate this spatial periodicity with the electromagnetic field giving back the same result as in the infinite extension case. Moreover applying phase-shift terms to cell boundaries permits to change incidence directions.

In this way four different kinds of samples have been analyzed in the frequency range $[1 - 3]$ GHz: a sandstone slab with 3 [cm] thickness and a concrete wall with 10 [cm] thickness, both for two surface statistics (all parameters can be found in table 4.2).

Note that *the wavelength value refers to the highest frequency* (3 [GHz]) and electromagnetic parameters of the sandstone slab are the same as in 3.3 while for the concrete $\varepsilon_r = 5.5$ and $\sigma = 0.013$ [S/m].

Finally simulations with the unit cell boundary conditions have been done in order to reproduce the ideal condition of an infinite extension wall; as said before in this way S-parameters can be estimated, so it is possible to evaluate the power that flows through the sample in case of rough or smooth surface or even the effect of volume irregularities with respect to a homogeneous sample.

	Thickness	c_l	3σ	**Incidence angle φ_i**
Sandstone	3 cm	$\lambda/4$	$\lambda/8$	
			$\lambda/4$	0° and 30°
Concrete	10 cm	$\lambda/4$	$\lambda/8$	
			$\lambda/4$	

Table 4.2: Simulated samples with unit cell boundary conditions; mean thickness and RRS statistical parameters are reported.

All results in case of smooth and homogeneous slab can also be obtained from models with a good accuracy, in particular (3.2) can be modified for this purpose in order to consider different layers of mediums (*e.g. air-wall-air*), while only approximate and lacking solutions exist if rough surfaces are considered.

In figures 4.20a–4.20b a representation of the simulated unitary cell in the case of concrete, *port 1* is where we stimulate the incident plane wave for both TE and TM polarizations (input port). With reference to these figures it is possible to understand how S-parameters are calculated: at each port voltages and currents are monitored that are the input and output signals of the structure; the structure can be considered as an abstract system (see fig. 4.21) with input and output signals that are related by the calculated transfer function, defined as the quotient between the output signal spectrum and the input signal spectrum for each port modes combination.
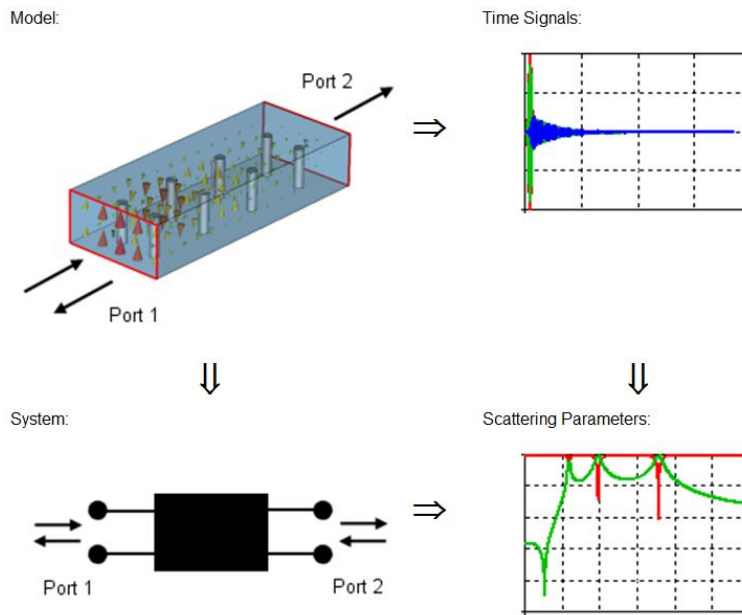
Figure 4.21: Relations among the model, the simulated system and their respective signals in time and frequency domain.

In our case of figures 4.20a–4.20b the stimulation is given at *port 1* as a plane wave realized with Floquet conditions, then S-parameters are estimated by the software, for both co- and cross-polarizations components, as the transfer functions of the equivalent two-port system; for example S_{11}^{TE} is the ratio between the spectra of the TE component of the output and input signals at *port 1*.

4.6.1 Sandstone

Simulation results are reported for each surface statistics and incidence angle. First reference simulations with a smooth slab are done obtaining S-parameters in ideal conditions and after simulations for rough surfaces are done. Superimposing these results for each TE or TM polarization one can observe the difference introduced by the RRS. In this case the material thickness is less than a wavelength for all frequencies of interest.

(a) TE

(b) TM
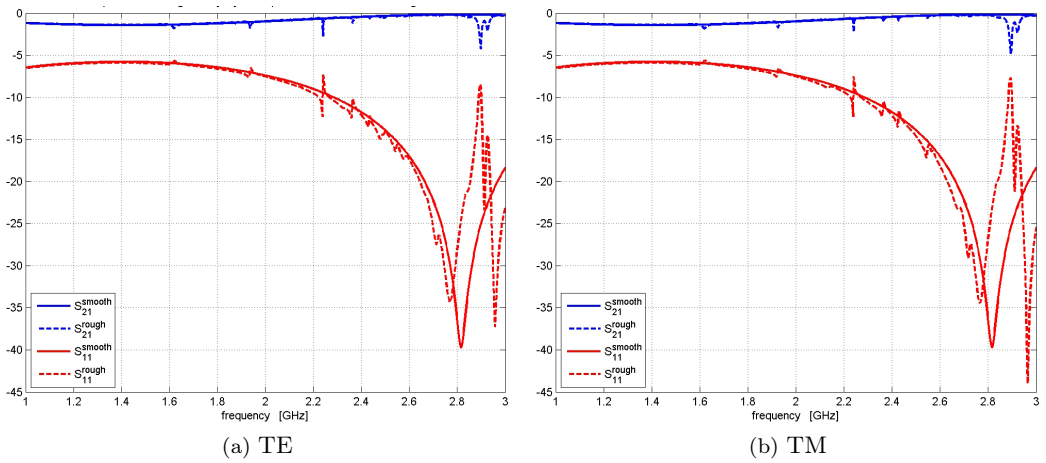
Figure 4.22: S_{11} (red) and S_{21} (blue) in [dB] in case of smooth (straight line) and rough (dotted line; $c_l = \lambda/4$, $3\sigma = \lambda/8$) surface for TE and TM polarizations and incidence angle $\varphi_i = 0$.

(a) TE

(b) TM
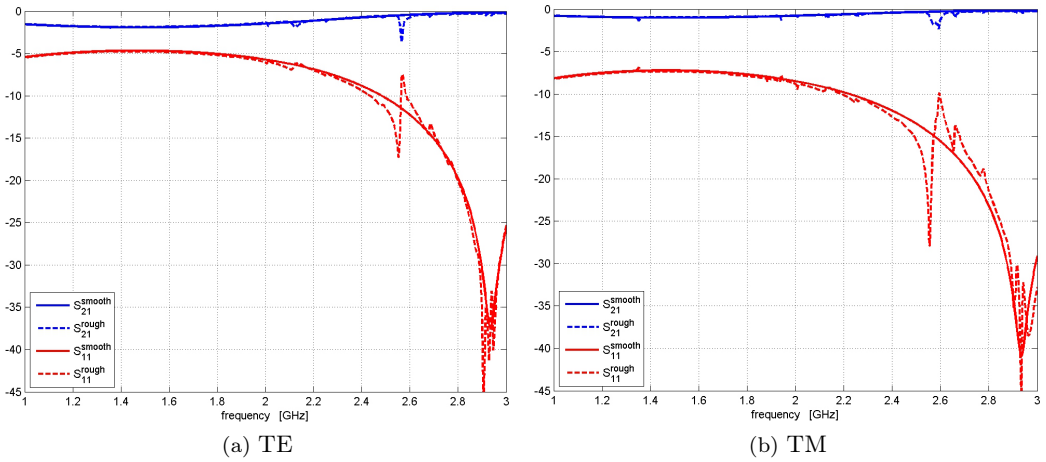
Figure 4.23: S_{11} (red) and S_{21} (blue) in [dB] in case of smooth (straight line) and rough (dotted line; $c_l = \lambda/4$, $3\sigma = \lambda/8$) surface for TE and TM polarizations and incidence angle $\varphi_i = \pi/6$.

(a) TE

(b) TM
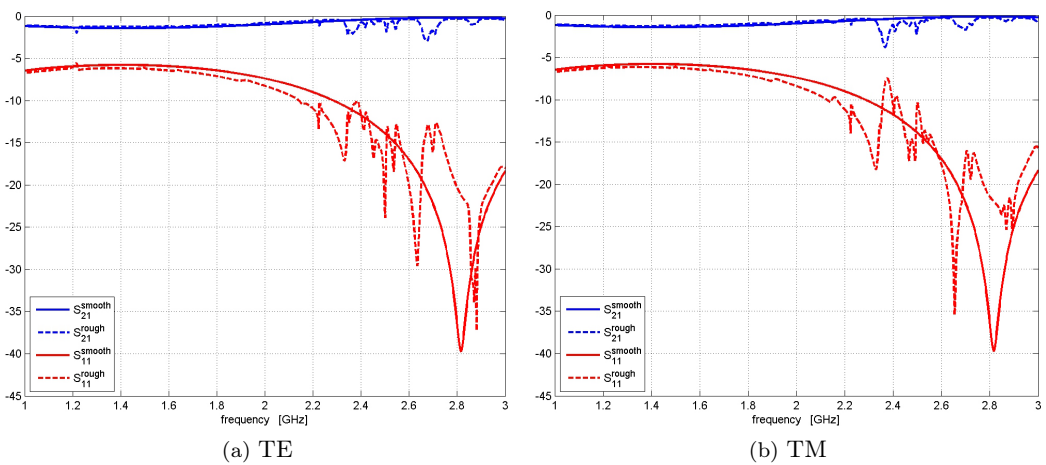
Figure 4.24: S_{11} (red) and S_{21} (blue) in [dB] in case of smooth (straight line) and rough (dotted line; $c_l = \lambda/4$, $3\sigma = \lambda/4$) surface for TE and TM polarizations and incidence angle $\varphi_i = \pi/6$.
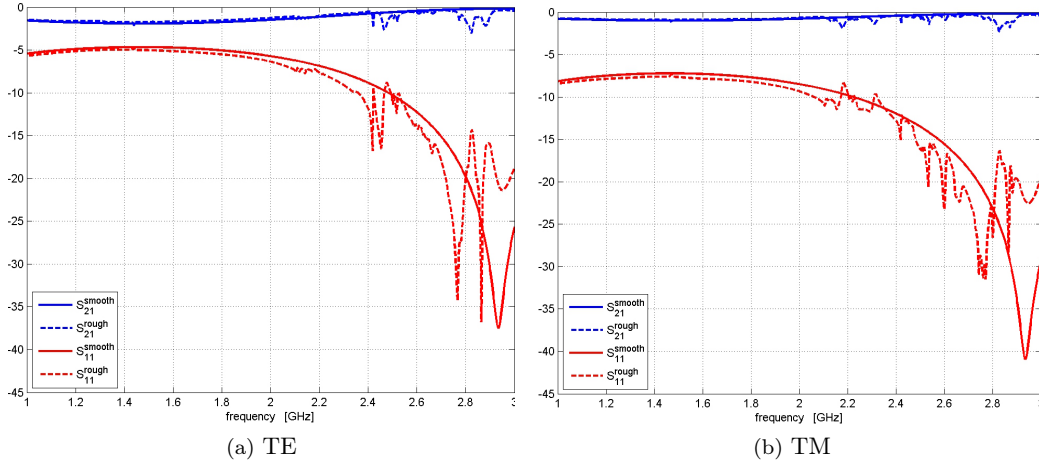
Figure 4.25: S_{11} (red) and S_{21} (blue) in [dB] in case of smooth (straight line) and rough (dotted line; $c_l = \lambda/4$, $3\sigma = \lambda/4$) surface for TE and TM polarizations and incidence angle $\varphi_i = \pi/6$.

These results show that at low frequencies there isn't a big difference between S-parameters in case of a smooth or a rough surface as it is at higher frequencies; this can be due to the fact that RRSs statistics are tuned according to the lowest wavelength, so that at lower frequency the surface is seen almost as smooth.

Another interesting effect is the change of behavior of the two TE and TM polarizations for the incidence angle $\varphi_i = 0$: in fact when we consider a smooth homogeneous slab these two components equals each other (in agreement with (3.2)) while in case of rough surface depolarization happens so they are slightly different. Moreover it is notable that the increase of standard deviation of heights from $\lambda/(3\cdot 8)$ to $\lambda/(3\cdot 4)$ results in a higher attenuation of the transmitted component, *i.e.*, $|S_{21}|^2$ tends to be lower with higher degree of roughness in the considered frequency band.

4.6.2 Concrete

The same set of simulations has been done for a concrete wall of 10 [cm] thickness, which is comparable with the wavelengths of simulated frequencies.

As one can see in the following figures the roughness effect is now more clear and evident: the transmitted power is reduced on average, but the difference is in the order of maximum $1\,[\mathrm{dB}] - 3\,[\mathrm{dB}]$. The interesting effect is that at certain frequencies even the reflected component is lower than in the smooth case, this means, according to (4.19), that roughness modifies the overall power balance.

Moreover simply inverting (4.19) it is straightforward to obtain the amount of incident power dissipated into the media and transferred in other polarizations because of the rough surface P_{loss}/P_{inc} (figg. 4.30a–4.31b).

First of all it is interesting to observe that the higher the frequency the higher the losses, independently from the polarization or incidence angle. In addition, comparing red and blue dotted lines in figures 4.30a–4.30b and figures 4.31a–4.31b, it is possible to see that the increase of standard deviation of heights rises the lost power.

Therefore from these results we can say that surface irregularities influences the overall power balance of the system, in general losses tend to rise with higher degree of roughness and this can be translated in more dissipations in the material and transfers of power into cross polarized components.

(a) TE

(b) TM
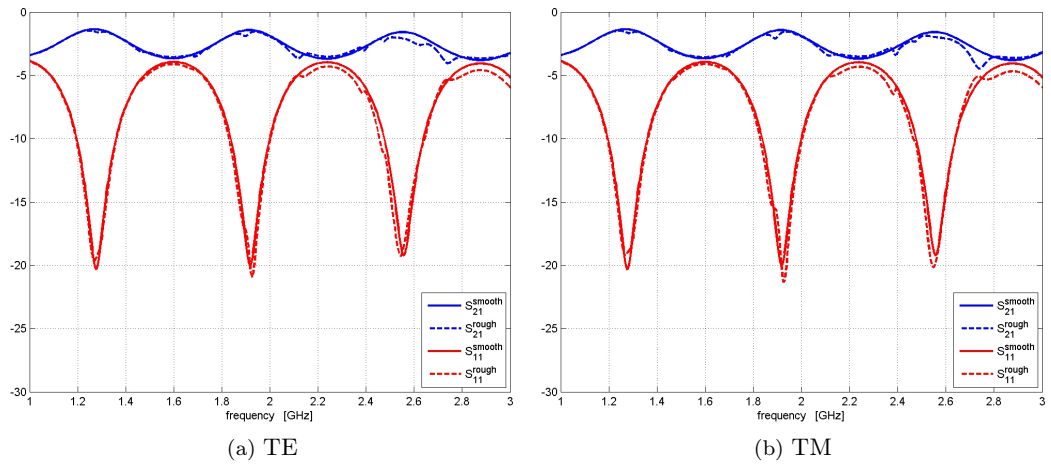
Figure 4.26: S_{11} (red) and S_{21} (blue) in [dB] in case of smooth (straight line) and rough (dotted line; $c_l = \lambda/8$, $3\sigma = \lambda/4$) surface for TE and TM polarizations and incidence angle $\varphi_i = 0$.

(a) TE

(b) TM
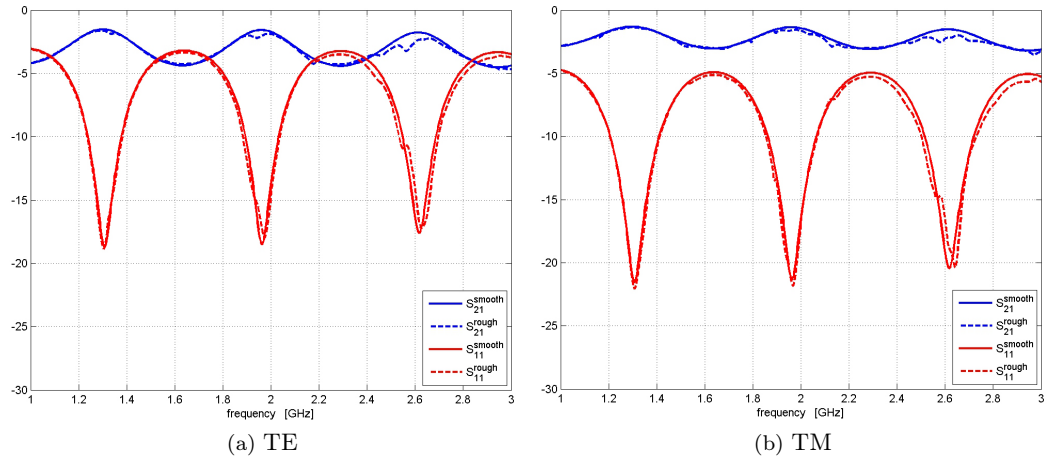
Figure 4.27: S_{11} (red) and S_{21} (blue) in [dB] in case of smooth (straight line) and rough (dotted line; $c_l = \lambda/8$, $3\sigma = \lambda/4$) surface for TE and TM polarizations and incidence angle $\varphi_i = \pi/6$.

(a) TE

(b) TM
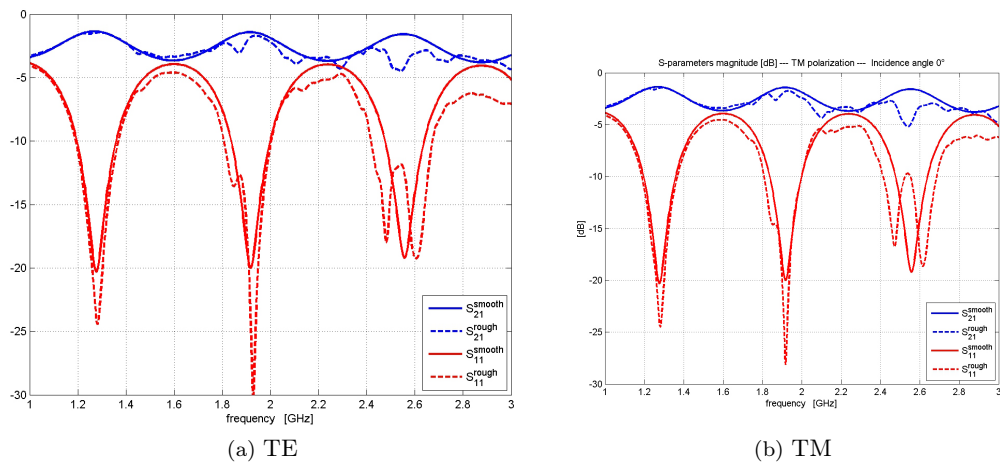
Figure 4.28: S_{11} (red) and S_{21} (blue) in [dB] in case of smooth (straight line) and rough (dotted line; $c_l = \lambda/4$, $3\sigma = \lambda/4$) surface for TE and TM polarizations and incidence angle $\varphi_i = 0$.

(a) TE

(b) TM
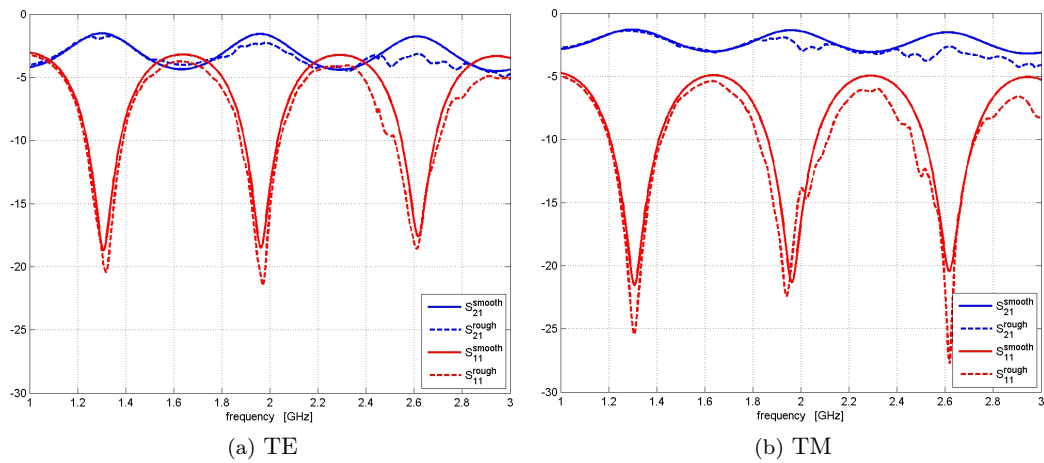
Figure 4.29: S_{11} (red) and S_{21} (blue) in [dB] in case of smooth (straight line) and rough (dotted line; $c_l = \lambda/4$, $3\sigma = \lambda/4$) surface for TE and TM polarizations and incidence angle $\varphi_i = \pi/6$.

(a) $\varphi_i = 0$

(b) $\varphi_i = \pi/6$
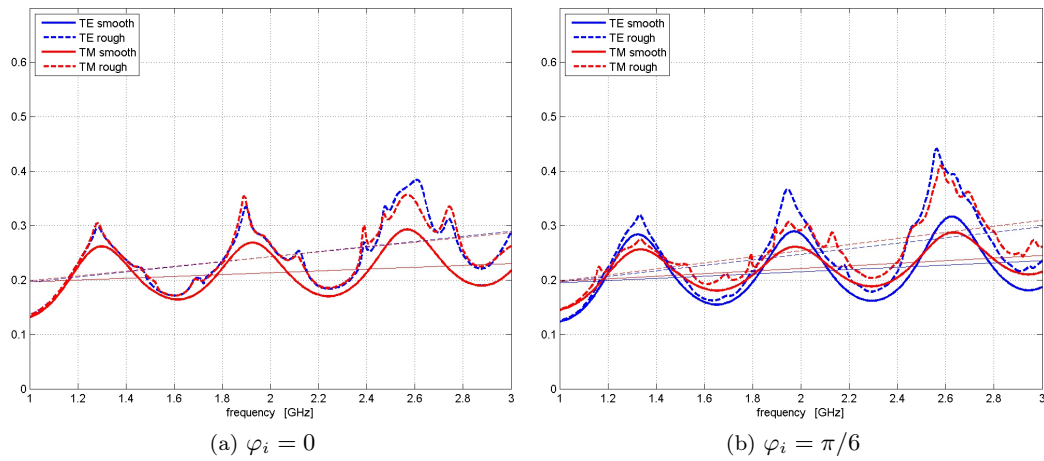
Figure 4.30: P_{loss}/P_{inc} in case of smooth (straight) and rough (dotted line; $c_l = \lambda/4$, $3\sigma = \lambda/8$) surface.

(a) $\varphi_i = 0$

(b) $\varphi_i = \pi/6$
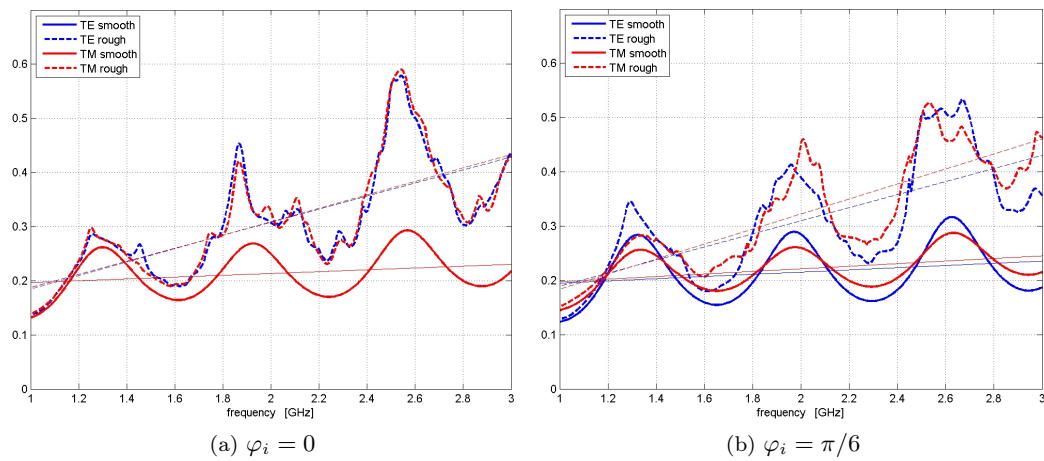
Figure 4.31: P_{loss}/P_{inc} in case of smooth (straight) and rough (dotted line; $c_l = \lambda/4$, $3\sigma = \lambda/4$) surface.

Characterization of electromagnetic scattering

A possible way to analyze the scattering phenomenon is to measure the received signal at an antenna for several positions around the object of the transmitting antenna (see fig. 5.1).

As previously seen reflection and transmission coefficients are functions of the incident angle φ_i and, as a consequence, the same is for the field spatial distribution. Moreover one has to remember that this dependence holds also for the effective degree of roughness (see 1.3). Therefore to give an estimation of both back and forward scattering is necessary to measure, for each incident angle, the scattered signal in the whole angular domain Then
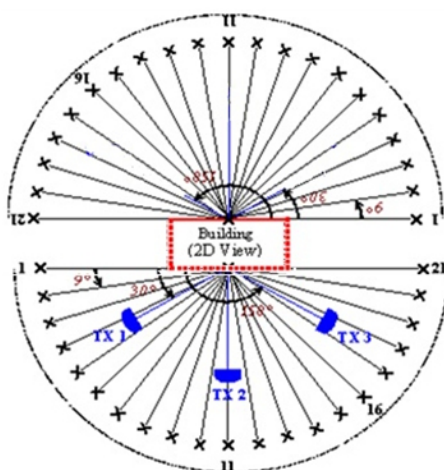
Figure 5.1: Diffuse scattering measurement setup.

the adopted solution has been developed in one of CEA-Leti Grenoble anechoic chamber in order to satisfy the before-mentioned constraints and offer the best flexibility during the measurements: a rotating positioning system, where the wall under test is positioned, is placed between transmitting and receiving antennas; one of these antennas has a fixed position, while the other has the possibility to rotate both jointly or dis-jointly with the sample, that can only rotate on itself.

Once measurements from this setup are available, the scattering pattern could be determined in two different ways:

1. Comparing the measurements of two different slabs of the same material, one with a smooth surface and the other with a rough surface.

2. Implementing a scattering model in a ray tracing program and tune it with respect to the measurements, after that the best fitting parameters of the model are assumed to describe the wave-sample interaction.

The former option is explicitly analysis-oriented, in fact the differences in the two cases are mainly due to surface roughness and this permits to evaluate only its contribution. On

the other hand the latter method permits to understand if a certain model can be suitable for scattering characterization, so it is a way to verify something previously supposed.

5.1 Experimental setup

A positioning system has been *ad-hoc* designed in order to do a complete characterization of the sample following the previously descripted measurement setup. The available rotation stage, in which the positioning system is placed, is the *Newport RV120PP* (fig. 5.2). Its characteristics can be found in [18] and, in particular, maximum operating loads are given in figure 5.3.
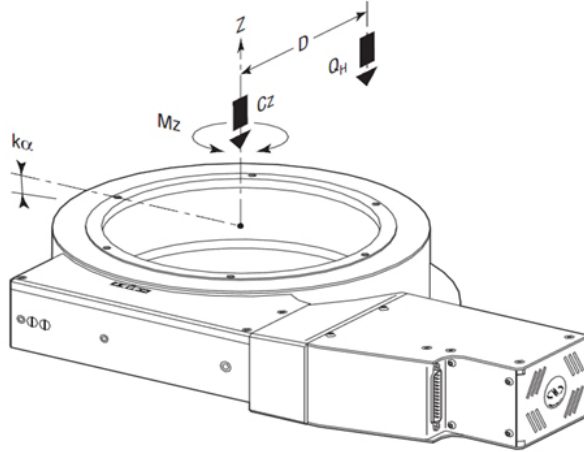
Figure 5.2: The Newport RV series rotation stage.

	RV120
Cz, Normal centered load capacity (N)	1800
a, construction parameter (mm)	40
b$^{(1)}$, (mm) except HAT & HAHLT	53
for HAT & HAHLT	71
kα, radial compliance (μrad/Nm)	1.5
Q$_H$, Off-center load, vertical rotation axis	Q$_H$ ≤ Cz / (1+D/a)
Q$_V$, Off-center load, horizontal rotation axis	Q$_V$ ≤ Cz / 2 / (1+D/a)

Figure 5.3: Newport RV120PP load specifications.

5.1.1 Load dimensioning

First a load dimensioning has been done. The weight of the antenna and its support is supposed to be around $6\,[\text{kg}] = 58.8\,[\text{N}] = Q_{\text{H}}^{ant}$, and its maximum distance from the rotation axis of the *RV120PP* is $d_{max} = 1\,[\text{m}]$. As one can see from figure 5.3 the maximum centered load supported by the stage is $C_z = 1800\,[\text{N}] \cong 184\,[\text{kg}]$ while considering an off-center load one has to satisfy one of the two last inequalities depending on the axis orientation. In our case the rotation axis is vertical, normal to the floor, so the *maximum off-center load is given by* (cf. [18]):

$$Q_{\text{H}}^{max} = \frac{1800\,[\text{N}]}{1 + \frac{1000\,[\text{mm}]}{40}} = 69.2\,[\text{N}] \cong 7.1\,[\text{kg}] \tag{5.1}$$

Considering the real weight of the antenna and its support we are able to estimate the *remaining off-center capability* of the rotation stage:

$$Q_{\text{H}}^{max} - Q_{\text{H}}^{ant} = 69.2\,[\text{N}] - 58.8\,[\text{N}] = 10.4\,[\text{N}] \cong 1.1\,[\text{kg}] \tag{5.2}$$

Inverting the second-last equation in figure 5.3 we obtain that the *centered load capability still available* is:

$$C_z = \left(1 + \frac{1000\,[\text{mm}]}{40}\right) \cdot 10.4\,[\text{N}] = 271.2\,[\text{N}] \cong 27.7\,[\text{kg}] \qquad (5.3)$$

Finally, just from system dimensioning in terms of loads, the maximum weight of the sample plus the support structure should be around 28 [kg] when the antenna is positioned at 1 [m] from it.

With the same procedure it is possible to obtain the maximum values of C_z for a fixed antenna (plus support) weight in function of the distance from the rotation axis. These results are reported in Table 5 for $Q_\text{H}^{ant} = 6$ [kg].

d_{max} [mm]	Q_H^{max} [N]	C_z [N]	C_z [kg]
100	514.29	1594.20	162.67
200	300.00	1447.20	147.67
300	211.76	1300.20	132.67
400	163.64	1153.20	117.67
500	133.33	1006.20	102.67
600	112.50	859.20	87.67
700	97.30	712.20	72.67
800	85.71	565.20	57.67
900	76.60	418.20	42.67
1000	69.23	271.20	27.67

Table 5.1: Maximum values of C_z in function of d_{max}.

The table above is quite useful because, with the designed setup, the distance between the antenna and the sample can be varied according the needs.

5.1.2 Inertia

Another parameter to take into account is the *maximum inertia* that the positioner can handle; this value represents the maximum kinetic energy that the rotation stage can absorb in the event of a sudden halt at the maximum speed or, equally, the kinetic energy that the stage can sustain when accelerating from stop to the maximum speed in 250 [ms] (cf. [18]). The moment of inertia with respect to the z axis is given by:

$$I_z = M \cdot d^2 \qquad (5.4)$$

Where M is the mass and d is the distance of the mass from the rotation axis; note that the total inertia of a certain system is obtained by the superposition of the various happening effects, *i.e.*, we have to sum up all inertia contributions. The values of inertia I_z^{ant}, due to the antenna and its support, are reported in table 5.2. These results have been obtained fixing $M_{ant} = 6, [\text{kg}]$ (previously we called this parameter Q_H^{ant}) and applying (5.4) in function of the distance from the rotation axis. Furthermore we have also a contribution to inertia from the sample I_z^{sample} that mainly depends on its shape and weight (M_{sample}). For a parallelepiped structure the inertia can be evaluated with (5.5):

$$I_z^{sample} = \frac{1}{12} M \cdot (x^2 + y^2) \qquad (5.5)$$

Where x and y are the dimensions of the sample defined with respect to the z rotation axis applying the right-hand rule. As said before $I_z^{tot} = \sum_i I_z^i$, where different i represents different contributions to inertia (sample, antenna, *etc.*).

The maximum inertia sustainable by the *RV120PP* positioner is $I_z^{max} = 1\,[\text{kg m}^2]$, so this limit is exceeded most of times. Anyway, as reported in [18], this issue can be neglected if the stage is used at low speeds or, better, at speeds for which an accidental stop wouldn't produce inertia higher than the maximum allowed. For example if $I_z^{tot}/I_z^{max} = 3$ the highest angular speed that one should use is equal to $\omega_{max}/3$.

d_{max} [mm]	I_z^{ant} [kg·m²]	I_z^{sample} [kg·m²]	I_z^{tot} [kg·m²]
100	0.06	2.17	2.23
200	0.24	2.17	2.41
300	0.54	2.17	2.71
400	0.96	2.17	3.13
500	1.50	2.17	3.67
600	2.16	2.17	4.33
700	2.94	2.17	5.11
800	3.84	2.17	6.01
900	4.86	2.17	7.03
1000	6.00	2.17	8.17

Table 5.2: Values of inertia for $M_{ant} = 6$ [kg], $M_{sample} = 40$ [kg], $x = 0.8$ [m] and $y = 0.1$ [m].

5.1.3 Torque

Finally we must consider the torque developed by the positioner. From [18] we have that the maximum allowed torque is $T_{max} = 15$ [N/m] for all speeds; in table 5.3 are reported the maximum weights M_{ant}^{max} of the antenna and its support, as a function of d, that permit to remain within this limit.

d_{max} [mm]	M_{ant}^{max} [kg]	d_{max} [mm]	M_{ant}^{max} [kg]
100	0.06	600	2.23
200	0.24	700	2.41
300	0.54	800	2.71
400	0.96	900	3.13
500	1.50	1000	3.67

Table 5.3: M_{ant}^{max} to respect the torque constraint.

As previously said the weight of the antenna and its support M_{ant} is about 6 [kg] thus, for a certain distance from the axis, when this value exceeds the values reported in the aforementioned table the rotation stage can be used only in the horizontal position, where the rotation axis is normal to the ground (cf. [18]).

5.1.4 Positioning system

According to what said at the beginning of this chapter a positioning system for scattering measurements in anechoic chamber has been made. First an accurate evaluation of needs and constraints has been done, in fact dimensions and weights of this structure had to satisfy rotation stage requirements and positioning alignments. As an existing structure was already available we tried to design the new system in manner to reuse some of its parts, but others options have also been analyzed. Therefore during the design phase several interviews have been done with external suppliers, so to have further verifications of our design and also to adapt it to realization constraints. The most important characteristics that our system had to offer were:

1. Full 360° rotation of the antenna round the sample (as the other antenna position is fixed)

2. Possibility to rotate the antenna both jointly and disjointly with the sample

3. Material under test holder (sample dimensions up to 1m × 1m × 0.2m)

4. Mechanical strength for weights up to 40 [kg]

As a result the system that best fitted our needs is reported in figure 5.4. The sample of the material under test is placed over the principal support on the left and is fixed on the holder in figure 5.5 by four clamps that are screwed on it. This system allows to secure several kinds of samples, in fact the clamps in the holding system can be adjusted according to material dimensions. This part rotates jointly with the rotating system previously seen, the *Newport RV120PP*.

The antenna is placed over an arm that has the possibility to rotate all around the sample and in the meanwhile it can be also fixed jointly with it each 10°; in this manner one has the possibility to maintain constant the angle between the antenna and the specimen while varying the angle with respect to the other antenna (see fig. 5.1). Thanks to this system we are able to reproduce bi-static measurements on a plane. Another parameter that can be changed is the distance between the antenna and the material under test, in fact in the arm are present two grooves permitting the antenna to move back and forward on it.
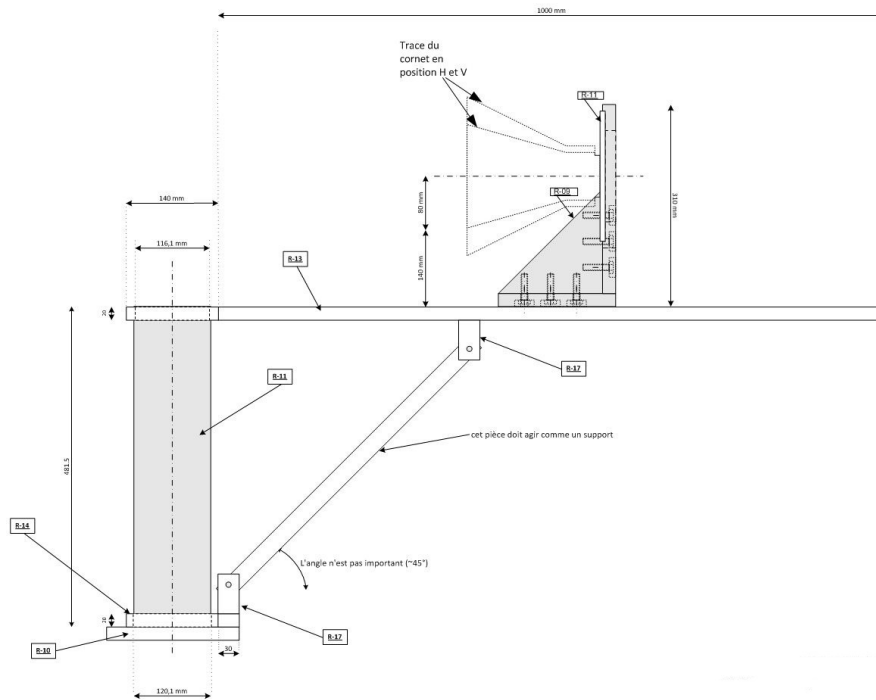
Figure 5.4: Upper part of the realized positioning system for scattering measurements, side view.
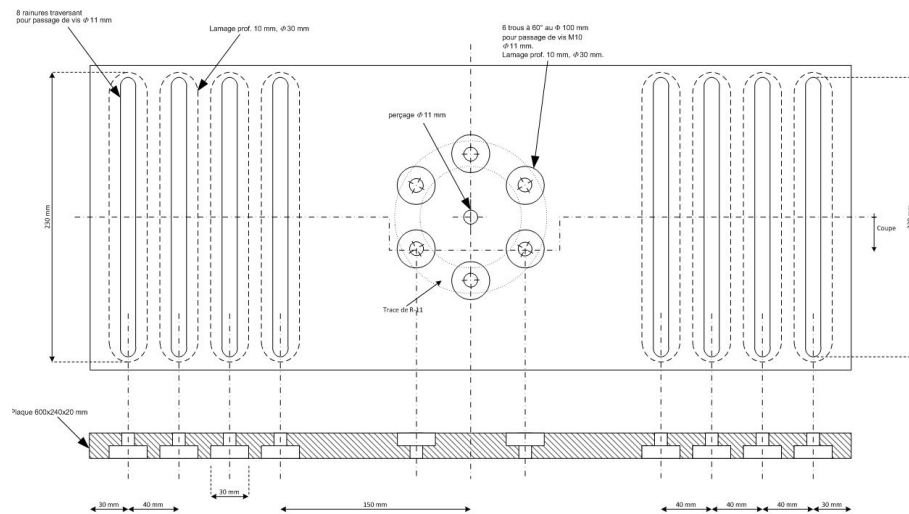
Figure 5.5: Sample holder, top view.

5.2   Farfield condition

In measurements we used a rectangular horn antenna *EMCO 3115* with a diagonal aperture of 27.5 [cm]. As well-known the far field condition is expressed by:

$$d = \frac{2D^2}{\lambda} \tag{5.6}$$

Where D is the maximum dimension of the antenna and d is the distance after which we are in the farfield region. The positioning system that we have seen in 5.1.4 offers the possibility to vary the distance between the antenna and the sample within a maximum distance of 0.85 [m] (because of dimensions constraints of the anechoic chamber); since we do measurements in the $[2-10]$ GHz band (5.6) is not always satisfied.

Frequency [GHz]	2	4	6	8	10
d [m]	1.01	2.02	3.03	4.03	5.04

Table 5.4: Farfield distance in function of frequency for the *EMCO 3115* horn antenna.

Simulations with CST MWS have been done with a simplified model of the horn antenna used in measurements (see fig. 5.6) in order to evaluate the phase difference between the center and the side of the sample.
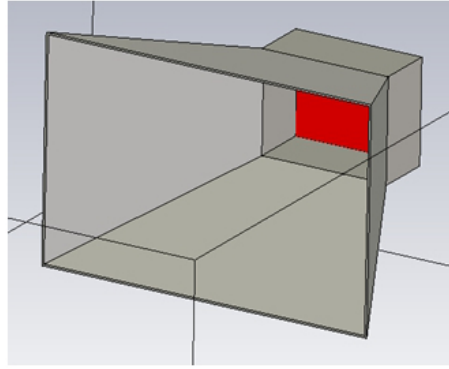
Figure 5.6: Simulated horn antenna design.

(a) 2 [GHz]	(b) 4 [GHz]	(c) 6 [GHz]
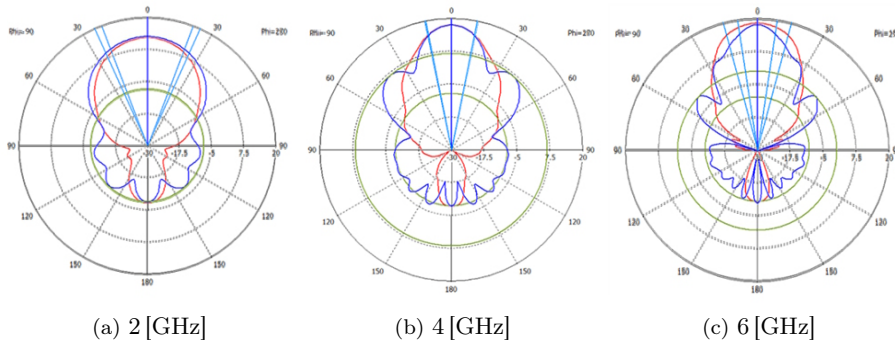
Figure 5.7: Patterns for vertical-TE (blue) and horizontal-TM (red) polarizations.

The sample is a concrete slab ($\varepsilon_r = 5.5$, $\tan\delta = 0.03$) which dimensions are 0.90m $\times$ 0.60m $\times$ 0.03m distant 0.80 [m] from the horn. The phase results are given in figure 5.8 as a function of frequency for a normal incidence angle. As we can see in figure 5.8 the phase differs between the center and the border, than confirming that the impinging wave is not plane as wanted, the phase representation of the system composed by the horn antenna and the wall is shown in figure 5.9 for a frequency of 6 [GHz].
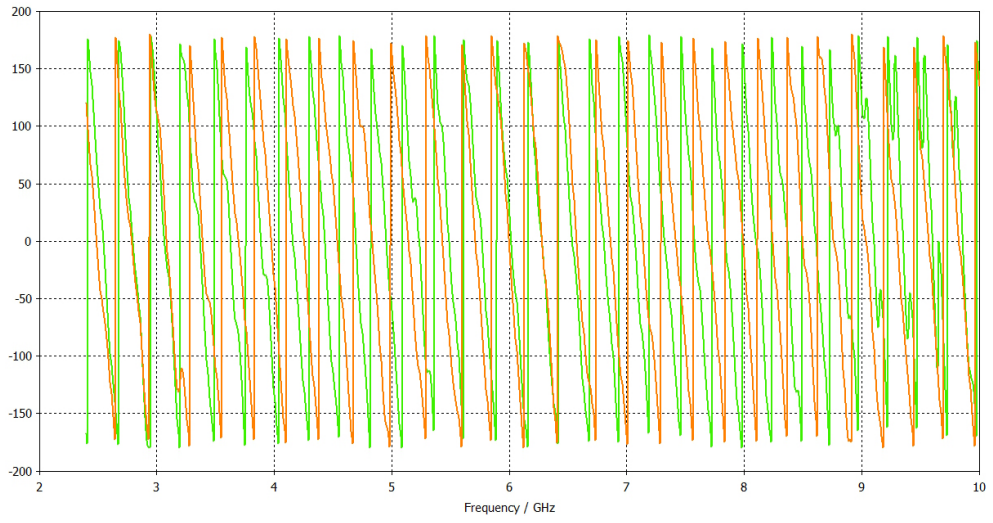
Figure 5.8: Phase in degree of the impinging wave in the center (orange) and in the outer border (green) as a function of frequency.
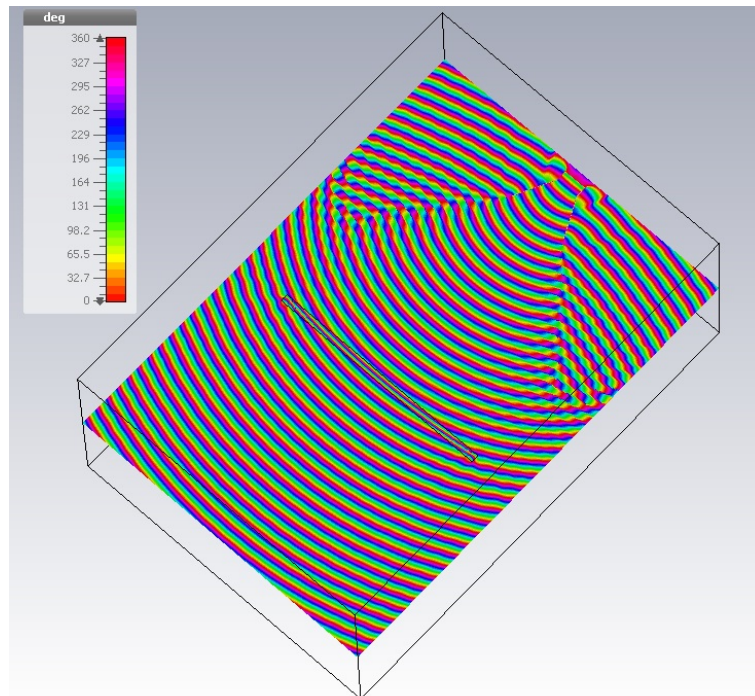
Figure 5.9: Phase representation at 6 [GHz]; the antenna doesn't illuminate the sample with a plane wave.

5.3 Reference system

Measurements have been conducted with the reference system shown in figure 5.10. It differs from the one adopted in simulations (fig. 4.9), in fact we have to remember that (1.1) and (1.2) still hold but in our case two different angles are varied, the *incidence angle* and the *receiving angle*, so it is better to show the measurement reference system in manner to have the key to post-process our results.

For a fixed incident angle φ_i, the system composed by the sample and the TX antenna are rotated jointly from 0° to 360° with 2° step; this angle will be denoted by φ_{sample}.
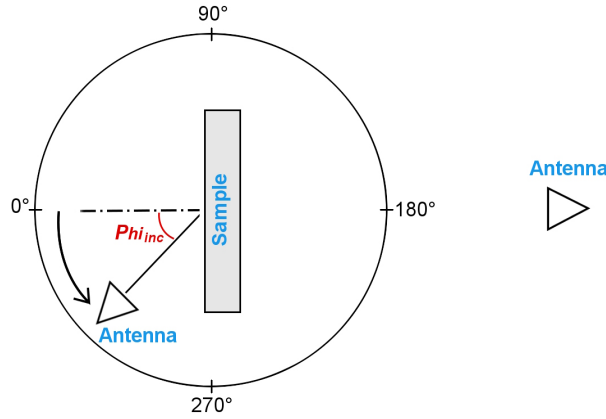
Figure 5.10: Measurement setup scheme for $\varphi_i = 0°$ and $\varphi_{sample} = 0°$.

For example is shown in figure 5.11 the measurement setup for $\varphi_i = 0°$ and $\varphi_{sample} = 90°$. According to what said before we have that the specular reflection (with respect to the
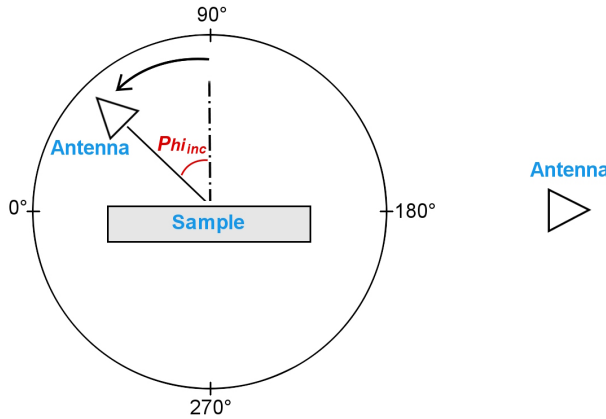
Figure 5.11: Measurement setup scheme for $\varphi_i = 0°$ and $\varphi_{sample} = 90°$.

incidence angle φ_i) happens when the receiving and transmitting antennas satisfy (1.1), thus when:

$$\varphi_{sample}^{refl} = \varphi_i + 180°$$

(5.7)

Considering the transmitted field (1.2) still holds but, due to the small thickness of the sample, it is reasonable to assume that the transmission direction is the same of the line of sight (LOS) case. Therefore the transmission direction is when φ_{sample} satisfies:

$$\varphi_{sample}^{trans} = -\varphi_i$$

(5.8)

As said before this is useful to comprehend how to manage measurement results (vector indexes, angles, *etc.*) for the post processing.

Anyway it could be better to have the possibility to analyze measurement results with the same reference system as in simulations, thus to have the x axis normal to the surface and angles that follows (1.1) and (1.2) without any correction. Therefore a change of reference system in has been done in data post-processing (fig. 5.12).
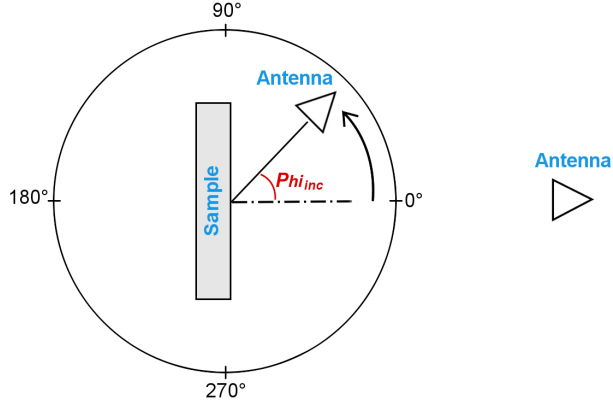
Figure 5.12: Final measurement analysis reference system (same as in 4.4).

Now it comes natural to understand results shown in the next section thanks to the facts that $\varphi^{refl} = -\varphi^{inc}$ and $\varphi^{trans} = \varphi^{inc} + 180°$, where the same assumption as in (5.8) has been done.

5.4   Measurement results

Using the experimental setup seen in 5.1.4 and 5.3 a measurements campaign has been conducted for different incidence angles and with different samples. The idea is to retrieve a sort of transfer function of the building material under test and also evaluate the difference between the rough and smooth samples. For each incidence angle a reference measurement is first done without the sample in order to characterize the overall effect of the antenna and the support. The second step is to repeat the same kind of measurements with the desired sample, in our case we measured two different kinds of sandstones: a smoothened one and a rough one with same dimensions of 0.9m × 0.6m × 0.03m (more precisely the thickness is 0.033 [m] for the smooth and 0.035 [m] for the rough).

Finally the post-processing leads to a sort of *sample transfer function* $\xi(f, \varphi_i, \varphi_{sample})$ of the material under test in the analyzed plane, that is the squared ratio between the $H(f)$ when the sample is present and the $H(f)$ of reference case:

$$\xi(f, \varphi_i, \varphi_{sample}) = 20 \log \left| \frac{H_{sample}(f, \varphi_i, \varphi_{sample})}{H_{calibration}(f, \varphi_i, \varphi_{sample})} \right| \tag{5.9}$$

The same operation can be done with two different measurements of the same slab in case of rough or smooth surface, in this way only the scattering contribution should be present (in a similar way as we did in simulations).

Measurements have been done for incidence angles φ_i of 20°, 30° and 40°, while φ_{sample} varied from 0° to 360° with 2° angular step (181 points); for each configuration a wideband frequency measurement of $H(f)$ has been conducted from 2 [GHz] to 10 [GHz] with 10 [MHz] step (801 points). The polarization of the impinging wave has always been vertical (TE) and antennas were in co-polarization.
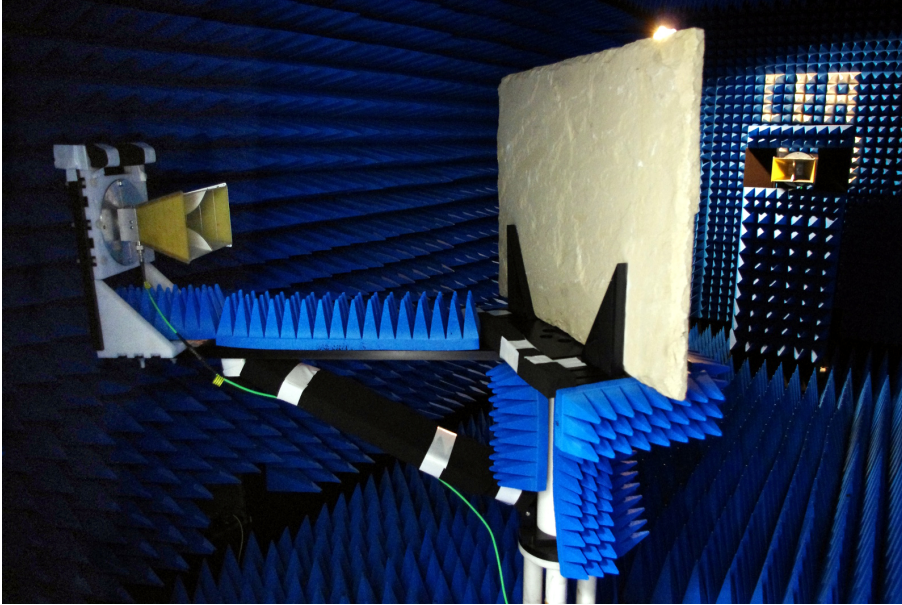
Figure 5.13: Analyzed rough sandstone slab mounted on its holder.

5.4.1 Calibration meausurement

The first step is to do a calibration measurement of the system without any sample, in this manner we characterize the transfer function of the antenna and its support, that is a modified antenna radiation pattern as represented in figure 5.14 for an incidence angle of $\varphi_i = 30° = \pi/6$ and frequency $f = 10\,[\text{GHz}]$.
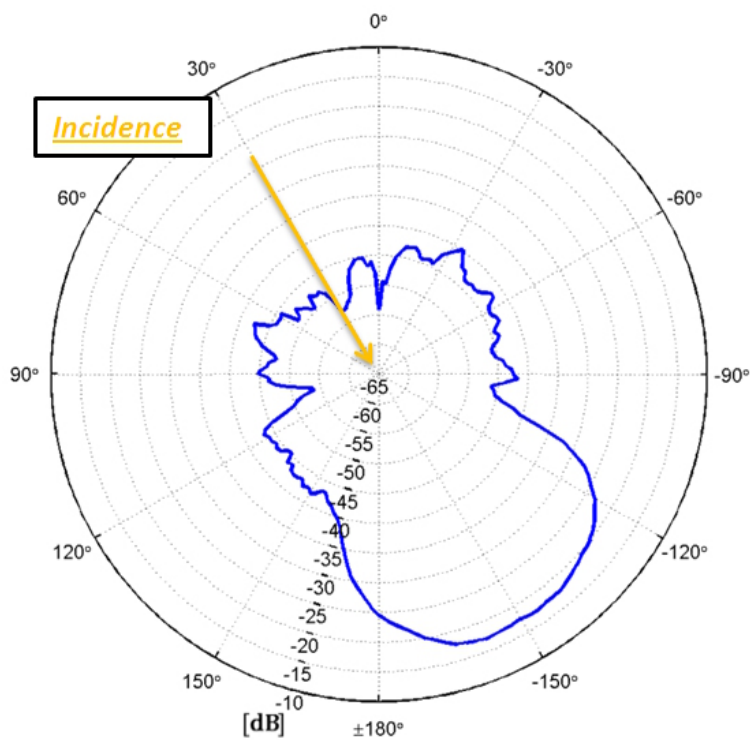
Figure 5.14: Calibration measurement for $\varphi_i = 30°$ at $f = 10\,[\text{GHz}]$.

5.4.2 Measurement with sample

Subsequently measurements with samples, both smooth and rough, have been done (note that the smooth slab isn't perfectly polished, a little level of roughness is present, but it is very low even if compared to the highest frequency).
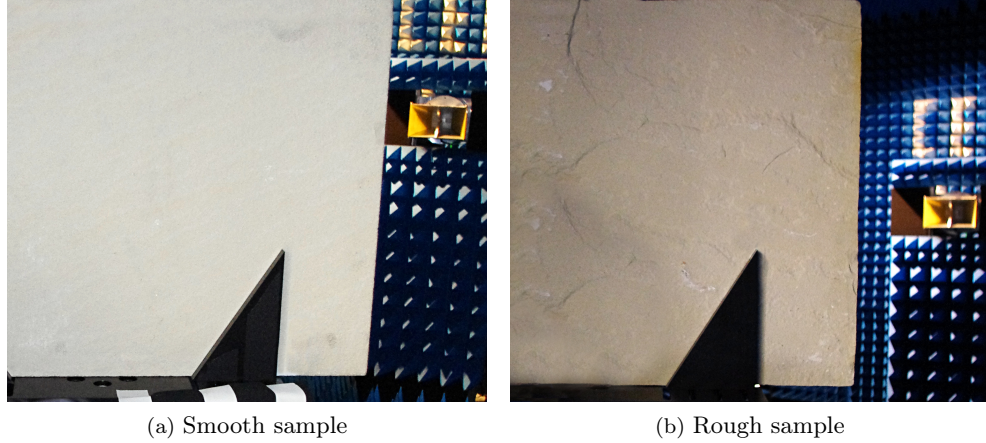
(a) Smooth sample   (b) Rough sample

Figure 5.15: Detail of smooth and rough samples.

In figures 5.16a–5.16b are reported the polar graphs for smooth and rough sandstone slabs respectively. As one can see the introduction of the slab results in an attenuation along transmission direction with reference to the calibration measurement and evidently the reflection lobe in the backward half-space appears. This lobe is the sum of both coherent and incoherent contributions, but thanks to the fact that the level of roughness of the smooth slab is negligible we can say that in this case it is almost due to the coherent component summed with the diffracted field from slab sides.
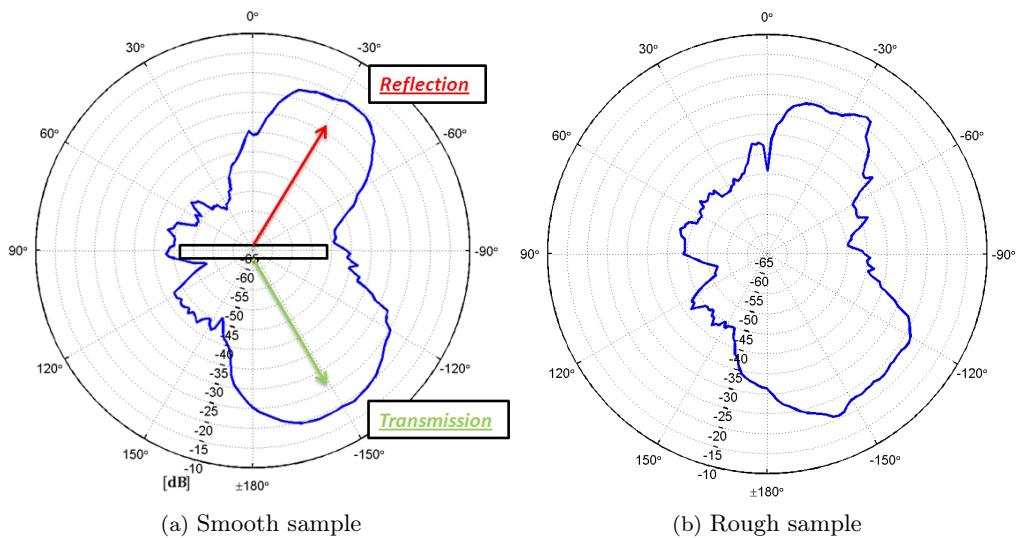
(a) Smooth sample   (b) Rough sample

Figure 5.16: Measurement with smooth and rough samples for $\varphi_i = 30°$ at $f = 10\,[\text{GHz}]$.

5.4.3 Sample transfer function

Processing our measurements as described in (5.9) permits to obtain only the contribution of the material, thus the effect that the introduction of the slab has on the system.
From figures 5.17a–5.17b it is clear that the field spatial distribution is spread over a wider

(a) Smooth sample
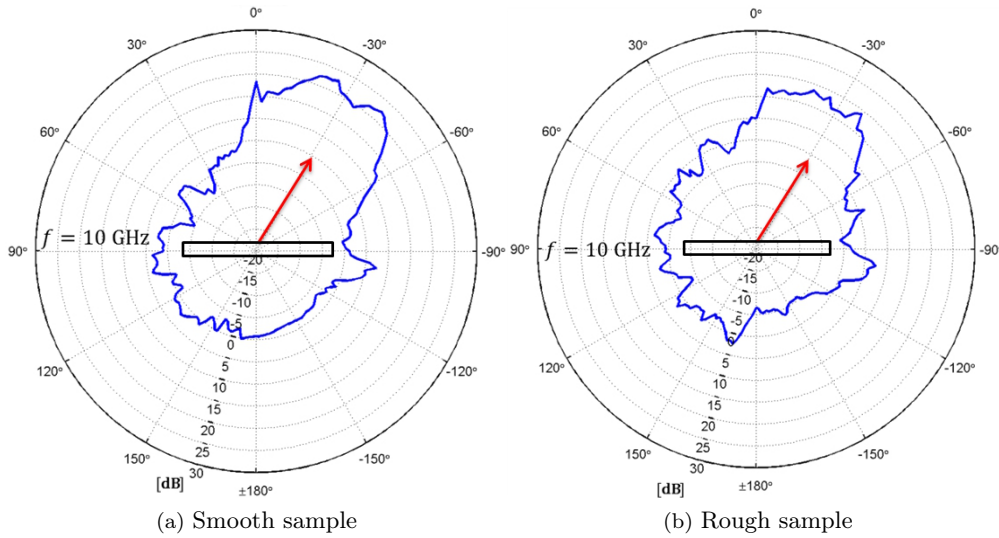
(b) Rough sample

Figure 5.17: Measurement with smooth and rough samples for $\varphi_i = 30°$ at $f = 10\,[\text{GHz}]$.

angular range in the case of rough surface at the expenses of the specular reflected component that is attenuated if compared to the smooth slab. These measurements show an higher reflected component around incidence direction, that is something like the *backlobe* in figure 2.11. Even diffracted components seem to be different, but it is hard to separate each contribution from the other and then any supposition could be wrong.

Moreover it is possible to observe an higher attenuation in transmission when the rough sample is considered, this accordingly to simulations in 4.

5.4.4 Power beamwidth

Starting from polar plots in figures 5.17a–5.17b we tried to retrieve the scattering lobe beamwidth (in degree) in function of frequency for both smooth and rough slabs. The purpose of this analysis is to see the different behaviour of the two samples over a wide frequency range and report aspects that usually are not taken into account.

The first step has been to find out the *half power beamwidth* (HPBW) for the various frequencies for both samples (figg. 5.18a–5.18b) and different incidence angles. Note that the HPBW has been calculated with reference to the value in the specular direction of reflection for each frequency, *i.e.*, the measured value of (5.9) in the reflection direction has been evaluated and, with reference to that, the nearest values attenuated of 3 [dB] have been searched, determining the HPBW. Actually the implemented algorithm for the beamwidth calculation is more complicated, because it permits to set an angular step of underthreshold samples to wait before setting beamwidth borders, this in order to neglet local underthreshold peaks that may be present.

As one can see for the smooth sample, we have that for certain frequencies (*e.g.* 2.6 [GHz], 5.4 [GHz] and 8.1 [GHz]) there isn't any reflection lobe, in fact at these frequencies its width ranges from 80° to 160°, while for the rough sandstone slab it doesn't happen.

To explain this phenomenon we have to remember that in the smooth case the slab can be modeled as a constant-thickness wall, so the ideal *Fabry-Pérot model* (see 3.1) holds and the structure has several frequencies of resonance, where the incident field is almost totally transmitted (neglecting losses). The red dotted line in figure 5.17a represents in fact the *power reflection coefficient* obtained from (3.2) and it is easy to see that we don't have the reflection lobe at resonance frequencies (minima of power reflection).

Vice-versa, looking at figure 5.17b, when the rough sample is considered the reflection lobe is always present. This fact could be explained because now the slab has locally always a different thickness, and then the Fabry-Pérot model, which power reflection coefficient in represented in red, doesn't hold anymore, because it assumes an infinite constant-thickness

(a) Smooth sample   (b) Rough sample
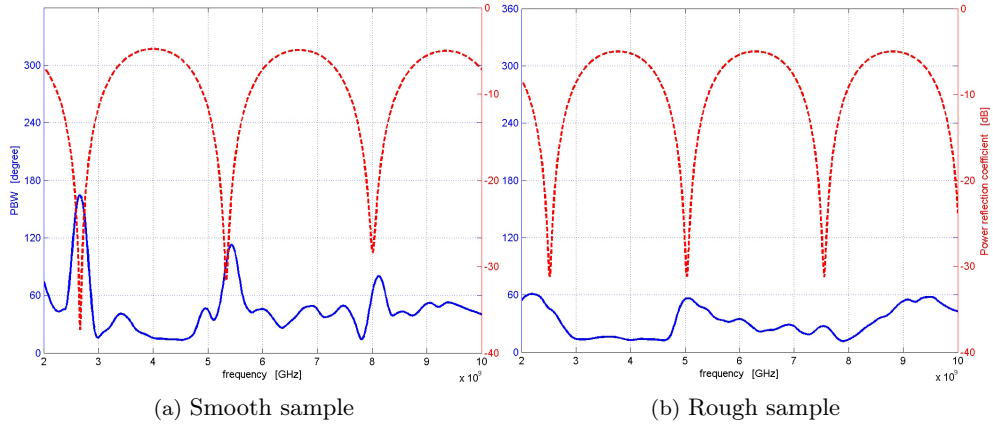
Figure 5.18: HPBW (blue) versus power reflection coefficient (red) in function of frequency for $\varphi_i = 30°$.

wall (fig. 3.1). In the rough case thus the constructive in-phase sum of the field is destroyed and reflection always happens.

Another interesting aspect is that the effect of scattering introduced by the rough surface cannot be seen very well when considering the $-3\,[\mathrm{dB}]$ lobe, because in our case it has a small contribution if compared to the coherent component, then could be better to analyze the $-10\,[\mathrm{dB}]$ lobe (see below).

For example in the following (figg. 5.19a–5.19b) is reported (5.9) at the resonance frequency $f = 5,43\,[\mathrm{GHz}]$ for the smooth sample and $f = 5.03\,[\mathrm{GHz}]$ for the rough (due to a slightly different thickness between the two).

(a) Smooth sample $f = 5,43\,[\mathrm{GHz}]$ (b) Rough sample $f = 5,03\,[\mathrm{GHz}]$
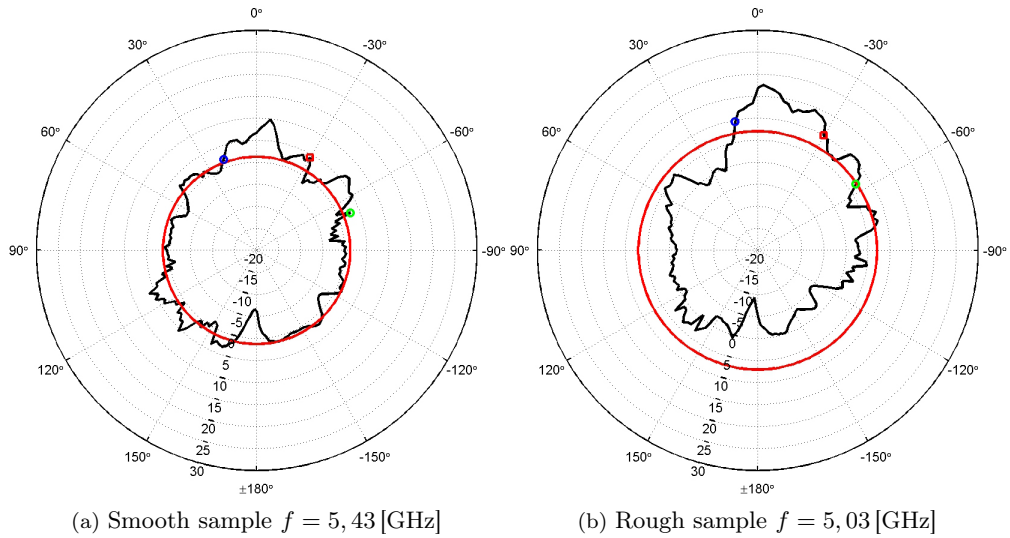
Figure 5.19: HPBW estimation in case of smooth and rough surface at their respective resonance frequencies for $\varphi_i = 30°$. The red straight line shows the $-3\,[\mathrm{dB}]$ threshold level, with respect to the value in reflection, for beam width calculation, while the blue and green dots delimitate the HPBW.

These previous polar plots highlight the fact that in case of roughness the reflection lobe at a resonance frequency is more evident with respect to the smooth slab and in addition the specular reflected power is higher thanks to the fact that the resonance doesn't happen anymore.

As previously said we also investigated the $-10\,[\mathrm{dB}]$ beamwidth of (5.9) for the to samples, in order to better evaluate scattering contribution (figg. 5.20a–5.20b). As before it is clear that at resonance frequencies the smooth slab hasn't any reflection lobe at $-10\,[\mathrm{dB}]$, while the rough sandstone wall continues to be more independent and the beamwidth

(a) Smooth sample

(b) Rough sample
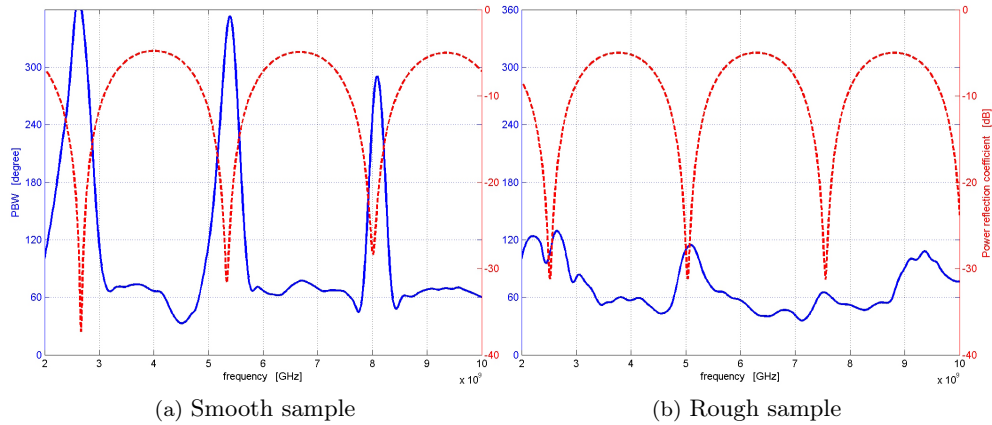
Figure 5.20: -10 [dB] PBW (blue) versus power reflection coefficient (red) in function of frequency for $\varphi_i = 30°$.

is only sligthly accentuated at these frequencies. Moreover for higher frequencies ($f > 8.8$ [GHz]) scattering begins to come out evidently, as the lobe is wider if compared to the smooth case (see for example figg. 5.17a–5.17b).

To conclude it is important to say that these wideband characterizations may have a strong relevance in scattering study, in fact these frequency-dependant aspects are not always taken into account, as the hypotesis of infinite thickness wall is usually done (then no resonance is present). As we seen before, surface roughness introduces a strong variation from what expected in ideal models and from what is measured for a smooth surface, then applications designed without considering these aspects may not work properly and, on the other hand, taking into account these phenomena could lead to a better use of the channel and improve the overall system performance.

6
Conclusion

A complete analysis of diffuse scattering from building structures has been conducted, first its behavior and its relevance in a real propagation scenario are explained and discussed, subsequently some models are reported in a state-of-the-art including articles and studies already present in literature. Starting from this knowledge, this work focus its attention on answering to questions not completely answered yet, in particular we tried to verify that the scattering phenomenon influences more the field in the backward half-space, furthermore we wanted to find out if surface roughness influences the overall power balance with respect to a smooth wall.

Then a new simulation setup based on an electromagnetic *finite integration technique* (FIT) simulator has been *ad-hoc* developed to analyze three-dimensional scattering distribution and allowing to do accurate electromagnetic simulations of real handmade structures, including rough surfaces and different kinds of building blocks reported in 4.2. Its realization required to focus on different topics, first of all how to realize *random rough surfaces* (RRS) in this simulation environment but also how to use them in order to get significant results. In addition the implementation of different kinds of real walls required a good knowledge of *CST Microwave Studio^{TM}* (CST MWS) macro ambient based on a limited set of *Visual Basic* (VBA) instructions.

Simulation results showed that in case of RRS the scattering is more influent in the backward half-space rather than in the forward half-space, its dependence on the surface statistical parameter (standard deviation of height and correlation length) has also been observed in function of frequency showing a good agreement from what expected. Another interesting thing related to this topic is that even when the *Rayleigh criterion* (1.13) considers the surface as smooth the scattered field isn't negligible, thus the *Fraunhofer criterion* (1.14) could be a better condition for discriminating rough and smooth surfaces. In case of volume inhomogeneities no hypothesis about diffuse scattering can be *a priori* done, in fact frequency dependence is strictly related to the sample internal geometry.

On the other hand the study of the system power balance led to the conclusion that surface roughness affects the power loss into media and transferred to other polarizations proportionally to the degree of roughness, while in the state of the art this aspect isn't usually taken into account.

In parallel the design and realization of a measurement setup for scattering characterization has been carried out (see 5) and a wideband characterization of scattering has been done. Results have shown how roughness affects the diffuse field and its different behavior in function of frequency, pointing out an intrinsic transfer function of building materials. In order to have a complete comprehension of scattering in propagation environments all these topics will require deeper investigations, and then our results will permit to better focus the efforts for future works. In particular three-dimensional scattering spatial distribution and the behavior of scattering in case of volume inhomogeneities need to be modeled; moreover further studies are needed to formalize the characterization of the overall power balance and the depolarization of the impinging wave due to surface roughness (and maybe even due to volume irregularities). Finally our measurements can be used to calibrate already existing scattering models (*e.g.* ray-tracing tools) and eventually even

other kinds of samples can be analyzed thanks to the realized experimental setup.

List of Tables

List of Figures

Bibliography

[1] V. Degli Esposti, H. L. Bertoni, "Evaluation of the role of diffuse scattering in urban microcellular propagation", *Vehicular Technology Conference, 1999. VTC 1999 - Fall. IEEE VTS* 50th.

[2] E. M. Vitucci, F. Mani, V. Degli Esposti, C. Oestges, "Polarimetric Properties of Diffuse Scattering From Building Walls: Experimental Parameterization of a Ray-Tracing Model", *IEEE TRANSACTIONS ON ANTENNAS AND PROPAGATION, VOL. 60, NO. 6, JUNE 2012.*

[3] P. Beckmann, A. Spizzichino, "The scattering of electromagnetic waves from rough surfaces", *Pergamon Press, 1963.*

[4] L. Tsang, J. Kong, Kung-Hau Ding, "Scattering of electromagnetic waves: Theories and Applications", *John Wiley & Sons, Inc. 2000.*

[5] L. Tsang, Kung-Hau Ding, S. Huang, X. Xu, "Electromagnetic Computation in Scattering of Electromagnetic Waves by Random Rough Surface and Dense Media in Microwave Remote Sensing of Land Surfaces", *Proceedings of the IEEE, Vol. 101, No. 2, February 2013.*

[6] Ulaby F. T., Moore R. K., Fung A. K., "Microwave remote sensing: active and passive", *Addison-Wesley Publishing Company, London, 1982.*

[7] D. Didascalou et al., "An Approach to Include Stochastic Rough Surface Scattering Into Deterministic Ray-Optical Wave Propagation Modeling", *IEEE TRANSACTIONS ON ATENNAS AND PROPAGATION, VOL. 51, NO. 7, JULY 2003.*

[8] Y. Cocheril, R. Vauzelle, "A new ray-tracing based wave propagation model including rough surfaces scattering", *Progress In Electromagnetics Research, 2007.*

[9] P. Pongsilamanee, H. L. Bertoni, "Specular and Nonspecular Scattering From Building Facades", *IEEE TRANSACTIONS ON ANTENNAS AND PROPAGATION, VOL. 52, NO. 7, JULY 2004.*

[10] V. Degli Esposti, F. Fuschini, E. M. Vitucci, G. Falciasecca, "Measurement and Modelling of Scattering From Buildings", *IEEE Transactions on Antennas and Propagation, Vol. 55 No 1, pp. 143-153, January 2007.*

[11] F. Fuschini, V. Degli Esposti, E. M. Vitucci, "A model for forward-diffuse scattering through a wall", *European Conference on Antennas and Propagation (EuCAP), 2010.*

[12] F. Sagnard, F. Bentabet, C. Vignat, "In Situ Measurements of the Complex Permittivity of Materials Using Reflection Ellipsometry in the Microwave Band: Theory (Part I)", *IEEE TRANSACTIONS ON INSTRUMENTATION AND MEASUREMENT, VOL. 54, NO. 3, JUNE 2005.*

[13] T. Weiland, "A discretization method for the solution of Maxwell's equations for six-component fields", *Electronics and Communication, (AEÜ), Vol. 31, pp. 116-120, 1977.*

[14] K. Uchida, J. Honda, K.Y. Yoon, "An Algorithm for Rough Surface Generation with Inhomogeneous Parameters", *International Conference on Parallel Processing Workshops, 2009.*

[15] J.J. Wu, "Simulation of rough surfaces with FFT", *Tribology International vol. 33, Elsevier, 2000.*

[16] T. K. Chan, Y. Kuga, A. Ishimaru, C. T. C. Le, "Experimental studies of bistatic scattering from two-dimensional conducting random rough surfaces", *IEEE Transactions on geoscience and remote sensing, vol. 34, No. 3, May 1996.*

[17] R. Vaughan, J. Bach, "Channels, propagation and antennas for mobile communications", *IET Electromagnetic Waves Ser. 50. U.K.: IEE, 2003.*

[18] Newport RV series rotation stages user's manual - Newport Corporation